FILIFORM-LIKE CORROSION ON MG-AL AND MG-AL-ZN ALLOYS

FILIFORM-LIKE CORROSION MECHANISM ON MAGNESIUM-ALUMINUM AND MAGNESIUM-ALUMINUM-ZINC ALLOYS

BY ZACHARY P. CANO, B.ENG.

A Thesis

Submitted to the Department of Materials Science & Engineering

and the School of Graduate Studies

in Partial Fulfilment of the Requirements

for the Degree

Master of Applied Science

McMaster University

Master of Applied Science (2015) McMaster University

(Materials Science & Engineering) Hamilton, Ontario, Canada

TITLE:	Filiform-Like Corrosion Mechanism on Magnesium-Aluminum and Magnesium-Aluminum-Zinc Alloys
AUTHOR:	Zachary P. Cano, B. Eng. (McMaster University)
SUPERVISORS:	Dr. Joseph R. Kish, Dr. Joseph R. McDermid
NUMBER OF PAGES:	xix, 135

Abstract

The filiform-like corrosion of Magnesium (Mg) alloys AZ31B and AM30 was investigated with electrochemical and microanalytical techniques. Potentiodynamic polarization testing and scanning vibrating electrode technique (SVET) measurements confirmed the "differential electrocatalytic" mechanism previously reported for filiform and filiform-like corrosion on pure Mg and AZ31B. Transmission electron microscopy (TEM) and Auger electron spectroscopy (AES) revealed that the MgO corrosion filaments on both alloys were likely a product of the direct reaction of Mg and water (H_2O), responsible for the rapid hydrogen (H_2) evolution observed at the propagating corrosion fronts. TEM analysis also revealed through-thickness cracks and noble intermetallic particles within the corrosion filaments and noble metal enrichment at the corrosion filament/metal interfaces, which were proposed to play significant roles in the cathodic activation of the corrosion filaments. The higher susceptibility of the AZ31B alloy to cathodic activation versus AM30 suggested that Zinc (Zn) has a detrimental effect on the resistance of Magnesium-Aluminum-Zinc (Mg-Al-Zn) alloys to filiform and filiform-like corrosion.

Acknowledgments

I would first like to thank my supervisors, Dr. Joseph (Joey) Kish and Dr. Joseph (Joe) McDermid for their expert guidance and support during my Master's degree. I feel very fortunate that they gave me the freedom and flexibility to pursue my academic goals as well as extracurricular activities, in addition to the opportunity to attend numerous conferences and connect with researchers studying corrosion all around the world. It was an absolute pleasure to work with them, and I would like to think I matured a great deal as a result. I would also like to thank my friends and colleagues in the Centre for Automotive Materials and Corrosion and the Department of Materials Science and Engineering, who experienced with me the joys and labours of working in the lab, provided helpful suggestions, and helped me periodically put work aside in favour of other interesting phenomena such as road hockey, softball, bowling, rollercoasters and of course, plenty of food and drinks. I would also like to acknowledge the Natural Science and Engineering Research Council of Canada (NSERC) and Automotive Partnership Canada (APC) for providing funding for this work.

I also owe plenty of thanks to several past and present members of the McMaster community for both technical and intellectual assistance. Mohsen Danaie helped me immensely with microscopy operation and analysis, and I appreciate his patience in answering my repeated questions. Carmen Andrei, Travis Casagrande, Julia Huang, and Shooka Mahboubi also helped with sample preparation and microscopy operation. Mehdi Taheri

introduced me to several pieces of electrochemical testing equipment that I used in this work. Xiangrong (Sarah) Zhang performed chemical analysis and Connie Barry and Doug Culley helped me with sample preparation and apparatus setup. In addition, I must also thank the countless strangers who give hundreds of hours of their free time providing open-source software, Excel macros and scientific knowledge to other strangers like myself over the Internet.

Finally, I would like to thank three people for their support prior to and throughout my Master's degree, and to whom I would like to dedicate this thesis. The first two are my parents, who have shaped who I am today and who have always encouraged me to pursue what I want to pursue (and also for allowing me to move back home while deciding what to pursue next). The third person is my girlfriend and best friend, Catherine, for always making my life exciting and for helping me to not take things too seriously. I genuinely appreciate that she not only supported my work, but also understood it, to the degree that she encouraged me more than anyone else to finally get it all onto paper.

Abbreviations and Symbols

List of Abbreviations

AES	**A**uger **E**lectron **S**pectroscopy
BF	**B**right **F**ield
DF	**D**ark **F**ield
EDS	**E**nergy **D**ispersive X-ray **S**pectrometer/**S**pectroscopy
EELS	**E**lectron **E**nergy-**L**oss **S**pectrometer/**S**pectroscopy
FIB	**F**ocused **I**on **B**eam
GHG	**G**reen**h**ouse **G**as
HAADF	**H**igh-**A**ngle **A**nnular **D**ark **F**ield
HCP	**H**exagonal **C**lose **P**acked
HE	**H**ydrogen **E**volution
NDE	**N**egative **D**ifference **E**ffect
ICP-OES	**I**nductively **C**oupled **P**lasma **O**ptical **E**mission **S**pectroscopy
LOM	**L**ight **O**ptical **M**icroscope/**M**icroscopy
OCC	**O**pen **C**ircuit **C**ondition
OCP	**O**pen **C**ircuit **P**otential
MFERD	**M**agnesium **F**ront **E**nd **R**esearch and **D**evelopment
SAD	**S**elected **A**rea **D**iffraction
SEM	**S**canning **E**lectron **M**icroscope/**M**icroscopy
SVET	**S**canning **V**ibrating **E**lectrode **T**echnique
TEM	**T**ransmission **E**lectron **M**icroscope/**M**icroscopy
XPS	**X**-ray **P**hotoelectron **S**pectroscopy

List of Symbols

A	Ampere
at. %	Atomic percent
cm	Centimetre
E_b	Breakdown potential
E_{corr}	Corrosion potential
eV	Electron volt
g	Gram
h	Hour
Hz	Hertz
I	Current
i	Current density
i_{corr}	Corrosion current density
K	Kelvin
keV	Kiloelectron volt
kJ	Kilojoule
M	Mole per litre
m	Metre
min	Minute
mL	Millilitre
mm	Millimetre
mV	Millivolt
nA	Nanoampere
nm	Nanometre
R^2	Coefficient of determination
s	Second
V	Volt
V_{SCE}	Volt versus a saturated calomel electrode

wt. %	Weight percentage
µm	Micrometre

Table of Contents

List of Tables

List of Figures

Chapter 1: Introduction

Concerns about rising energy demand and subsequent climate change due to greenhouse gas (GHG) emissions have led policymakers around the world to establish various GHG emission reduction targets [1]. In Canada, the transportation sector accounts for approximately 21% of the country's total energy usage and 24% of total GHG emissions [2]. The transportation sector accounts for 28% of total energy usage in the United States, with 59% of total transportation energy use attributed to cars and light trucks [3]. As such, the transportation industry (particularly passenger vehicles) is a major target of efforts to reduce GHG emissions, which highlights the need for "at-the-source" emission-reduction strategies such as high-density urban planning, public transit and car-sharing incentives [4,5]. However, another strategy being undertaken is to improve the energy efficiency of automobiles through technological means. The implementation of sustainable lightweight automotive materials is identified as a key strategy in this regard by the United States-Canada Clean Energy Dialogue [6,7].

The low density of magnesium (Mg) alloys (two-thirds that of aluminum [Al] and one-quarter that of iron [Fe]) makes them promising candidates for light-weight automotive applications. Recognizing this, the Magnesium Front End Research and Development (MFERD) Project was established between Canada, the United States and China in 2007 to investigate and develop technologies enabling the implementation of a magnesium-intensive automotive front end body structure in consumer automobiles [7,8]. A "cradle-

to-grave" lifecycle analysis undertaken as part of this initiative demonstrated that the fuel savings accrued by a 2007 GM-Cadillac CTS with a magnesium-based front end assembly would lead to an overall decrease in energy usage and GHG emissions compared to the standard carbon steel-based front end assembly (Figure 1.1) [9]. Although the vehicle with the Al-based front end assembly had the lowest amount of required energy and emissions expected throughout its lifetime, the authors of the study noted that the most substantial improvements in primary production and recycling efficiency could be expected for Mg in the future due to the relatively low maturity of Mg technology [9].

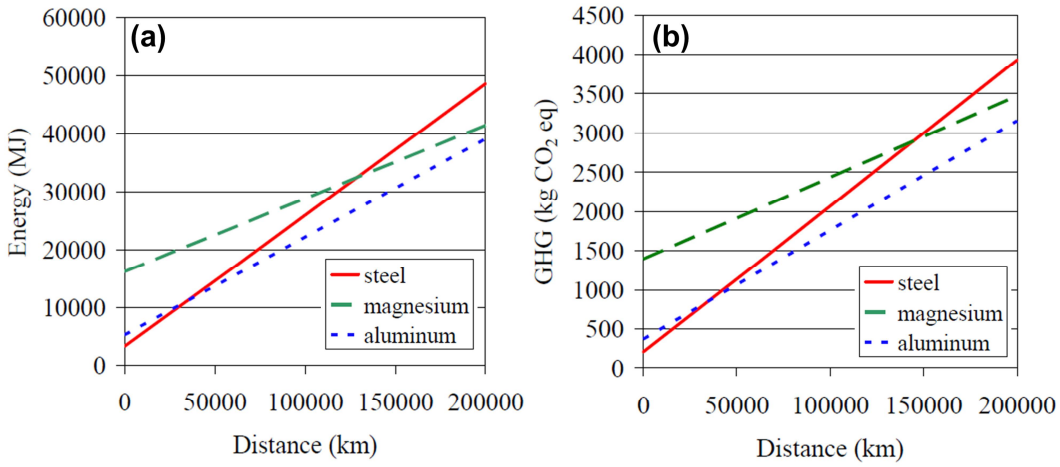

Figure 1.1: "Cradle-to-grave" life cycle analysis of a North America-built 2007 GM-Cadillac CTS with an Al, Mg and carbon steel-based front end assembly [9]. The (a) required energy and (b) GHG emissions expected from each assembly is shown as a function of vehicular distance travelled.

Although the use of Mg alloys has seen significant growth in the automotive industry, the generally poor corrosion resistance in aqueous and chloride (Cl)-containing environments has been a major factor in preventing their widespread adoption [10,11]. Efforts to improve the corrosion resistance of Mg alloys have been complicated by the fact that Mg corrosion is less understood and quite unique versus that of Fe and Al-based alloys [12,13]. One of the MFERD project tasks is thus focussed on better understanding of corrosion processes and protection technologies, including applied coatings schemes [8,14]. Coated Mg and Mg alloys are susceptible to a localized corrosion phenomenon referred to as filiform corrosion [14,15], an example of which is shown in Figure 1.2. Filiform corrosion initiates at a local coating defect and then propagates laterally, undermining the originally intact coating in the process [15]. The specific mechanisms associated with filiform corrosion (which also appears to occur on uncoated Mg and Mg alloys [15,16]) need to better understood in order to aid the development of effective and robust coating schemes. Therefore, this thesis is focused on gaining a better understanding of filiform corrosion of industrially-relevant Mg alloys, namely AZ31B and AM30, which have been considered for implementation in the MFERD front end demonstration structures [8,9].

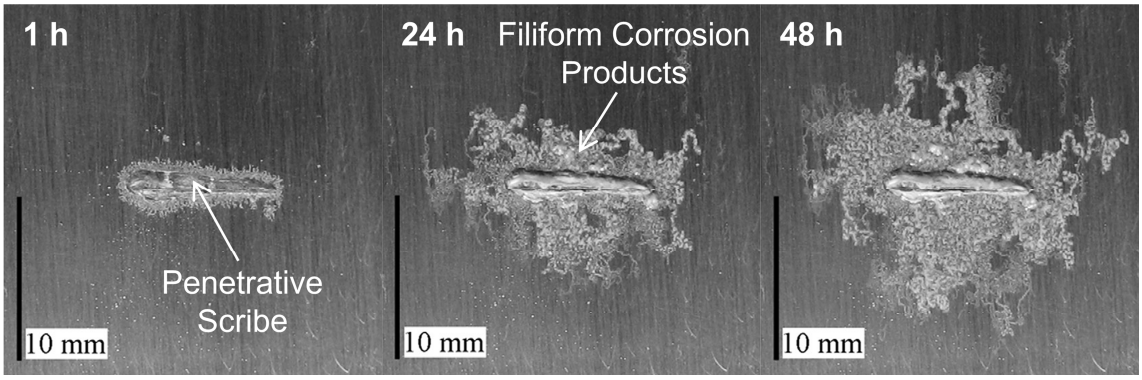

Figure 1.2: Surface images of a polyvinyl butyral-coated pure Mg sample undergoing filiform corrosion [15]. Images were taken at various times after applying a droplet of 1 mole per litre (M) aqueous HCl to a penetrative scribe in the coating.

Chapter 2: Literature Review

2.1. Fundamental Corrosion Mechanism for Mg

Mg is well known as one of the most reactive metals with a standard electrode potential of -2.4 V versus a standard hydrogen (H_2) electrode or -2.6 V versus a saturated calomel electrode (V_{SCE}). When immersed in an aqueous Cl solution, the corrosion potential (E_{corr}) of Mg and its alloys typically falls between -1.4 to -1.8 V_{SCE} [17], which is the lowest of all engineering alloys. This low E_{corr} leads to some important corrosion characteristics unique to Mg. Firstly, within the range of -1.4 to -1.8 V_{SCE} the H_2 evolution (HE) reaction, rather than oxygen (O_2) reduction, is the dominant cathodic reaction regardless of aeration conditions [13]. The low corrosion potential is also a significant concern for Mg alloys which possess heterogeneous microstructures, since the secondary phases are most often cathodic with respect to the Mg matrix phase. This leads to micro-galvanic coupling, causing the Mg matrix phase to be selectively attacked in regions adjacent to the secondary phases [18–21].

The reactions governing aqueous Mg corrosion are most commonly written as shown in Equations (2.1)-(2.4) [18,21]. The anodic Mg dissolution reaction (2.1) and cathodic HE reaction (2.2) cause the production of Mg^{2+} and OH^- ions, respectively, as well as the evolution of H_2 bubbles. The Mg^{2+} and OH^- ions can then undergo a chemical reac-

tion (2.3) to produce Mg hydroxide ($Mg[OH]_2$), resulting in the overall corrosion reaction (2.4) of Mg and H_2O reacting to produce $Mg(OH)_2$ and H_2 gas.

$$Mg \rightarrow Mg^{2+} + 2e^- \tag{2.1}$$

$$2H^+ + 2e^- \rightarrow H_2 \ \underline{or}\ 2H_2O + 2e^- \rightarrow H_2 + 2OH^- \tag{2.2}$$

$$Mg^{2+} + 2OH^- \rightarrow Mg(OH)_2 \tag{2.3}$$

$$Mg + 2H_2O \rightarrow Mg(OH)_2 + H_2 \tag{2.4}$$

The negative difference effect (NDE) is an often-reported phenomenon of aqueous Mg corrosion in which an increased magnitude of anodic polarization (i.e. removal of electrons) is accompanied by increased HE, apparently contradicting Equation (2.2) [13,22,23]. Although a variety of mechanisms [22,24] have been explored to account for this behaviour, a number of recent investigations [13,23,25,26] have pointed to an increased catalytic tendency for HE on increasingly corroded Mg surfaces as the cause of the NDE. Further details of this concept will be discussed in later sections of this chapter and Chapter 6.

2.2. Film Formation and Growth on Mg in Aqueous Media

Aqueous-formed surface films on Mg are typically reported to be composed of a mixture of magnesium oxide (MgO) and $Mg(OH)_2$ with overall film thicknesses ranging from approximately 10 nm to a few μm, depending on the immersion time [27–31]. Investiga-

tions employing X-ray photoelectron spectroscopy (XPS) have demonstrated that the Mg(OH)2-rich outer layer of the surface film thickens as a function of immersion time, whereas the MgO-rich inner layer thickness remains relatively constant [29,30].

The surface film formed on Mg after immersion in a bulk volume of pure water (H2O) for 48 h has been investigated by Nordlien et al. [27] and Taheri et al. [31] using cross-sectional transmission electron microscopy (TEM). Nordlien et al. observed a three-layer structure comprised of a cellular $Mg(OH)_2$ inner layer, dense MgO intermediate layer and platelet-like $Mg(OH)_2$ outer layer, shown schematically in Figure 2.1. The MgO intermediate layer was assumed to have formed as a result of ambient atmosphere exposure prior to immersion, whereas the outer and inner $Mg(OH)_2$ layers were assumed to have formed as a result of egress of Mg^{2+} and ingress of H_2O, respectively, through the intermediate layer [27]. Taheri et al., on the other hand, observed a two-layer structure consisting of a platelet-like $Mg(OH)_2$ outer layer overtop a porous MgO-rich inner layer (Figure 2.2). It was proposed that the thermodynamically-favourable chemical hydration of the initially-present MgO-rich layer led to the observed porosity in the inner layer, presumably because of internal stresses associated with the lattice expansion upon transformation from MgO to $Mg(OH)_2$ [31]. The induced porosity constituted a "breakdown" of this layer allowing for the dissolution-precipitation mechanism responsible for the $Mg(OH)_2$ outer layer formation (Figure 2.3) [31]. Differing preparation techniques used by Nordlien at al. (ultramicrotomy) and Taheri et al. (focused ion beam [FIB] milling) were proposed to have influenced the differing observations between the two studies [31]. Taheri et al. also measured the open circuit potential (OCP) of Mg as a function of im-

mersion time in pure H_2O (Figure 2.4). It was proposed that the initial rise of the OCP within the first 2 h of immersion corresponded to the hydration of the initial MgO layer, and that the plateau corresponded to the formation of the outer $Mg(OH)_2$ layer [31]. Some support for this notion was provided in a cross-sectional TEM investigation of Mg performed by Unocic et al. [32], who observed only a single-layer MgO structure with a thickness of tens of nm following a shorter immersion time of 4 h in pure H_2O. However, it should be noted that Taheri et al. immersed their Mg samples in a 1000 mL volume of H_2O while Unocic et al. only used 5 mL, the latter of which was determined to result in a notably thicker surface film [32].

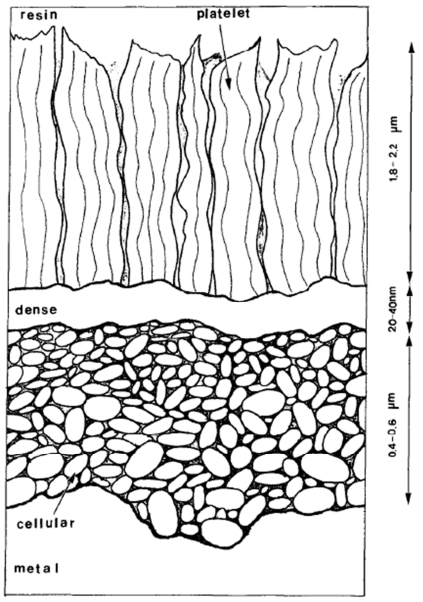

Figure 2.1: Schematic representation of the three-layer surface film on Mg observed by Nordlien et al. after immersion in pure H_2O for 48 h [27].

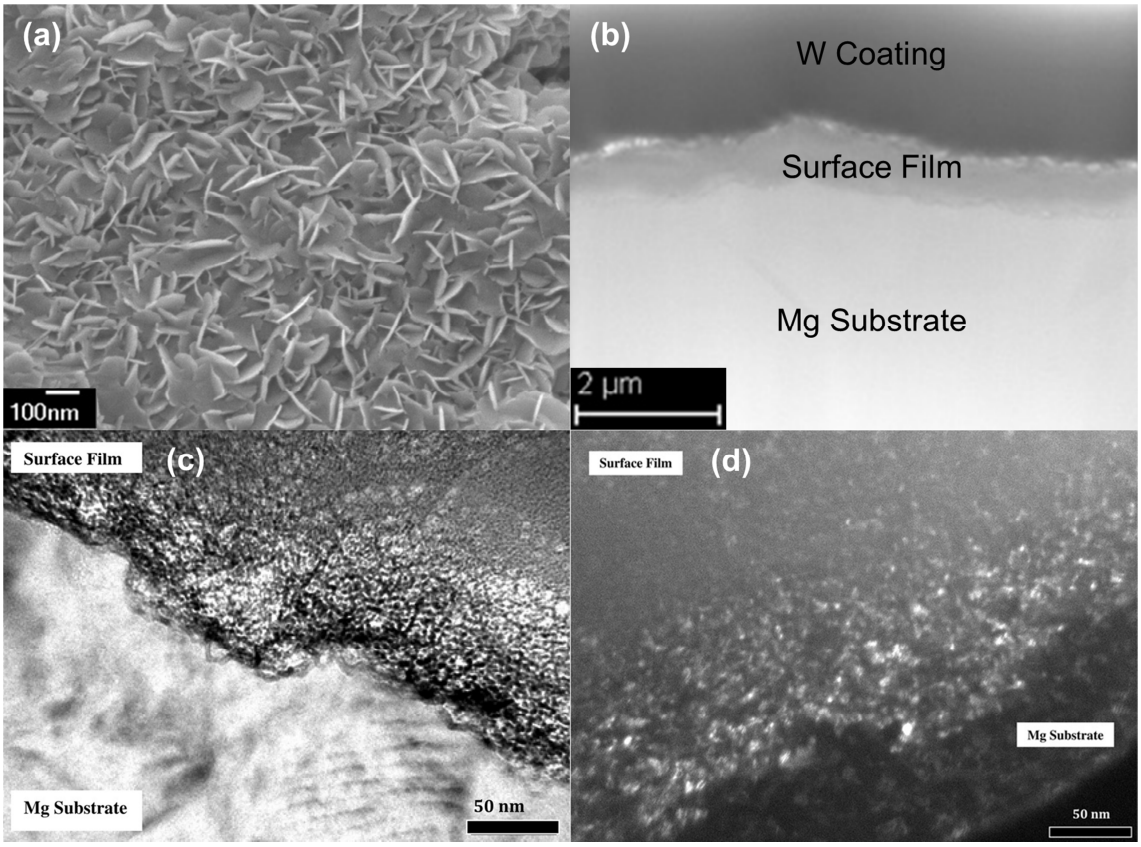

Figure 2.2: (a) SE-SEM image displaying plan view morphology of the surface film formed on Mg after immersion in pure H_2O for 48 h, (b) SE-SEM image displaying FIB-prepared thin foil cross section of the surface film, (c) Bright field (BF)-TEM image of the surface film in cross-section, (d) Dark field (DF)-TEM image of the surface film in cross-section highlighting the (200) MgO plane [31].

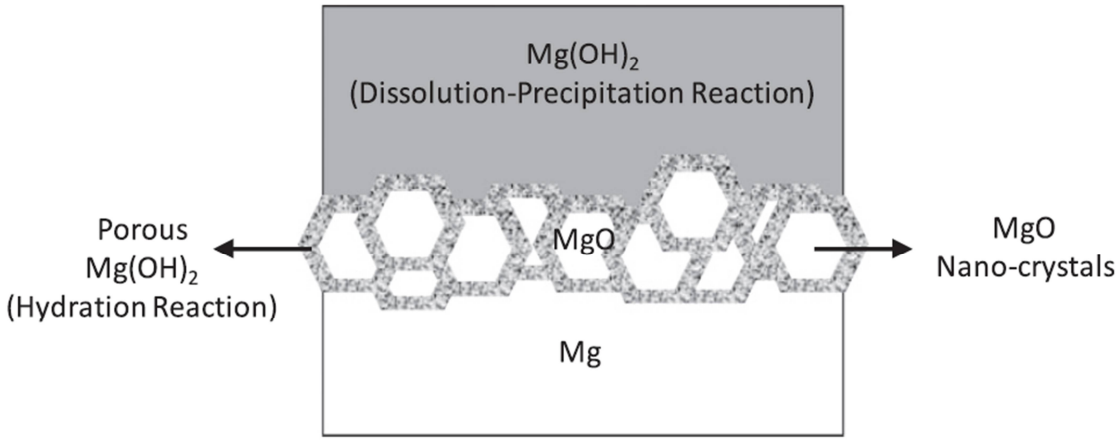

Figure 2.3: Schematic representation of the two-layer surface film on Mg observed by Taheri et al. after immersion in pure H_2O for 48 h [31].

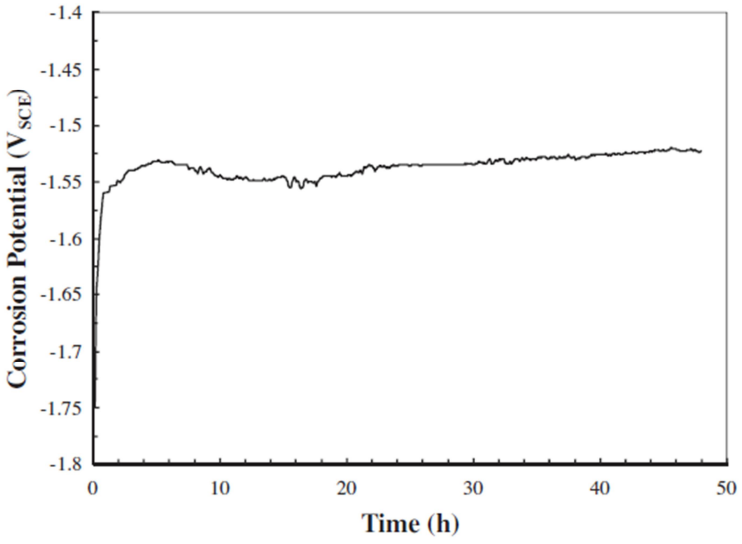

Figure 2.4: Plot of the OCP of Mg as a function of immersion time in pure H_2O [31].

2.3. Effects of Alloying Elements on General Corrosion Behaviour of Mg

The addition of alloying elements to Mg often results in the formation of secondary phases, which as mentioned in Section 2.1 can lead to micro-galvanic interactions and ultimately localized corrosion. However, the AZ31B and AM30 alloys investigated in this thesis possess single-phase microstructures with the exception of aluminum-manganese (Al-Mn) intermetallic particles. Therefore, this section focuses on the effects of solid-solution additions of Al and zinc (Zn) on the corrosion behavior of Mg, while the effects of Mn additions are discussed in the context of Al-Mn particles.

2.3.1. Aluminum

The solid-solution addition of Al has been widely reported to improve the corrosion resistance of Mg via Al-enrichment of the oxide/hydroxide surface film, which strengthens the film and leads to reduced anodic kinetics [33–39]. Following aqueous immersion of solid-solution Mg-Al binary alloys containing 3-16 wt.% Al, Baliga and Tsakiropoulos [35] and Mathieu et al. [38] reported the formation of a hydrotalcite-type film consisting of $Mg(OH)_2$ structures with Al^{3+} ions substituting for a portion of the Mg^{2+} lattice sites. Nordlien et al. [36,37] carried out cross-sectional TEM examinations of Mg alloys containing 2-3 wt.% Al immersed in pure H_2O for 48 h and reported the same three-layer structure as they observed for pure Mg (Figure 2.1). However, energy dispersive X-ray

spectroscopy (EDS) measurements revealed the surface films to be enriched with up to 35 wt.% Al at certain locations and the outer $Mg(OH)_2$-rich layer decreased in thickness as a function of alloyed Al content [36,37]. Phillips and Kish [40] similarly reported an Al-enriched surface film above the Mg-rich matrix phase of Mg alloy AZ80.

2.3.2. Zinc

Several investigations have studied the corrosion behaviour of binary Mg-Zn alloys, but the formation of secondary phases or inhomogeneities in as-cast microstructures made it difficult to separate micro-galvanic effects from the effects of Zn in solid solution with Mg [41–43]. Xia et al. [44] investigated solutionized binary Mg-Zn alloys containing 0-2 wt.% Zn and found that the anodic kinetics decreased as a function of Zn content while the cathodic kinetics increased, leading to an overall neutral effect on the corrosion current. The anodic and cathodic kinetics were changed by approximately an order of magnitude with the addition of 2 wt.% Zn [44].

Metallic Zn-enriched layers have been observed at the film/metal interface of both air-formed [45] and aqueous-formed [32,40] surface films on Mg alloys containing approximately 0.5-1 wt.% Zn. Unocic et al. [32] suggested the enrichment of Zn at the surface of the metal led to decreased anodic kinetics, which is consistent with the previously discussed findings of Xia et al [44]. Additionally, the fact that cathodic kinetics on Zn are approximately an order of magnitude larger than Mg at the corrosion potential of Mg [46]

would explain the enhanced cathodic kinetics observed when Zn is added in solid solution with Mg [44].

2.3.3. Manganese

Mn has a very low solid solubility in Mg (approximately 0.95 at% at 650°C [47]) and therefore is expected to be virtually absent from the matrix phase of the alloy that it is added to. One of the main purposes of adding Mn to Mg alloys is to scavenge Fe by forming Al-Mn-(Fe) particles, thus eliminating elemental Fe particles from the microstructure which otherwise would cause severe micro-galvanic corrosion [48–50]. The Al-Mn-(Fe) particles are often separated from the alloy during the melting stage prior to casting [49]. Regardless of whether or not this separation occurs, the corrosion resistance of the alloy is improved by the Mn addition because the Al-Mn-(Fe) phase is a less efficient cathode than pure Fe [50].

2.4. Localized Corrosion Phenomena of Pure Mg and Single-Phase Mg Alloys

While localized corrosion on multi-phase Mg alloys can often be explained by micro-galvanic effects, localized corrosion mechanisms on pure Mg and single-phase alloys are not well understood [18–21]. Localized corrosion on these materials is generally charac-

terized by the appearance of dark corrosion products which propagate laterally across the surface of the metal. The corrosion products tend to form as thread-like "filaments" or radially-expanding "discs", the latter of which can be mistaken as traditional pitting at short times after their initiation [12,15,16,26,51–57]. The advancement of localized electrochemical techniques and high-resolution electron imaging has allowed researchers to make significant developments in the understanding of localized corrosion phenomena on pure Mg and single-phase alloys [12,15,16,51,58].

2.4.1. Pure Mg

Several researchers have reported the occurrence of localized corrosion on pure Mg during immersion in aqueous sodium chloride (NaCl) solutions. Disc-like corrosion tends to occur in relatively concentrated (greater than 0.6 M) solutions [12,26] while filiform-like corrosion tends to occur during immersion in relatively dilute (0.1 M or less) solutions [15,52–54].

Williams and co-workers have offered critical insights into the electrochemical mechanism of localized corrosion on pure Mg by employing the scanning vibrating electrode technique (SVET) [12,15,54]. The SVET involves vibrating a platinum (Pt) microelectrode tip close to the sample surface and measuring the voltage difference between the two extremes of the tip's position. Then, knowing the conductivity of the solution and the amplitude of the tip vibration, ionic current density can be calculated in the direction of vibration using a modified form of Ohm's law [59]. Alternatively, a calibration relating

the measured voltage difference and ionic current density for a given solution can be performed by taking vibrating electrode measurements of a series of known applied current densities [12]. A more detailed explanation of the SVET is available elsewhere [59]. The ability to measure spatially-resolved ionic currents makes the SVET an excellent choice to study localized corrosion phenomena on any metal. However, the technique can be particularly advantageous for investigations of the localized corrosion of Mg when compared to scanning electrochemical microscopy techniques which employ microelectrodes to collect evolved Mg^{2+} and H_2. This is because the local detection of HE via H_2 collection cannot be directly correlated to local cathodic currents, since rapid Mg dissolution (i.e. an anodic process) is often accompanied by HE at the same locations on the surface [60]. By contrast, SVET-detected cathodic ionic currents above corroding Mg can only correspond to the cathodic HE reaction [Equation [2.2]).

During the initial immersion of pure Mg in a 5% w/v (0.86 M) NaCl solution, Williams and McMurray [12] noted that the OCP quickly increased (Figure 2.5) as the polished metal surface turned a whiter colour, which indicated the transition from an air-formed surface film into a thicker aqueous-formed surface film. A SVET plot collected during this initial film-forming phase revealed several cathodic "hotspots" (Figure 2.6), which may have indicated the locations of either defects in the surface film or cathodic impurity particles such as elemental Fe. The inflection point of the OCP transient curve shown in Figure 2.5 corresponded with the initiation of a dark corrosion product which subsequently spread across the metal surface in the form of a corrosion disc (Figure 2.7[a]). The SVET plots shown in Figure 2.7(b) revealed net cathodic currents above the

regions consumed by the corrosion disc. Galvanic coupling of this region with the adjacent intact metal surface caused intense anodic currents at the perimeter of the laterally-spreading corrosion discs. This "differential electrocatalytic" mechanism was also shown to drive filiform corrosion on coated pure Mg (Figure 1.2) with scanning Kelvin probe measurements [15].

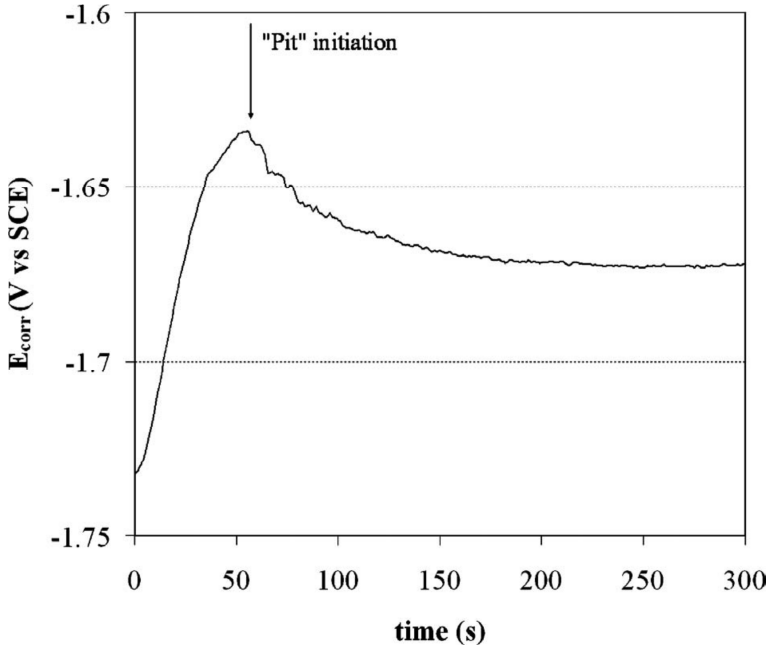

Figure 2.5: Plot of the OCP of Mg as a function of immersion time in a 5% w/v (0.86 M) NaCl solution [12].

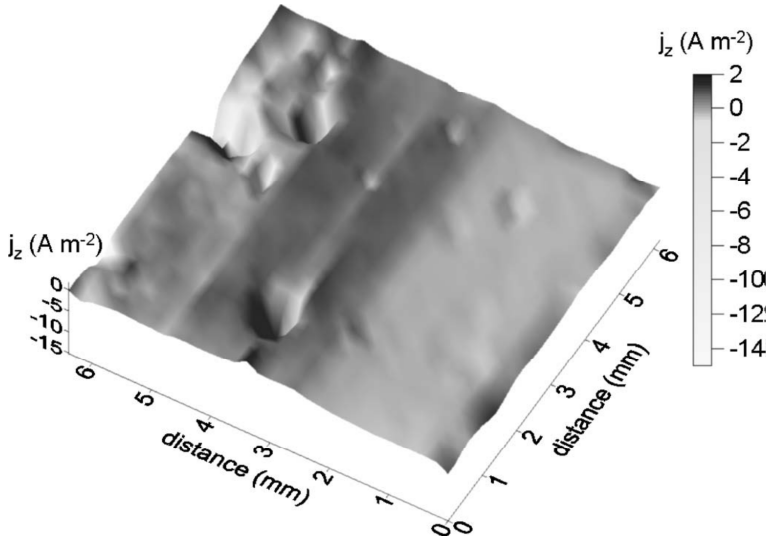

Figure 2.6: SVET plot of pure Mg immediately after immersion in a 5% w/v (0.86 M) NaCl solution (prior to initiation of localized corrosion) [12].

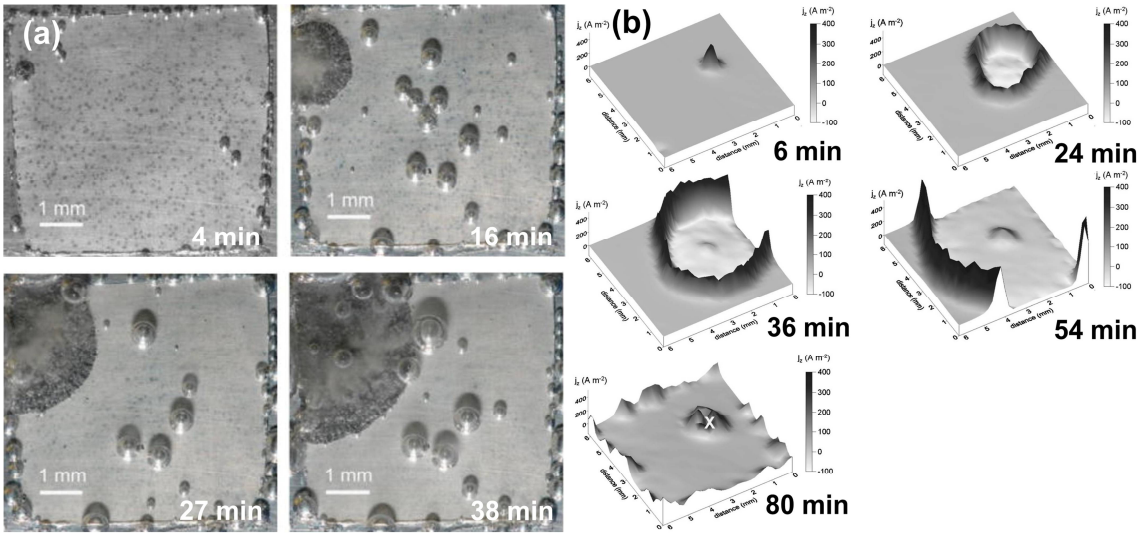

Figure 2.7: (a) Surface images and (b) SVET plots of pure Mg at various times after immersion in a 5% w/v (0.86 M) NaCl solution [12]. Note that (a) and (b) were recorded from different samples, and thus the surfaces images and plots do not directly correspond to one another.

Enhanced catalytic activity for the cathodic reaction on corroded Mg has been independently verified via conventional cathodic polarization experiments on pure Mg surfaces previously subjected to anodic polarization [23,58]. The "cathodic activation" of corroded Mg has thus been suggested as the cause of the NDE, since anodic polarization leads to the rapid formation of localized corrosion products, which would subsequently increase the rate of the HE reaction [13,23]. However, the mechanism by which the HE reaction is enhanced on corroded Mg is still unclear. Cathodic activation of the locally corroded regions of pure Mg has been proposed to result from enrichment of more noble impurity elements such as Fe, which are left behind when Mg is selectively dissolved [12,61]. Physical evidence in support of this mechanism was provided in an investigation by Taheri et al. [58] where Fe particles were resolved with TEM in the corroded regions of anodically polarized pure Mg (Figure 2.8[c,d]). However, Samaniego et al. [62] provided some evidence casting doubt on the above mechanism by showing that Mg alloyed with Ca, which is more electrochemically active than Mg, exhibited a higher HE rate than pure Mg under galvanostatic anodic polarization. Williams and McMurray also suggested the increased surface area evidenced by the roughened appearance of the regions consumed by the corrosion disc could be an additional factor causing enhanced cathodic kinetics on locally corroded Mg [12]. The investigation by Taheri et al. [58] also provided evidence of this claim, as the plan view SEM images of the corrosion disc revealed a rough platelet-like morphology (Figure 2.8[a,b]).

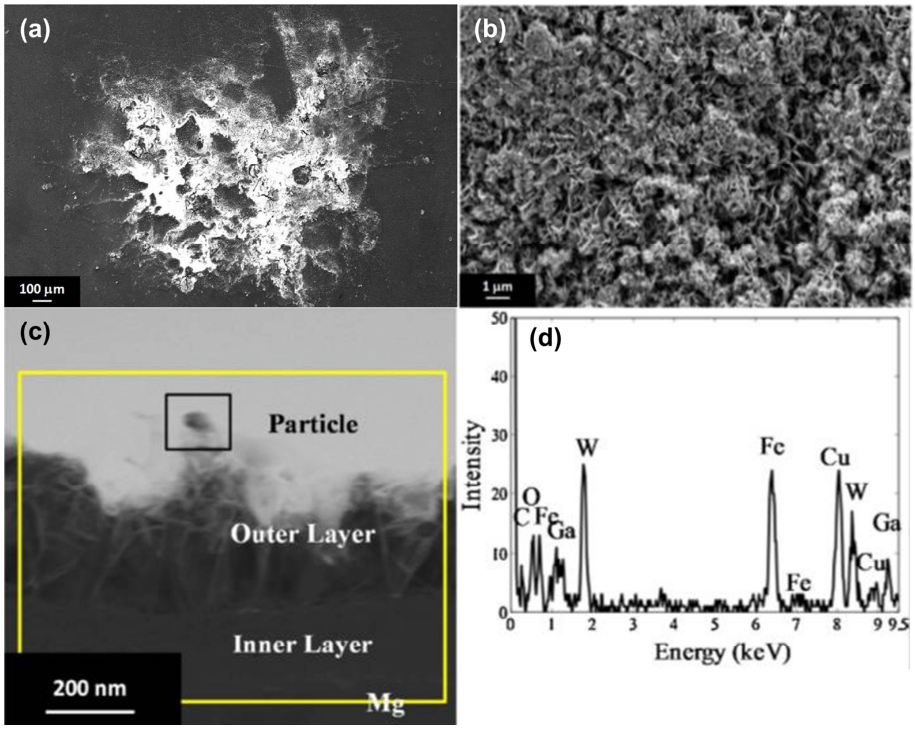

Figure 2.8: (a) SE-SEM image displaying plan view morphology of the corrosion disc formed on Mg after immersion in 0.01 M NaCl for 48 h followed by anodic polarization at -1.0 V_{SCE}, (b) higher magnification plan view SE-SEM image of the corrosion disc, (c) HAADF-STEM image of the corrosion disc in cross-section, (d) EDS point identification spectra from the area marked by the small square in (c) (note that the gallium (Ga), tungsten (W) and copper (Cu) signals were artifacts of the FIB and TEM sample preparation technique [58].

A subsequent investigation by Williams and Grace [15] demonstrated that the immersion of pure Mg in a more dilute solution of 0.01 M NaCl led to filiform-like corrosion rather than disc-like corrosion (Figure 2.9[a]). However, the SVET measurements shown in Figure 2.9(b) revealed that the electrochemical mechanism of filiform-like cor-

rosion was identical to that of disc-like corrosion, since the regions previously consumed by the corrosion filaments displayed enhanced catalytic activity for the cathodic HE reaction. The change from disc-like to filiform-like morphology upon reducing the NaCl concentration has been suggested to be caused by the reduction of the conductivity (i.e. throwing power) of the solution, thereby hindering the ability of the local cathode to galvanically couple with its entire perimeter [54].

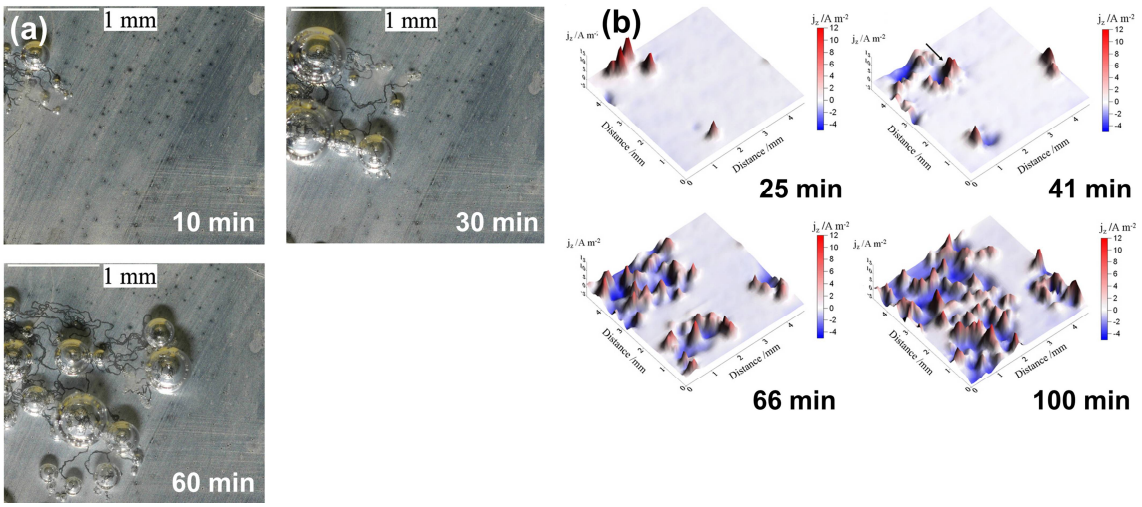

Figure 2.9: (a) Surface images and (b) SVET plots of pure Mg at various times after immersion in a 0.01 M NaCl solution [15]. Note that (a) and (b) were recorded from different samples, and thus the surfaces images and plots do not directly correspond to one another.

Schmutz et al. [51] and McCall et al. [63] have extensively characterized the structural and crystallographic properties of filiform-like corrosion on Mg in an aqueous solution of 0.01 M NaCl with a small addition (10^{-4} M) of sodium dichromate

($Na_2Cr_2O_7$). XPS analysis revealed that Cr was not significantly incorporated into the corrosion filaments [51], indicating that these investigations can be justifiably compared to other investigations which used NaCl solutions containing no $Cr_2O_7^{2-}$ ions. The corrosion filaments propagated laterally in high-surface energy directions such as grain boundaries, twin boundaries and scratch lines [51], and plan view SEM imaging of the corrosion filaments revealed the presence of several cracks within the corrosion products (Figure 2.10[a]). The authors noted that the cracks could be attributed to shrinkage only if the corrosion products were composed of MgO, and not $Mg(OH)_2$, since the former has a smaller lattice parameter than Mg while the latter does not [51]. A higher magnification plan view SEM image of the corrosion filament (Figure 2.10[b]) revealed a roughened surface that appeared similar in morphology to that of the corrosion disc shown previously (Figure 2.8[b]). An SEM image of a FIB-prepared trench through a freshly formed corrosion filament, viewed at a 45º angle, is shown in Figure 2.10[c]. The corrosion filament appeared to have tunnelled underneath the $Mg(OH)_2$-rich surface film previously present on the Mg surface (referred to herein as a pre-existing surface film), which is identical to the process of filiform propagation on an organic-coated metal [15]. The interface between the filament and metal was very rough, perhaps further supporting the notion of an increased surface area of corroded Mg causing a locally enhanced HE rate (albeit at the filament/metal interface in this case rather than the surface of the filament). Considerable electronic contrast was observed within the corrosion filament, with the top-centre portion appearing similar in intensity to the pre-existing $Mg(OH)_2$-rich surface film and the remainder of the filament appearing much brighter. The authors deduced that the lighter

portion was a very hard or electronically-insulating MgO-based corrosion product, since they also noted that argon (Ar) ion-sputtering through this region was significantly slower than sputtering through the porous pre-existing $Mg(OH)_2$-rich surface film.

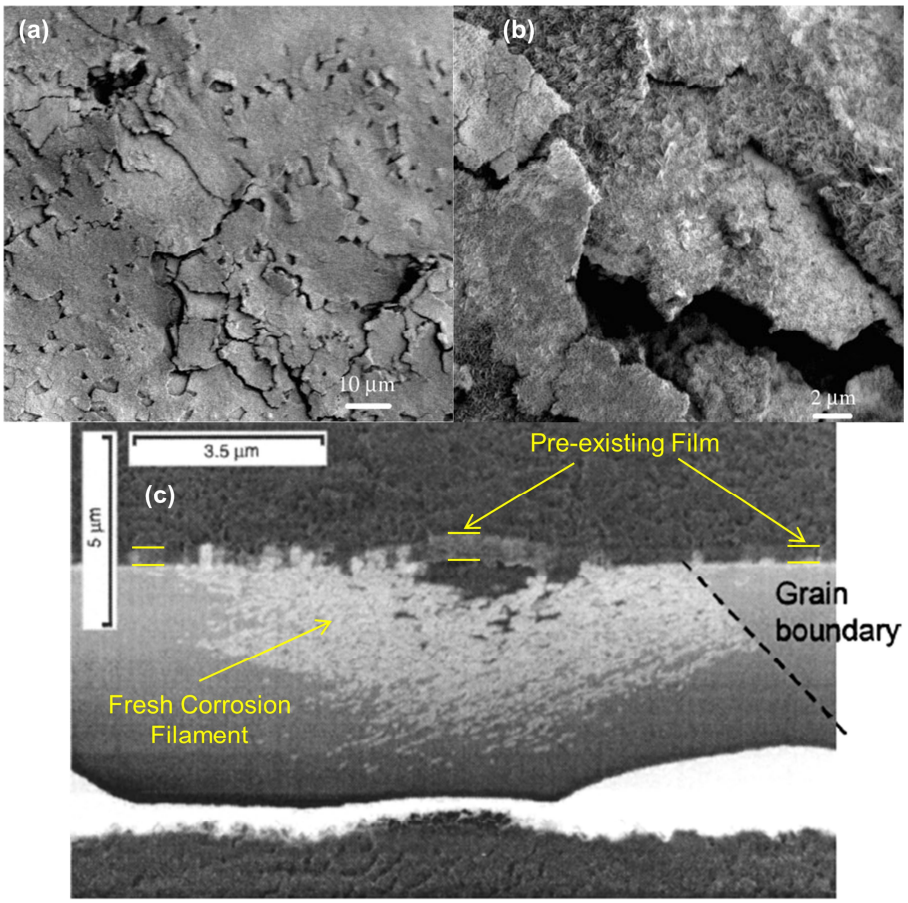

Figure 2.10: (a) SE-SEM image displaying plan view morphology of a corrosion filament on a (0001) Mg surface after immersion in 0.01 M NaCl + 10^{-4} M $Na_2Cr_2O_7$ for 2 h, (b) higher magnification plan view SE-SEM image of the corrosion filament [63], (c) SE-SEM image (utilizing a Ga ion beam) of a FIB-prepared trench through a freshly formed corrosion filament on a Mg surface after immersion in 0.01 M NaCl + 10^{-4} M $Na_2Cr_2O_7$ for 2 h (viewed at a 45° angle) [51].

2.4.2. AZ31B Alloy

Mg alloy AZ31B, nominally containing 3 wt.% Al, 1 wt.% Zn and 0.3 wt.% Mn, is a commonly used wrought Mg alloy because of its relatively good strength, ductility and corrosion resistance [20]. The 'B' designation as outlined in the ASTM standard on the codification of Mg alloys specifies the maximum tolerance limits of various impurity elements, which includes 0.005 wt.% for Fe [64]. AZ31B is a single-phase alloy with the exception of intermetallic Al-Mn particles distributed throughout the matrix [48,65–68]. The beta (β-$Mg_{17}Al_{12}$) phase is not typically observed in AZ31B, and thermodynamic modelling only predicts it to form below 200°C [68]. The Al-Mn particles observed are most commonly reported as Al_8Mn_5 with sizes ranging from 2 to 20 μm [48,65,67,68], although Al-Mn particles with sizes on the order of tens of nanometers have also been resolved with TEM [66,69].

In neutral-pH solutions with Cl concentrations ranging from 0.01 M to 0.86 M, AZ31B tends to undergo filiform-like corrosion [16,55,56]. Williams et al. [16] have shown that the corrosion filaments formed on as-cast AZ31B in a 5% w/v (0.86 M) NaCl solution become cathodically activated in the same manner as the corrosion discs or corrosion filaments on pure Mg, leading to intense local anodes at the heads of the corrosion filaments (Figure 2.11). The observation of filiform-like corrosion on AZ31B rather than the disc-like corrosion observed on pure Mg immersed in the same solution (Figure 2.7) was justified by the order-of-magnitude lower cathodic current densities measured on the regions consumed by the filaments [16]. Therefore, similarly to immersing pure Mg in a

lower-conductivity solution (Figure 2.9), the reduction of the catalytic efficiency of the locally corroded region prevented galvanic coupling with its entire perimeter, leading instead to filiform-like propagation along energetically-favourable pathways. The cathodic activation of the corrosion filaments on AZ31B was proposed to result from a buildup of noble [70] Al-Mn particles which were left behind as the Mg matrix phase dissolved, as shown schematically in Figure 2.12 [16]. The reduction of the catalytic efficiency of the corrosion filaments on AZ31B with respect to the corrosion discs on pure Mg was thus corroborated with the proposal that the cathodic activation of the latter was caused by a buildup of more cathodically-efficient pure Fe particles. This observation provides strong evidence that the susceptibility of Mg and Mg alloys to cathodic activation (and thus, filiform or filiform-like corrosion) is highly dependent on the cathodic efficiency of their microstructural constituents.

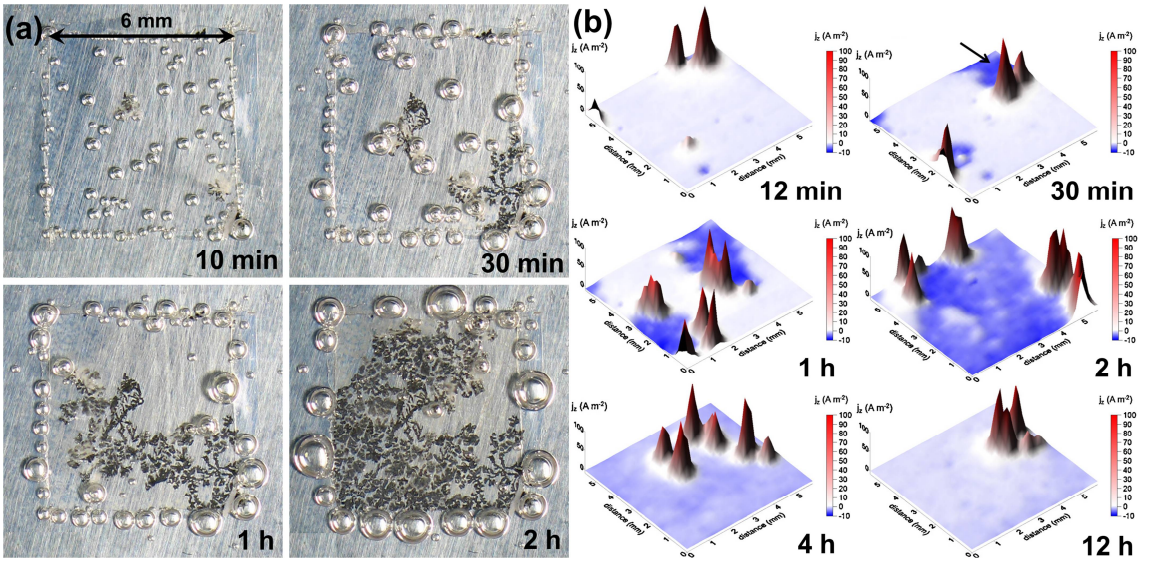

Figure 2.11: (a) Surface images and (b) SVET plots of AZ31B at various times after immersion in a 5% w/v (0.86 M) NaCl solution [16]. Note that (a) and (b) were recorded from different samples, and thus the surfaces images and plots do not directly correspond to one another.

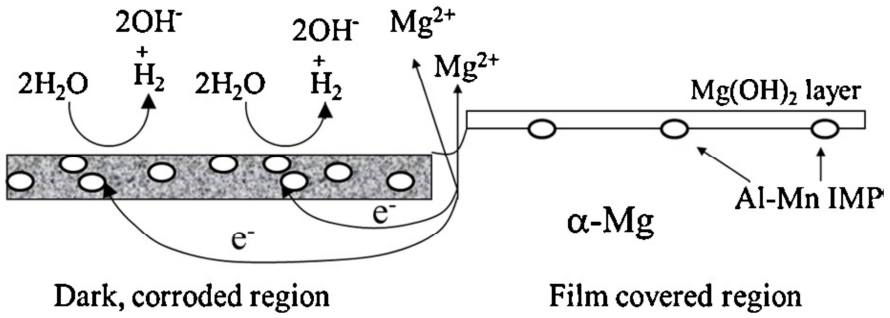

Figure 2.12: Schematic representation of the proposed filiform-like corrosion mechanism on AZ31B [16].

2.4.3. AM30 Alloy

Mg alloy AM30 nominally contains 3 wt.% Al and 0.4 wt.% Mn, with the absence of Zn being the major factor differentiating it from the AZ31B alloy [71]. The alloy was first developed in 2007, where an investigation demonstrated that the absence of Zn allowed for an improvement of the extrudability of the alloy with respect to AZ31B [71]. It should be noted that the AM30 alloy is not listed in the most recent ASTM standard on the codification of Mg alloys and thus does not contain the 'B' designation; however, the nominal maximum tolerance limit of 0.004 wt.% Fe specified for the alloy would pass the 'B' designation requirement for AZ31B [64,71]. As expected, the AM30 alloy is similar to the AZ31B alloy in that it is a single-phase alloy with the exception of intermetallic Al-Mn particles [72,73].

In comparison to AZ31B, relatively few studies have been conducted on the corrosion behaviour of AM30. Hu et al. [74] determined that the polarization kinetics prior to localized corrosion initiation on AM30 were not significantly different than on AZ31B in a GMW14872 test solution (0.9 wt.% [0.16 M] NaCl, 0.1 wt.% [0.009 M] $CaCl_2$ and 0.075 wt.% [0.009 M] $NaHCO_3$) at pH 7.9. However, Zhao et al. [73] determined that the corrosion rate of AM30 was considerably higher than AZ31B in a more aggressive solution (3 wt.% [0.53 M] NaCl) in which localized corrosion was initiated. Song et al. [57] characterized the localized corrosion behaviour of AM30 immersed in 3.5 wt.% (0.62 M) NaCl and determined a polished surface was susceptible to filiform-like corrosion similar to AZ31B.

Chapter 3: Research Objective

Previous studies have shown that filiform or filiform-like corrosion on both uncoated and coated Mg and Mg alloys is driven by a "differential electrocatalytic" process, whereby the corrosion filaments catalyze the cathodic HE reaction and galvanically couple with intense anodic Mg dissolution at the filament heads. However, the precise mechanism by which the corrosion filaments are cathodically activated has not been elucidated in the literature to date. The main objective of the present investigation was thus to link the electrochemical behaviour of filiform-like corrosion on Mg alloys with the physical and chemical structure of the corrosion filaments, such that a stronger understanding of the controlling factors of the filiform-like corrosion process could be established. Since Mg alloys adopted in exterior automotive applications will likely require applied coatings, a better understanding of these factors should prove to be useful in mitigating filiform corrosion from local coating defects.

The filiform-like corrosion tendencies of Mg alloys AZ31B and AM30, which are two of the candidate alloys that have been studied in the MFERD project, were investigated and compared to one another. The electrochemical behaviour was characterized with conventional polarization tests and the SVET, while the corroded structures were characterized with cross-sectional TEM and Auger electron spectroscopy (AES) depth profiling. The intention of the latter exercise was to find evidence of Al-Mn particle buildup in the corrosion filaments and/or any other significant differences between the

corrosion filaments and the adjacent intact surfaces which could explain why and how the corrosion filaments became cathodically activated. Since Al-Mn particles were expected to be present in both alloys, any differences in their observed electrochemical behaviours could presumably be rationalized by different particle properties (i.e. particle size, distribution and/or stoichiometry) or different alloying contents (i.e. alloyed Zn for AZ31B).

Chapter 4: Experimental Methods

4.1. Materials

In this work, the filiform-like corrosion of Mg alloys AZ31B and AM30 taken from an automobile shock tower sub-assembly demo structure was investigated. The automotive demo structure was fabricated under the MFERD project [8,75]. The AZ31B alloy was in the form of a 2.0 mm thick wrought sheet in the H24 temper and the AM30 alloy comprised a 3.0 mm thick extruded part.

The chemical compositions of each alloy as determined by inductively coupled plasma optical emission spectroscopy (ICP-OES) are presented in Table 4.1. The AZ31B alloy had a slightly higher Al composition than the AM30 alloy (3.1 vs. 2.9 wt. %) and a slightly lower Mn composition (0.3 vs. 0.4 wt. %). However, the major compositional difference between the two alloys was the amount of Zn in each alloy; the AZ31B alloy contained 1.2 wt. % Zn whereas the AM30 alloy contained no detectable Zn. The compositions of both alloys were within the ranges outlined by their respective specifications [64,71].

Table 4.1: Chemical composition of alloying elements in the AZ31B and AM30 alloys determined by ICP-OES.

Alloy	Al		Zn		Mn	
	Wt. %	At. %	Wt. %	At. %	Wt. %	At. %
AZ31B	3.08	2.81	1.16	0.44	0.293	0.131
AM30	2.86	2.59	Not Detected		0.409	0.182

Prior to electrochemical testing, a cross-sectional (i.e. transverse) and plan-view (i.e. longitudinal) face of each alloy was cold-mounted in epoxy in order to examine their respective microstructures. The mounted surfaces were polished using standard metallographic techniques and water-free lubricants. The samples were imaged with a Nikon Eclipse LV100 light optical microscope (LOM) and JEOL JSM-7000F scanning electron microscope (SEM), the latter of which was operated at 200 kV. Prior to LOM analysis, the samples were etched in a solution of 25 mL ethanol, 5 mL acetic acid and 2.1 g picric acid for 3 to 5 s in order to reveal their grain structures. After etching the samples were rinsed with ethanol and dried in a warm air stream. Prior to SEM analysis, a carbon (C) film was deposited on the sample surfaces in order to prevent major charging of the samples under the electron beam.

The AZ31B alloy possessed an exterior layer containing relatively coarse grains (Figure 4.1[a]) while the AM30 alloy possessed a dual-layer exterior containing relatively fine grains at the top surface and relatively coarse grains just below the top surface (Figure 4.2[a]). These “skin” layers had a maximum thickness of approximately 500 μm for both alloys. Figure 4.1(b,c) and Figure 4.2(b,c) show plan-view LOM images of the alloy interiors which were obtained following removal of at least 500 μm of material

from each alloy. The grains within each alloy interior were relatively equiaxed, with the AZ31B alloy containing a significantly larger average grain size than the AM30 alloy. The AM30 alloy also contained numerous twins, while no twinning was observed in the AZ31B alloy. The mean grain size of each alloy was determined using the Heyn lineal intercept procedure as described in ASTM E112-10 [76]. The mean grain sizes of the AZ31B and AM30 alloys with 95% confidence intervals were 13 ± 2 μm and 133 ± 19 μm, respectively. Intermetallic particles were observed in the LOM images of each alloy, and their presence was confirmed by their bright contrast observed under back-scattered electron SEM imaging (Figure 4.1[d] and Figure 4.2[d]).

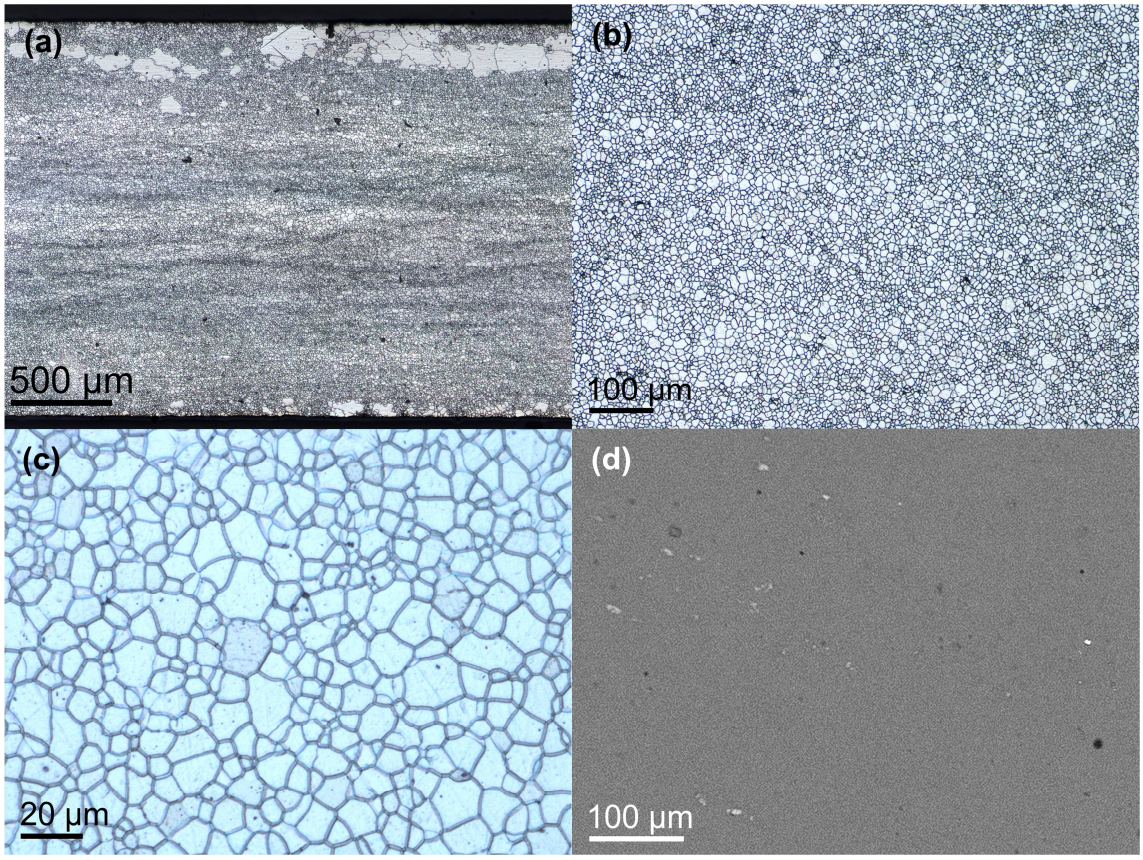

Figure 4.1: (a) Cross-sectional LOM image displaying the grain structure throughout the entire AZ31B alloy thickness, (b), (c) plan-view LOM images and (d) plan-view SEM back scattered electron image following removal of at least 500 µm of material from the AZ31B surface.

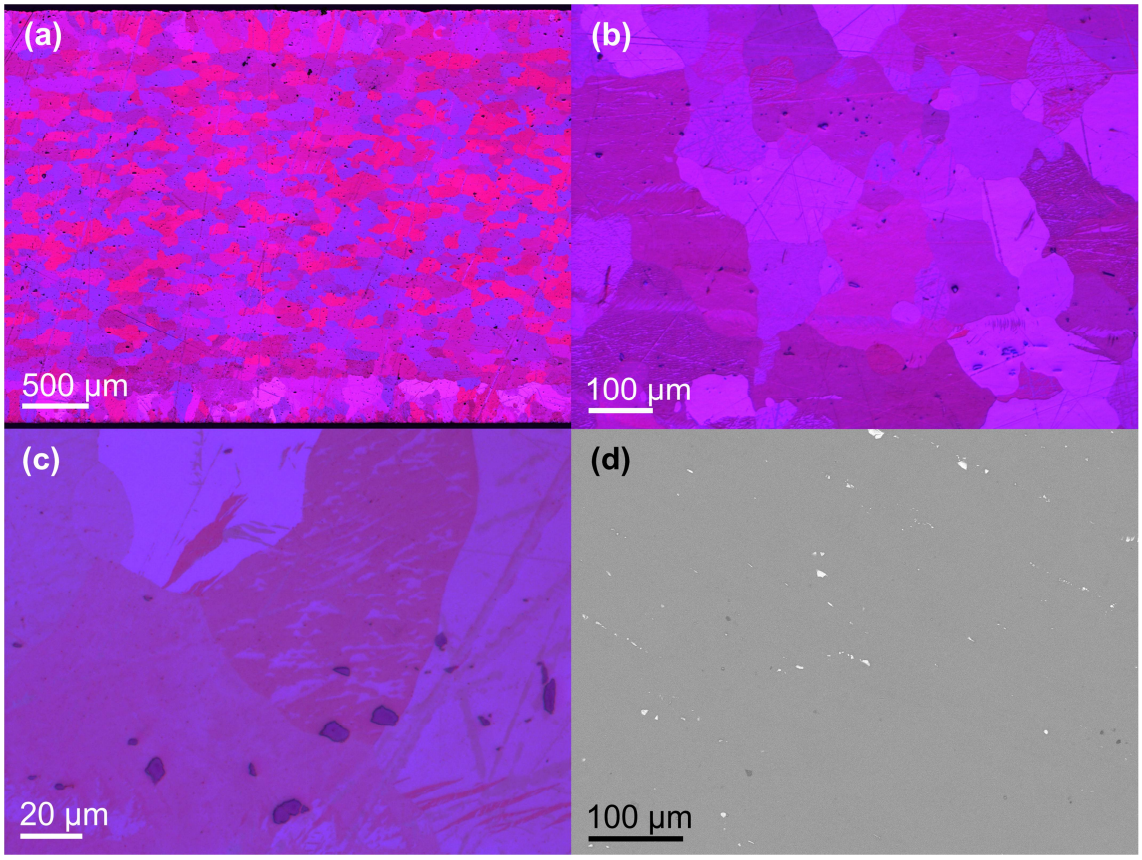

Figure 4.2: (a) Cross-sectional LOM image displaying the grain structure throughout the entire AM30 alloy thickness, (b), (c) plan-view LOM images and (d) plan-view back scattered electron SEM image following removal of at least 500 µm of material from the AM30 surface. The LOM images were captured with polarized light in order to display the grain structure more clearly.

Unless otherwise noted, plan-view sections with at least 500 µm of material removed from the top surfaces were employed for the tests subsequently described in Sections 4.2 and 4.3. This ensured that the tested alloy surfaces consistently possessed the interior grain structures observed in Figure 4.1(b,c) and Figure 4.2(b,c).

4.2. Electrochemical Characterization of Corrosion Behaviour

4.2.1. Open Circuit and Potentiodynamic Polarization Measurements

Al tape was used to attach steel wires to 5 mm × 5 mm plan-view sections of the AZ31B and AM30 alloys. The samples were individually mounted in epoxy such that only the plan-view surface opposite to the surface attached to the wire was left exposed (Figure 4.3). The exposed surface was then polished up to a 1200-grit finish using SiC paper with an ethanol lubricant. Fast-curing epoxy was applied around the edges of the exposed surface due to the noted tendency for localized corrosion to occur preferentially at the sample surface/epoxy mount interface.

Figure 4.3: Epoxy-mounted sample with wire attached and fast-curing epoxy applied around the edges of the exposed surface.

Open circuit and potentiodynamic polarization measurements were conducted on the mounted samples of each alloy using a standard three-electrode configuration. The exposed face of the sample acted as the working electrode, while a saturated calomel electrode was used as the reference electrode. Two graphite rods positioned on opposite sides of the sample were used as the counter electrodes. The electrodes were positioned in a corrosion cell with a mount holder fixed to its base, shown schematically in Figure 4.4(a). A photograph of the Uniscan Instruments Environmental TriCell™ used for this purpose is shown in Figure 4.4(b). This configuration was similar to that used for the localized electrochemical measurements (described in Section 4.2.2) which required the sample to lie in a horizontal plane. All open circuit and potentiodynamic polarization measurements were conducted with a Solartron 1287 potentiostat.

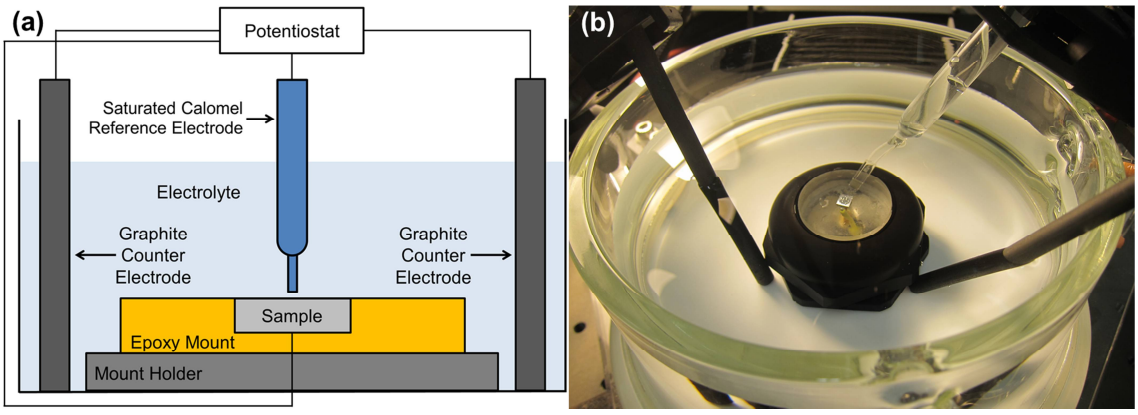

Figure 4.4: (a) Schematic representation and (b) photograph of the electrode setup used for open circuit and potentiodynamic polarization measurements.

An aqueous solution of 0.05 M NaCl at a near-neutral pH was selected as the electrolyte for all open circuit and potentiodynamic polarization measurements. This solution was selected such that corrosion filaments on each alloy initiated spontaneously within a convenient time period (typically between 1 to 5 h after sample immersion), with the corrosion filament propagation occurring slowly enough to allow reasonably spatially-resolved electrochemical measurements (described in Section 4.2.2). The solution was prepared from NaCl powder (Fisher Scientific, 99.0% min. assay) and deionized water naturally aerated with laboratory air at room temperature. The corrosion cell with all electrodes in position was filled with approximately 800 mL of the salt solution immediately prior to the beginning of electrochemical measurements.

The OCP of each alloy was measured for an immersion period of 24 h. In order to correlate the open circuit behaviour with the initiation and propagation of localized corrosion, the exposed surfaces were also monitored with a high-resolution video camera positioned directly above the corrosion cell.

Potentiodynamic polarization measurements of each alloy were conducted after immersion periods of 1 h and 24 h at the open circuit condition (OCC) with the purpose of investigating the anodic and cathodic kinetics on each alloy surface at two different stages of corrosion. The polarization measurements after 1 h at the OCC characterized the electrochemical kinetics prior to the initiation of localized corrosion, whereas the polarization measurements after 24 h at the OCC characterized the electrochemical kinetics after the alloy surfaces were significantly covered with corrosion filaments. For the 1 h polarization measurements, anodic and cathodic scans were completed separately using

freshly-prepared solutions and samples. For the 24 h polarization measurements, the anodic scans were completed following the cathodic scan on the same sample with an immersion period of 1 h at the OCC between the two scans. The electrode potential was swept from the OCP to a potential of -1.75 V_{SCE} for the cathodic scans and from the OCP to a potential of -1.35 V_{SCE} for the anodic scans, each with a scan rate of 0.1667 mV/s. Each polarization measurement was repeated three times for each alloy using freshly-prepared solutions and samples.

4.2.2. Localized Electrochemical Measurements

10 mm × 10 mm plan-view sections of the AZ31B and AM30 alloys were individually mounted in epoxy and polished up to a 1200-grit finish using SiC paper with an ethanol lubricant. Fast-curing epoxy was applied around the edges of the exposed surface to avoid preferential localized corrosion at the sample surface/epoxy mount interface. Each sample was immersed in a 0.05 M NaCl aqueous solution (prepared as described in Section 4.2.1) for a period of 24 h. During immersion, the evolution of spatially resolved ionic currents as a function of time were detected across the sample surface using SVET measurements taken as vectors normal to the exposed surface. For a brief explanation of the SVET, refer to Section 2.4.1. SVET measurements were performed using a Uniscan Instruments Model 370 Scanning Electrochemical Workstation and Environmental TriCell™. The electrode setup used for this technique is shown schematically in Figure 4.5(a) and a photograph of the setup is shown in Figure 4.5(b). Voltages were measured between the scan-

ning Pt tip and a graphite ground/reference electrode. The diameter of the Pt tip was specified by the manufacturer to be in the range of 5 to 50 µm. SVET scans were completed on a 6 mm × 6 mm area of the sample once every 1800 s (30 min) throughout the duration of the 24 h exposure period. The probe outputs were measured using a series of sweeping line scans across the scan area with a speed of 200 µm/s with a data point collected once every 150 µm. The probe was vibrated in the vertical direction with an amplitude of 30 µm and a frequency of 80 Hz. The gain of the electrometer was set to 10^4, and the full scale sensitivity of the lock-in amplifier was set to 160 µV.

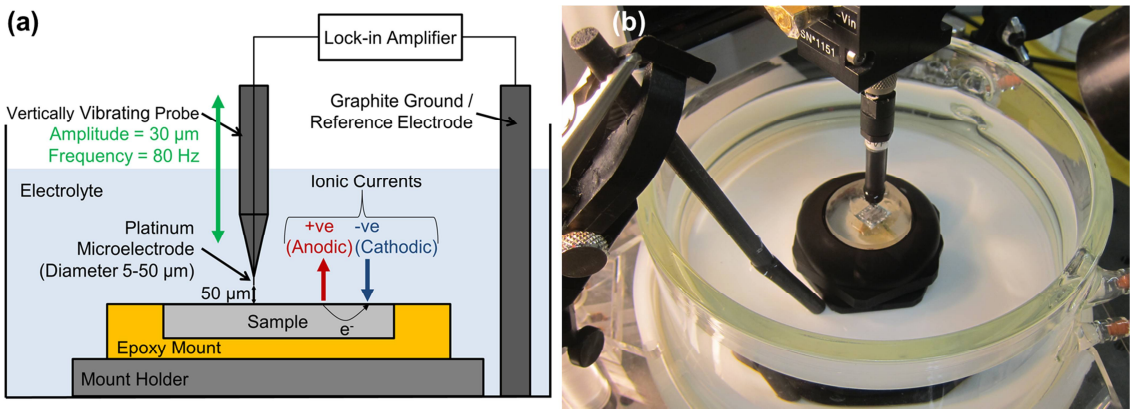

Figure 4.5: (a) Schematic representation and (b) photograph of the electrode setup used for SVET measurements.

In order to convert the measured voltages to ionic current density values, a calibration test similar to the one outlined by Williams and McMurray [12] was completed. The vibrating probe was first placed inside a tube with a known inner area. Using a polished gold (Au) working electrode immersed in a 0.05 M NaCl solution, a series of set

currents were passed through the tube and the vibrating probe output measured for each current. Plots of the probe output versus current density were constructed and a linear fit was applied with a R^2 value of 0.998. The resulting linear equation was used to convert the local probe outputs from each SVET scan into local ionic current densities.

The 24 h immersion test was repeated three times for each alloy using a freshly polished surface for each test. In order to relate the local ionic activity with the visual development of localized corrosion, the exposed surfaces were monitored with a high-resolution video camera positioned at an approximate 45° angle to the vertical during each test.

4.3. Physical Characterization of Corroded Structures

10 mm × 10 mm plan-view sections of the AZ31B and AM30 alloys were polished to a 1200-grit finish using SiC paper with an ethanol lubricant. Two samples of each alloy were immersed in separate Petri dishes containing a 0.05 M NaCl aqueous solution (prepared as described in Section 4.2.1). The first sample of each alloy was immersed for 3.5 h, which allowed localized corrosion to initiate and propagate for approximately 1-2 h. The second sample of each alloy was immersed for 19-21 h, which provided enough time for the entire sample surface to be covered by corrosion products.

4.3.1. Cross-Sectional Transmission Electron Microscopy (TEM)

A Zeiss NVision 40 FIB microscope was used to prepare thin-foil cross-sections from the corroded structures taken from three unique sites for each alloy. The locations of the three sites for AZ31B and AM30 are shown in Figure 4.6 and Figure 4.7, respectively. The first cross-section for each alloy was taken from an intact surface site (i.e. a site that had not been affected by a corrosion filament) on the sample immersed for 3.5 h. The corroded structures characterized from these cross-sections will be referred to as the "pre-existing surface films" in the following text, because they were assumed to be a derivative of the initial air-formed oxide films. The second cross-section for each alloy was also taken from the sample immersed for 3.5 h, and was taken near the head of a corrosion filament which was actively propagating before the sample was removed from the solution. The freshly formed corroded structures characterized from these cross-sections will be referred to as the "fresh corrosion filaments". The third cross-section for each alloy was taken from the sample immersed for 19-21 h, and was taken from the tail of a corrosion filament which had been in contact with the solution for approximately 11 h after its formation (determined from a high-resolution video recording). The corroded structures from these cross-sections will be referred to as the "aged corrosion filaments". Note that a protective tungsten (W) coating was applied to each site of interest before milling with the FIB in order to preserve the original morphology of the corroded structures. Each thin-foil cross-section was deposited onto a copper (Cu) grid before being placed in the TEM sample chamber.

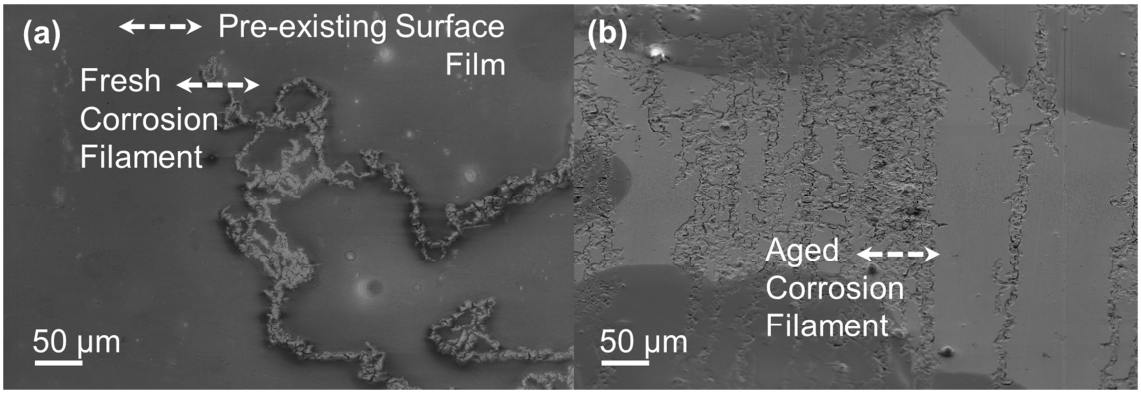

Figure 4.6: SEM plan view images displaying FIB cross-section locations from AZ31B immersed in a 0.05 M NaCl solution for (a) 3.5 h, (b) 19 h. The image in (a) is a back-scattered electron image and the image in (b) is a secondary electron image.

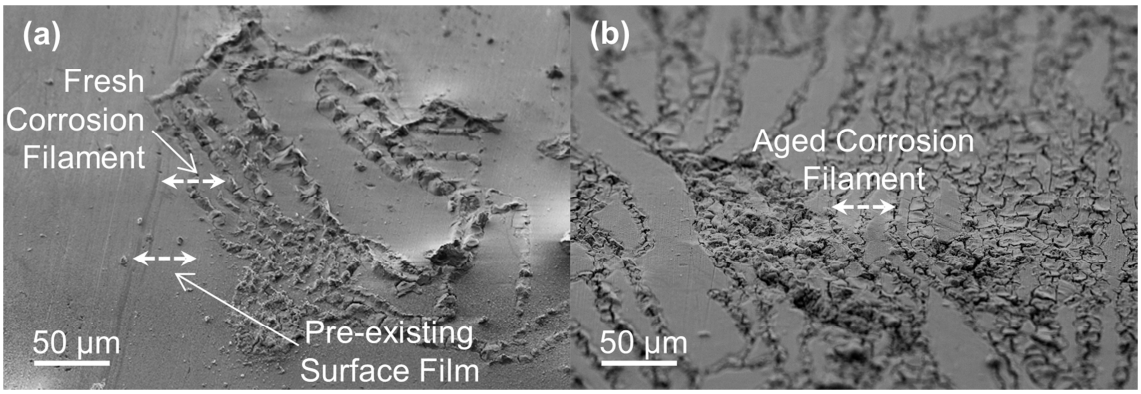

Figure 4.7: SEM secondary electron plan view images displaying FIB cross-section locations from AM30 immersed in a 0.05 M NaCl solution for (a) 3.5 h, (b) 21 h.

The AZ31B thin-foil cross-sections were examined using a FEI Titan 80-300 TEM/STEM operating at 300 keV and the AM30 thin-foil cross-sections were examined using a JEOL 2010F TEM/STEM operating at 200 keV. Both instruments were equipped with an Oxford Inca silicon (lithium drifted) [Si(Li)] detector EDS and a Gatan Image

Filter electron energy-loss spectrometer (EELS). All TEM examinations were conducted using a cryogenically-cooled stage (i.e. at 95 K) in order to minimize beam-induced damage of the corroded structures. The surface films were examined using bright field (BF) and dark field (DF) imaging along with selected area diffraction (SAD). The surface films were also characterized via STEM mode, with a HAADF detector utilized for imaging and EDS used to determine the composition of various microstructural features. EDS area maps and line profiles were acquired in order to identify elemental enrichment across the film/metal and filament/metal interfaces. Atomic compositions were also measured semi-quantitatively using the built-in standards (also known as k-factors [77]) of the EDS software. Low-loss EELS was used to clearly identify the metallic and non-metallic regions within the surface films, using the characteristic plasmon peaks for Mg [78] and $MgO/Mg(OH)_2$ [79]. Microstructural features of the underlying AZ31B and AM30 base metals were also characterized using the same thin-foil cross-sections.

4.3.2. Auger Electron Spectroscopy (AES) Depth Profiles

Site-specific AES depth profiles were collected from three unique sites of the corroded structures on each alloy with equivalent locations and immersion durations to those described in Section 4.3.1. The depth profiles were conducted primarily to obtain a reliable quantification of the proportion of O in each structure, since the collection efficiency of characteristic Auger electrons from light elements is superior to that of characteristic X-rays collected in EDS analysis [78].

All AES depth profiles were collected using a JEOL JAMP-9500F Field Emission Auger Microprobe. The electron beam had an accelerating voltage of 10 keV and a current of 40 nA, which allowed for a lateral resolution of approximately 30 nm. An Ar ion beam with an accelerating voltage of 3 keV was used for sputtering into the corroded structures. Specific energy ranges of the Auger spectra appropriate for the elements of interest (O, Mg, Al, Zn, Mn and Cl) were collected after each successive sputtering cycle. The sputtering time for each cycle was varied from 6 s to 20 s, with the lower sputtering time being used when approaching the surface film/metal interfaces. The Auger spectra were then quantified in order to determine the atomic compositions as a function of sputtering time into the corroded structures.

Chapter 5: Results

In Section 5.1 of this chapter, the open circuit and potentiodynamic polarization measurements for Mg alloys AZ31B and AM30 are presented together in order to allow for a direct comparison of these results. The rest of the results are separated into individual sections for each alloy due to the relative complexity of their presentation. The localized electrochemical measurements and microstructure/corroded structure characterization results for AZ31B are presented in Section 5.2 and the respective results for AM30 are presented in Section 5.3.

5.1. General Corrosion Characteristics of Mg Alloys AZ31B and AM30

5.1.1. Open Circuit Measurements

Plots of the OCP of each alloy as a function of immersion time in a 0.05 M NaCl solution are shown in Figure 5.1. For both alloys, the OCP typically increased from approximately -1.7 V_{SCE} to -1.6 V_{SCE} within the first 100 s after immersion and continually increased thereafter at a more gradual rate. After an immersion time typically within the range of 1-5 h, a sudden drop of the OCP was observed. This event coincided with the initiation of a dark corrosion filament at a specific location of the surface and the observance of H_2

bubbles evolving from this same location. After this initiation (i.e. breakdown) event, relatively large fluctuations of the OCP were observed as the surface became increasingly covered by the corrosion filaments. The plots shown in Figure 5.1 were selected from the sample of each alloy that displayed the longest time delay prior to breakdown, in order to demonstrate that a stabilized OCP was never established before suddenly dropping at breakdown.

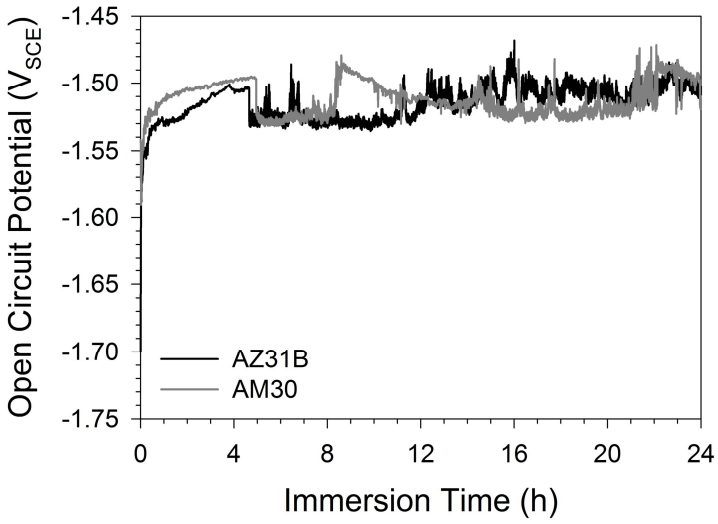

Figure 5.1: Plots of the OCP of AZ31B and AM30 alloys as a function of immersion time in a 0.05 M NaCl solution.

Prior to the initiation of corrosion filaments, slightly higher OCP values were observed on the AM30 alloy than on the AZ31B alloy (at equal time periods), as seen in Figure 5.1. This was consistently observed during the three repeat OCP measurements on each alloy, with the AM30 alloy attaining an average OCP approximately 20 mV higher than the AZ31B alloy after 1 h of immersion (refer to Table 5.1 at the end of Section 5.1).

However, the average OCP value attained after 24 h of immersion was approximately 10 mV higher on the AZ31B alloy than on the AM30B alloy (Table 5.1). The time until breakdown at the OCC was not determined to differ significantly between the two alloys (Table 5.1).

A sequence of images of the surface of each alloy as a function of immersion time at the OCC is shown in Figure 5.2. These images were taken while recording the OCP values plotted in Figure 5.1. The surfaces of both alloys became noticeably lighter in colour within the first 30 min of immersion, perhaps indicative of an aqueous film growth corresponding to the increase of the OCP as a function of immersion time prior to breakdown. Corrosion filaments can be observed on the surfaces of both alloys following the 6 h mark in Figure 5.2. The corrosion filaments on AZ31B tended to be congregated closer together than on AM30, which is attributed to the finer grain size of the AZ31B alloy. The corrosion filaments appeared to propagate across the surface at an equal linear rate on both alloys within the first couple of h following breakdown. However, after immersion times longer than approximately 10 h, the filament growth on the AZ31B surface was noticeably more severe than on the AM30 surface. This resulted in a significantly higher population of corrosion filaments on the AZ31B surface at the end of the 24 h immersion period. It was also noted that, after forming, the corrosion filaments on both alloys became noticeably lighter in colour as they aged in the solution. This could be more easily observed on the AM30 surface due to the lower growth rate of new filaments; for example, the same cluster of filaments that formed on the upper-left portion of the AM30 surface after 8 h appeared noticeably brighter after 20 h.

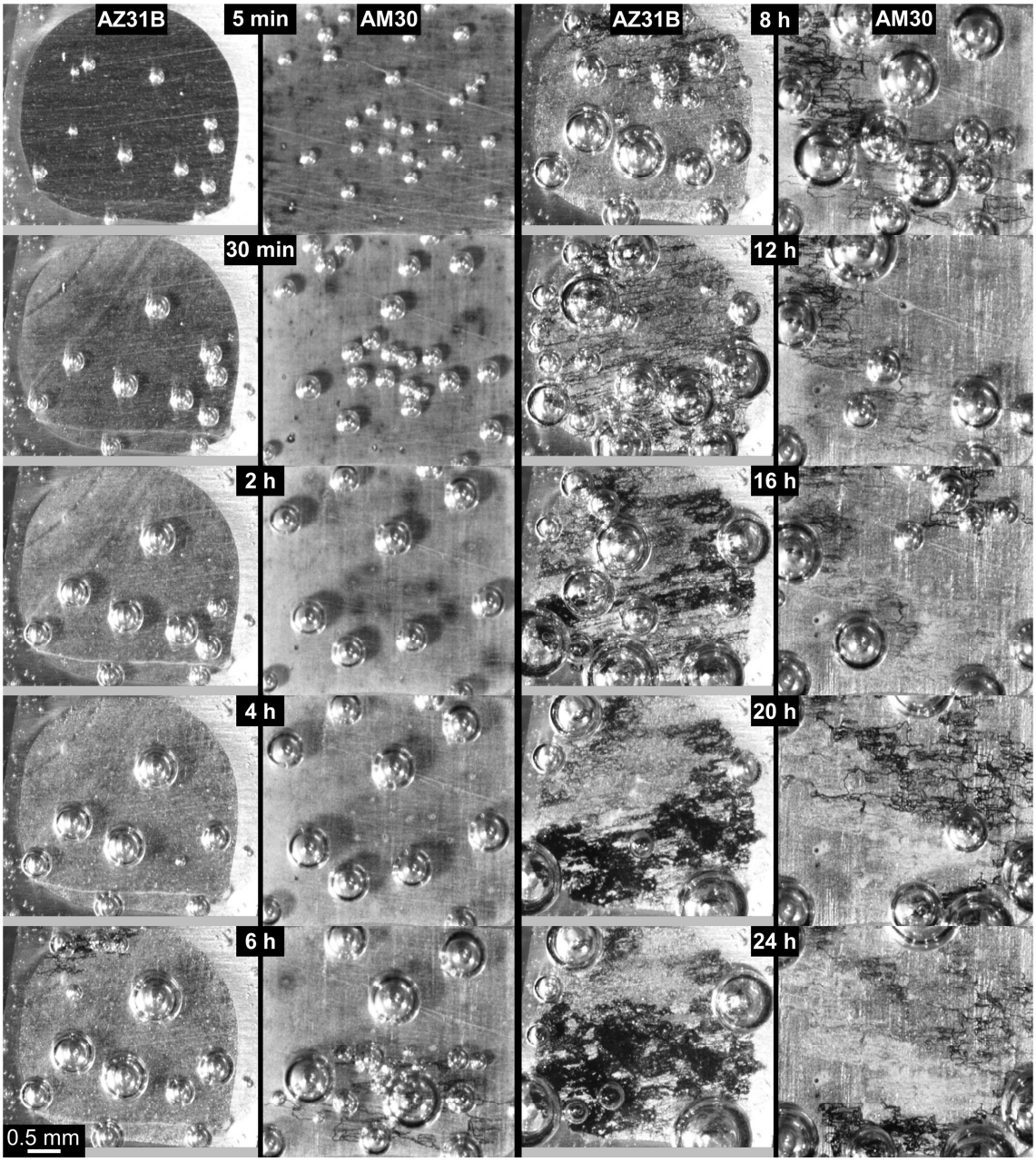

Figure 5.2: Surface images of AZ31B and AM30 alloys as a function of immersion time at the OCC in a 0.05 M NaCl solution. Images were taken while recording the OCP values plotted in Figure 5.1.

5.1.2. Potentiodynamic Polarization Measurements

Representative potentiodynamic polarization curves for both alloys after 1 h of immersion at the OCC are presented in Figure 5.3. These measurements demonstrated the anodic and cathodic kinetics on the alloy surfaces prior to breakdown, since no corrosion filaments initiated within 1 h of immersion at the OCC. The anodic and cathodic kinetics appeared to be relatively similar on each alloy surface, although slightly increased cathodic kinetics were apparent for the AM30 alloy. However, the average cathodic current density at a potential chosen within the linear portion of the cathodic curves (-1.6 V_{SCE}) was not significantly higher for the AM30 alloy ([81.7 ± 28.5] × 10^{-6} A/cm^2) than for the AZ31B alloy ([47.4 ± 15.0] × 10^{-6} A/cm^2). The anodic polarization curves for each alloy displayed a breakdown potential (E_b), above which the anodic current density rapidly increased as a function of applied potential. The average values of E_b for the AZ31B and AM30 alloys were -1.417 ± 0.131 V_{SCE} and -1.423 ± 0.043 V_{SCE}, respectively, and therefore were not found to differ significantly. The average corrosion current density (i_{corr}) was calculated by extrapolating the linear portion of the cathodic curves to the E_{corr} of each sample. The average i_{corr} values for AZ31B and AM30 with 95% confidence intervals were (12.7 ± 5.4) × 10^{-6} A/cm^2 and (17.6 ± 6.3) × 10^{-6} A/cm^2, respectively, and therefore were also not found to be significantly different from each other.

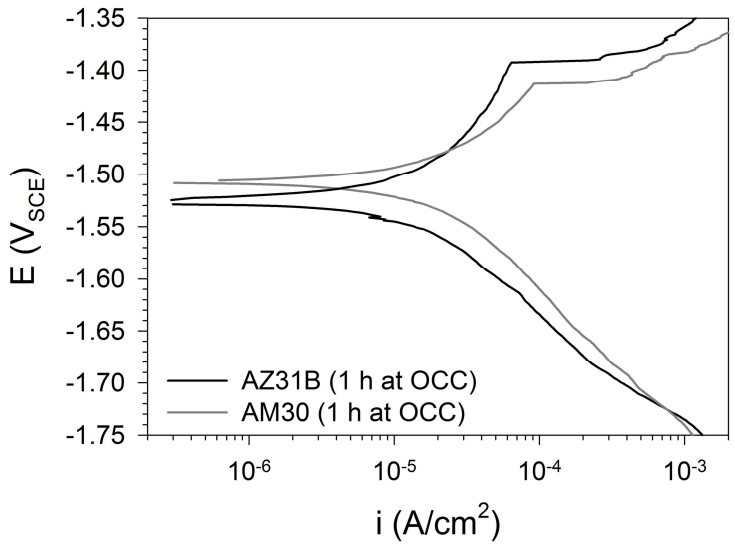

Figure 5.3: Representative potentiodynamic polarization curves for AZ31B and AM30 recorded after 1 h at the OCC in a 0.05 M NaCl solution.

Representative potentiodynamic polarization curves for both alloys following 24 h of immersion at the OCC are presented in Figure 5.4. The cathodic kinetics on both alloys appeared to increase relative to the alloys after only 1 h of immersion at the OCC. Significantly larger cathodic current densities were observed on the AZ31B surface after 24 h of immersion at the OCC ([158 ± 38.7] × 10^{-6} A/cm^2) compared to after 1 h of immersion at the OCC ([47.4 ± 15.0] × 10^{-6} A/cm^2). By contrast, the cathodic current densities observed on the AM30 surface after 24 h of immersion at the OCC ([110 ± 35.0] × 10^{-6} A/cm^2) were not significantly higher than that after 1 h of immersion at the OCC ([81.7 ± 28.5] × 10^{-6} A/cm^2). For every anodic scan, higher anodic kinetics were apparent on the AZ31B surface relative to the AM30 surface after 24 h of immersion at the OCC, which was consistent with the higher population of corrosion filaments observed on the AZ31B

surface after 24 h (Figure 5.2). However, the anodic current density values were too varied to make this observation statistically significant. The average i_{corr} values for the AZ31B and AM30 alloys following 24 h of immersion at the OCC were (54.5 ± 22.0) × 10^{-6} A/cm^2 and (23.3 ± 10.4) × 10^{-6} A/cm^2, respectively. Therefore, as was the case for the cathodic current densities, only the i_{corr} for AZ31B significantly increased from 1 h to 24 h at the OCC.

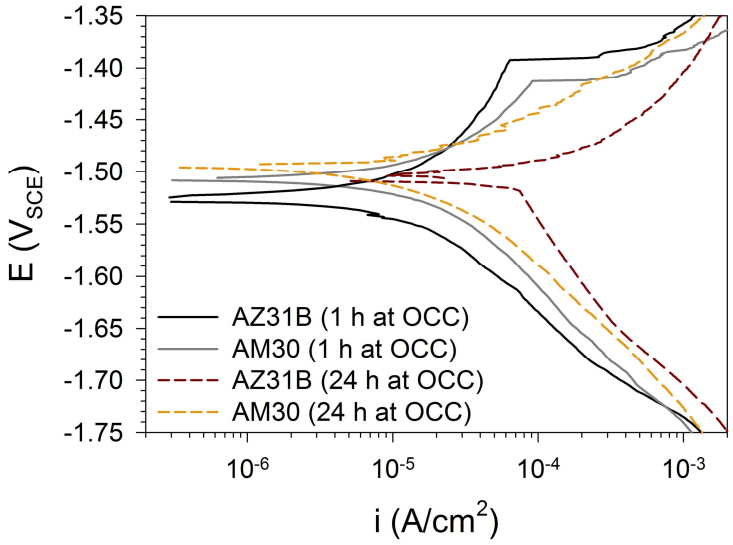

Figure 5.4: Representative potentiodynamic polarization curves for AZ31B and AM30 recorded after 24 h at the OCC in a 0.05 M NaCl solution. Curves recorded after 1 h at the OCC (Figure 5.3) are superimposed for reference.

Table 5.1: Average corrosion parameters with 95% confidence intervals determined from OCP and potentiodynamic polarization measurements in a 0.05 M NaCl solution. The time until breakdown is presented as individually determined values because the confidence interval for its average was unacceptably large.

	AZ31B (1 h at OCC)	AM30 (1 h at OCC)	AZ31B (24 h at OCC)	AM30 (24 h at OCC)
Final OCP (V_{SCE})	-1.527 ± 0.005	-1.509 ± 0.004	-1.499 ± 0.008	-1.513 ± 0.001
Time until breakdown (h)	-	-	3.22, 2.44, 4.66	1.75, 4.95, 2.21
E_b (V_{SCE})	-1.417 ± 0.131	-1.423 ± 0.043	-	-
i_{corr} ($A/cm^2 \times 10^{-6}$)	12.7 ± 5.4	17.6 ± 6.3	54.5 ± 22.0	23.3 ± 10.4
i_c at -1.6 V_{SCE} ($A/cm^2 \times 10^{-6}$)	47.4 ± 15.0	81.7 ± 28.5	158 ± 38.7	110 ± 35.0

5.2. Localized Corrosion of Mg Alloy AZ31B

5.2.1. Localized Electrochemical Measurements

Selected SVET maps recorded during immersion of the AZ31B sample in a 0.05 M NaCl solution are presented in Figure 5.5 as a function of immersion time. Images of the scan area at corresponding immersion times are also provided alongside the SVET maps. It is important to note that the SVET maps presented in this work are not completely time-resolved, since the anode and cathode locations sometimes moved appreciably during the time required to complete one scan (approximately 25 min). In light of this, either the

SVET scan immediately after or prior to each indicated immersion time was selected for presentation based on whether the bottom half of the scan area (i.e. the first half scanned) or the top half (i.e. the second half scanned) was of higher interest. In addition, it was noted during SVET testing that the initiation of corrosion filaments generally occurred earlier than during the OCP measurements discussed in Section 5.1.1. This was perhaps due to the increased solution convection caused by the repeated scanning of the SVET probe, as well as the fact that the Pt tip on the probe tended to remove H_2 bubbles stuck to the alloy surface that would have otherwise isolated parts of the surface from the solution. However, the morphology and linear propagation rate of the corrosion filaments following localized breakdown did not appear to be affected by the SVET probe movement.

For the SVET test presented in Figure 5.5, localized corrosion sites were initiated within the first 30 min of immersion, evidenced by local anodic peaks with evolution of H_2 bubbles at the corresponding locations (Figure 5.5[a]). Multiple corrosion filaments propagated laterally from these locations towards the bottom half of the scan area, with anodic peaks and HE observed at the moving fronts of the corrosion filaments (Figure 5.5[b,c]). In addition, cathodic currents could be observed in the dark areas left behind by the corrosion filaments (Figure 5.5[c]). After approximately 8 h of immersion, a second set of corrosion filaments initiated near the top of the scan area and propagated downwards across the areas already consumed by the first set of corrosion filaments (Figure 5.5[d-f]). The anodic currents at the fronts of the second set of corrosion filaments and the cathodic currents left behind by these filaments were both noticeably larger in magnitude than for the first set of corrosion filaments. After approximately 17 h of immersion, a

third set of corrosion filaments initiated near the top of the scan area and again propagated across the areas already consumed by prior filaments (Figure 5.5[g,h]).

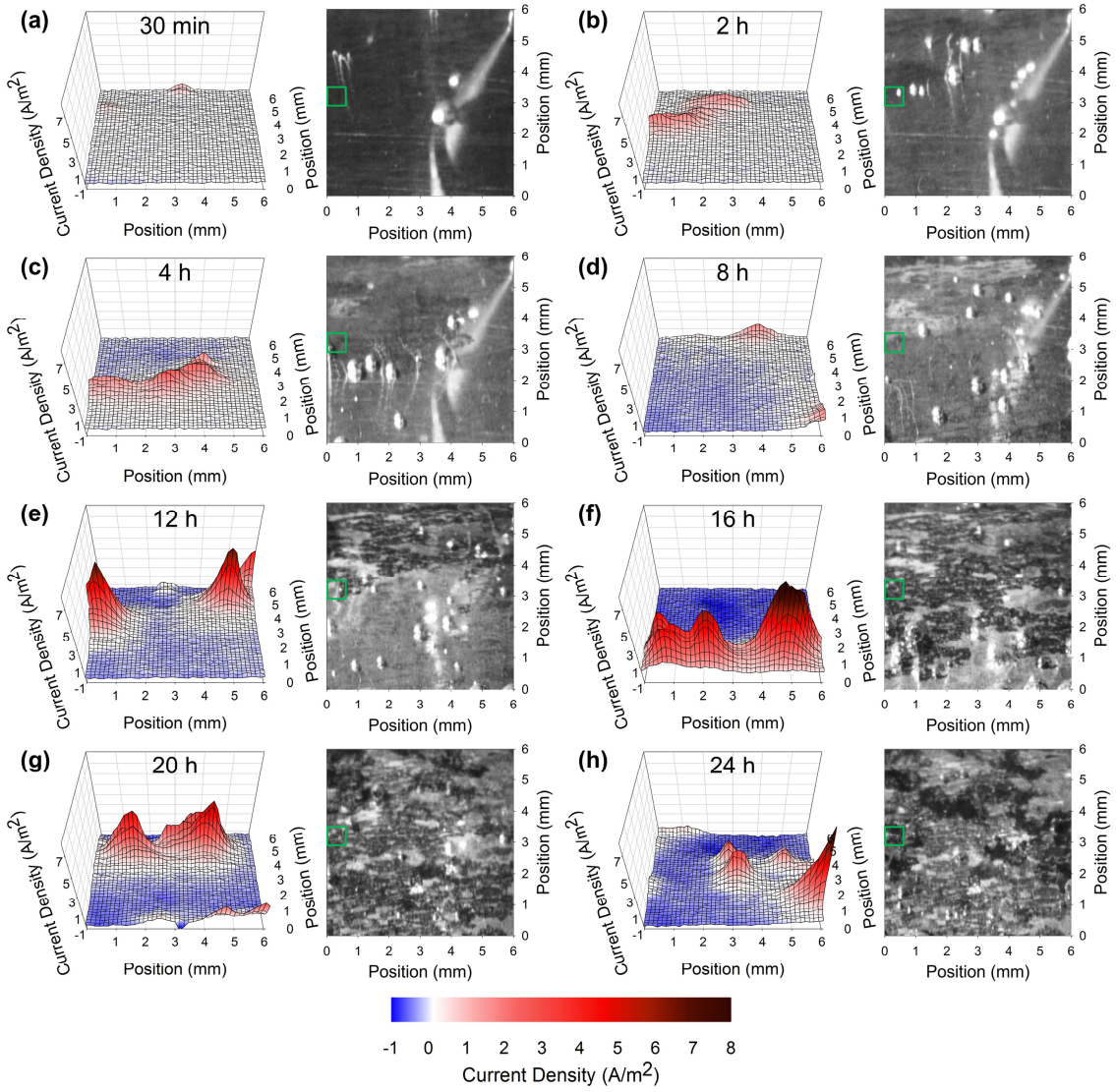

Figure 5.5: Selected SVET plots and scan area images of the AZ31B sample at various times after immersion in a 0.05 M NaCl solution. Note that the streak of light sometimes visible on the right half of the scan area images was caused by the reflection of the SVET probe on the alloy surface.

In order to demonstrate cathodic current variations of a specific region of the alloy surface as a function of immersion time, the average magnitudes of the anodic and cathodic current densities within a 0.6 mm × 0.6 mm area outlined by the small squares in the scan area images of Figure 5.5 are shown in Figure 5.6. It can be seen that after the first pass of filaments (indicated by the large average anodic current densities) from approximately 0-4 h this area became dominated by cathodic currents with relatively stable magnitudes with respect to time. After the second pass of filaments from approximately 10-12 h, comparatively larger cathodic currents dominated this area until a third set of filaments passed across the area.

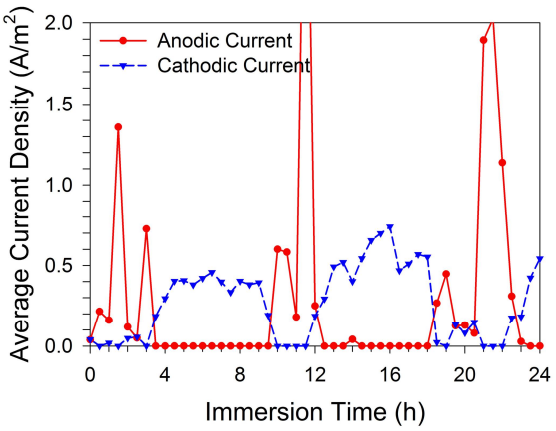

Figure 5.6: Average current density values within the area outlined by the small squares in the scan area images in Figure 5.5.

In order to estimate the magnitudes of localized anodic and cathodic currents developed across the entire scan area as a function of immersion time, the individual current

densities for each SVET map were integrated according to the following equations as per Williams and McMurray [12]:

$$I_{a_t} = \int_0^Y \int_0^X [i_{z(x,y)} > 0] dx dy \tag{5.1}$$

$$I_{c_t} = \int_0^Y \int_0^X [i_{z(x,y)} < 0] dx dy \tag{5.2}$$

where I_{a_t} and I_{c_t} are the total anodic and cathodic currents detected across the scan area, X and Y are the dimensions of the scan area and $i_{z(x,y)}$ corresponds to each individual SVET-measured current density. This resulted in plots of integrated current representing the total localized current detected with SVET versus immersion time as shown in Figure 5.7. The anodic currents in these plots should ideally be equal to the cathodic currents at each time in order to satisfy the conservation of charge. Deviations of the respective currents likely resulted from the limited spatial resolution of the SVET measurements as well as the fact that the SVET scan area did not encompass the entire exposed sample area. Nevertheless, it can be observed in Figure 5.7 that the general increase in integrated anodic current as a function of time was accompanied by a general increase in integrated cathodic current. This trend was consistent across the three 24 h immersion tests of freshly-polished alloy surfaces. In order to test if grain size had an effect on the localized anodic and cathodic kinetics, an SVET experiment of a coarse-grained AZ31B sample obtained by removing approximately 100 μm of material from the top surface of a plan-view sec-

tion (refer to Figure 4.1[a] for the coarse grain structure) was also carried out. As shown in Figure 5.8, the integrated anodic and cathodic kinetics on the coarse-grained sample as a function of immersion time appeared similar in magnitude to those in Figure 5.7.

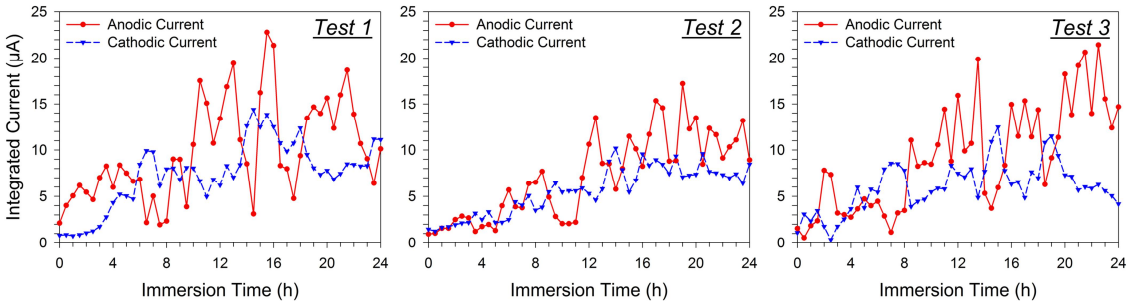

Figure 5.7: Integrated currents across the SVET scan area for AZ31B as a function of immersion time in a 0.05 M NaCl solution. Each plot was derived from a separate 24 h immersion test of a freshly polished alloy surface. The first plot was derived from the same test as Figure 5.5 and Figure 5.6.

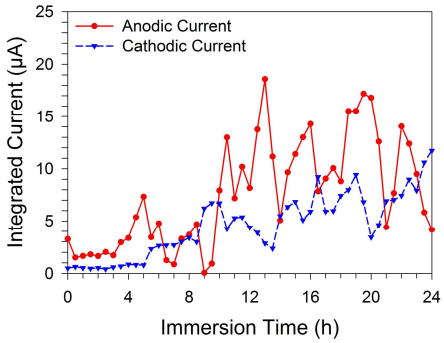

Figure 5.8: Integrated currents across the SVET scan area for a coarse-grained AZ31B sample as a function of immersion time in a 0.05 M NaCl solution.

5.2.2. Microstructure / Corroded Structure Characterization

5.2.2.1. AZ31B Microstructure

The AZ31B microstructure observed from the FIB-prepared thin-foil cross-sections contained fine round particles with an average diameter ($\bar{D}$) of 12.7 ± 4.3 nm (Figure 5.9[a,b]). The volumetric number density (N_V) of the fine particles was estimated to be 6500 per μm^3 of metal, which was determined by measuring the average planimetric number density (N_A) of fine particles in five separate TEM micrographs and applying the following equation [80]:

$$N_v = N_A / \bar{D} \tag{5.3}$$

Coarse particles with sizes on the order of microns were also scarcely observed in the AZ31B microstructure (Figure 5.9[a]), which likely corresponded to the particles observed with SEM imaging (Figure 4.1[d]). EDS spot analyses of the matrix phase and particles revealed that both types of particles (fine and coarse) were enriched with Al and Mn (Figure 5.9[c,d]). At least six spot analyses were completed in each of the matrix phase and individual fine and coarse particles, with all of the results proving to be consistent with Figure 5.9(c,d). The Mg and Zn peaks in the EDS spectra for the fine and coarse particles were assumed to originate from the surrounding matrix phase since the EDS interaction volume was not solely confined to the targeted particles. Also, the Cu peaks in

these spectra and all spectra hereafter originated from the TEM sample grid and should not be interpreted as originating from the thin-foil cross-sections themselves. None of the analyzed particles were identified as the β-$Mg_{17}Al_{12}$ phase.

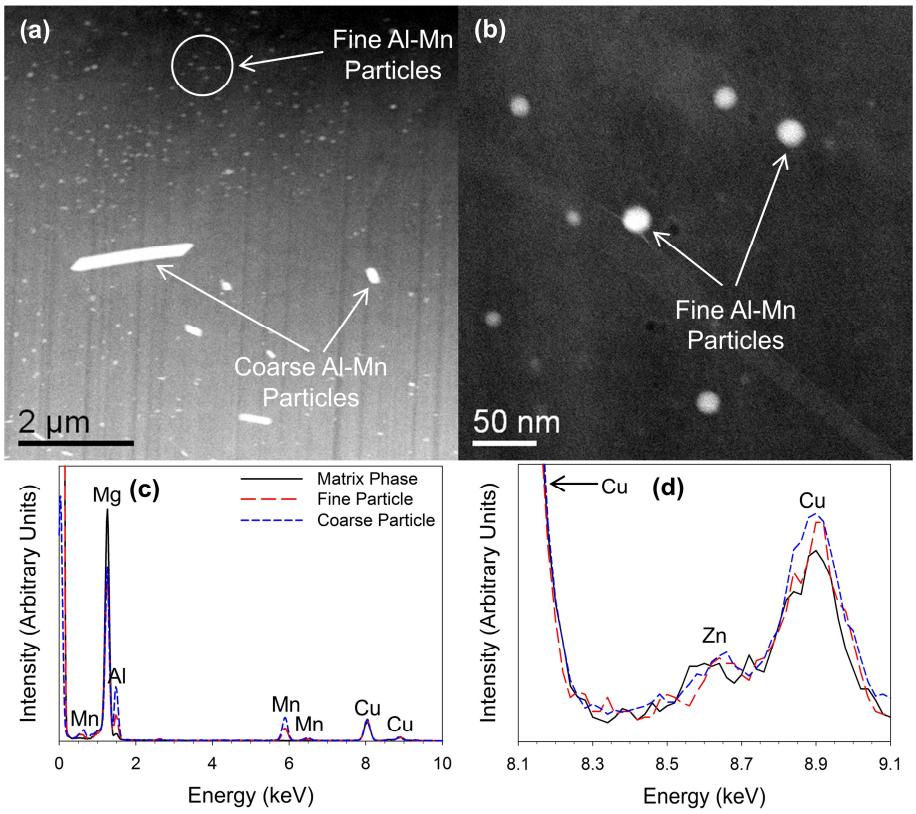

Figure 5.9: (a) HAADF-STEM image of fine and coarse-sized particles found in the AZ31B microstructure, (b) high-magnification HAADF-STEM image of the fine-sized particles, (c) typical EDS spectra from matrix phase, fine particles and coarse particles, (d) EDS spectra from (c) magnified to display Zn peaks.

EDS quantification was performed on six particles of each type (fine and coarse) and the Al:Mn atomic ratios were calculated from these measurements (Table 5.2). The

Al:Mn atomic ratios were overestimated in the original quantification results because the surrounding matrix, which contained Al in solid solution, was included in the EDS interaction volume. In order to determine a more realistic Al:Mn ratio for the particles, the Mg signal detected from the EDS measurement was assumed to originate entirely from the matrix. Thus, a portion of the quantified at.% of Al corresponding to the quantified at.% of Mg from the EDS measurement was subtracted in the same proportions as the Al present in the matrix (i.e. ~2.5 at.% Al, obtained via EDS quantification of the matrix, which translates into Al:Mg = 0.0256). The corrected Al:Mn ratio was calculated after this adjustment was applied. The mean Al:Mn atomic ratios for the fine and coarse particles were 2.53 +/- 0.58 and 2.69 +/- 0.32, respectively, which were both significantly higher than the maximum range of 1.1 to 1.8 which would be expected of the thermodynamically stable Al_8Mn_5 phase at 650°C or below [81]. Rather, these corresponded more closely to the ratio of 2.75 expected for the stoichiometric $Al_{11}Mn_4$ phase [81]. Nevertheless, these particles will simply be referred to as Al-Mn particles in the below text.

Table 5.2: Corrected atomic ratios calculated from EDS quantification of Al-Mn particles in the AZ31B microstructure.

Fine Al-Mn Particles		Coarse Al-Mn Particles	
Particle #	Al:Mn atomic ratio	Particle #	Al:Mn atomic ratio
1	2.68	1	2.64
2	2.10	2	2.70
3	2.83	3	2.96
4	2.09	4	2.64
5	3.42	5	2.10
6	2.07	6	3.09
Mean (95% Confidence)	2.53 (+/- 0.58)	Mean (95% Confidence)	2.69 (+/- 0.32)

5.2.2.2. Pre-existing Surface Film

A BF-TEM image of the pre-existing surface film (i.e. an intact surface not affected by a corrosion filament) is shown in Figure 5.10(a). The variations in contrast observed throughout the film were indicative of its porous morphology. The thickness of the film varied significantly along the length of the thin-foil cross-section, ranging from approximately 50 to 120 nm and with an average thickness of 84 ± 5 nm. The SAD pattern of the pre-existing film is shown in Figure 5.10(b). The spots in the diffraction pattern were indexed as hexagonal close packed (HCP) Mg, which were present because the SAD collection area included both the film and the underlying AZ31B metal. The relatively broad diffraction rings matched well with the cubic MgO (200) and (220) rings, which suggested that the pre-existing film consisted of nanocrystalline MgO. A DF-TEM image collected from the diffraction rings of the SAD pattern caused the pre-existing film to appear brighter (Figure 5.10[c]). In the same DF-TEM image, crystallites of MgO on the underlying AZ31B metal are also highlighted. The MgO SAD signal, therefore, originated from both the pre-existing surface film and the MgO layer formed on the FIB-prepared cross-section. A second DF-TEM image, collected from one of the Mg $(\bar{1}103)$ diffraction spots, caused a thin, elongated grain at the metal surface to appear brighter (Figure 5.10[d]). This is consistent with the presence of multiple Mg zone axes that were observed in the SAD pattern (Figure 5.10[b]).

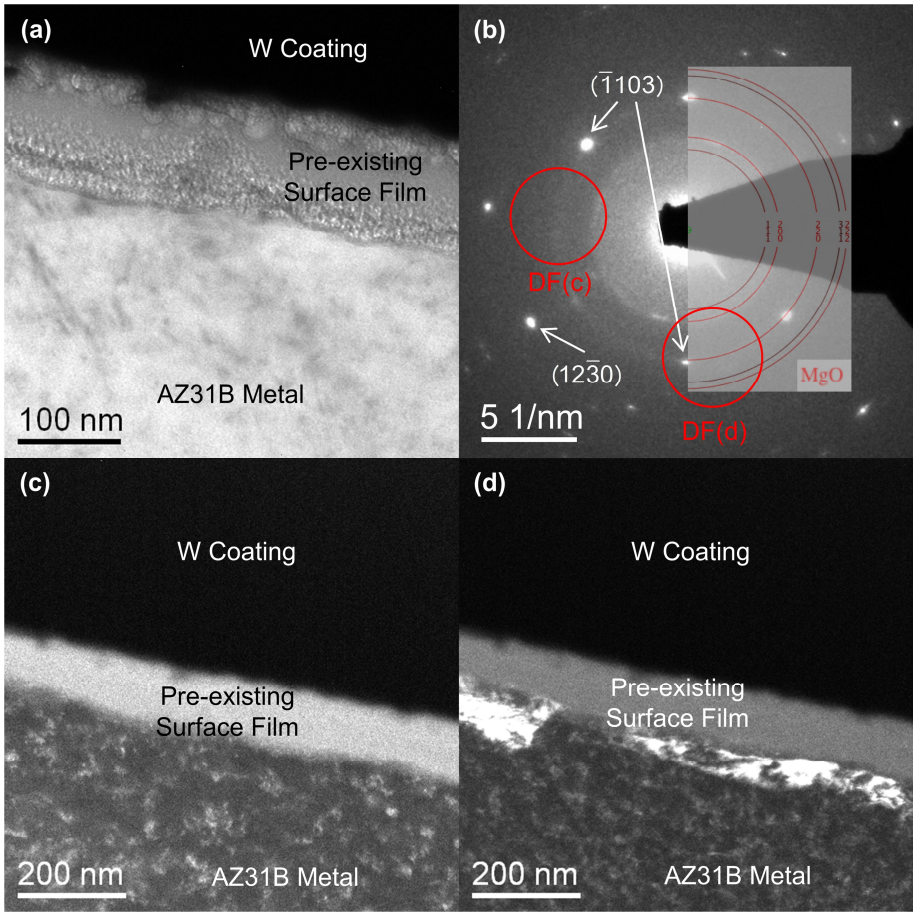

Figure 5.10: (a) BF-TEM image of the pre-existing surface film on AZ31B in cross-section after immersion in a 0.05 M NaCl solution for 3.5 h, (b) SAD pattern collected from the area in (a) (collection area was larger than the imaged area); the diffraction spots were indexed to the $(\bar{1}103)$ and $(12\bar{3}0)$ planes of HCP Mg while the diffraction rings were indexed to the (200) and (220) planes of cubic MgO, (c) (d) DF-TEM images of the pre-existing surface film obtained from the corresponding marked areas in (b).

The pre-existing surface film imaged with HAADF-STEM is shown in Figure 5.11. The fine Al-Mn particles present in the AZ31B metal (Figure 5.9) were also observed within the pre-existing surface film (Figure 5.11[a]). EDS point identification revealed a Zn peak at the film/metal interface (Figure 5.11 [b,c]) that was more intense than for the alloy matrix phase (Figure 5.9[d]). EDS maps confirmed an enrichment of Zn at the pre-existing film/metal interface (Figure 5.12). A line profile traversing across the interface was extracted from the EDS maps and the elemental intensities were converted semi-quantitatively to atomic percentages. The line profile for Zn indicated that its atomic concentration approximately doubled at the interface relative to the alloy matrix and film. The EDS maps also indicated that Al and Cl were present in the pre-existing film. Note that the quantification of the proportion of O from EDS quantification was considered to be unreliable due to the generally poor collection efficiency of elements with atomic numbers less than 11 [82].

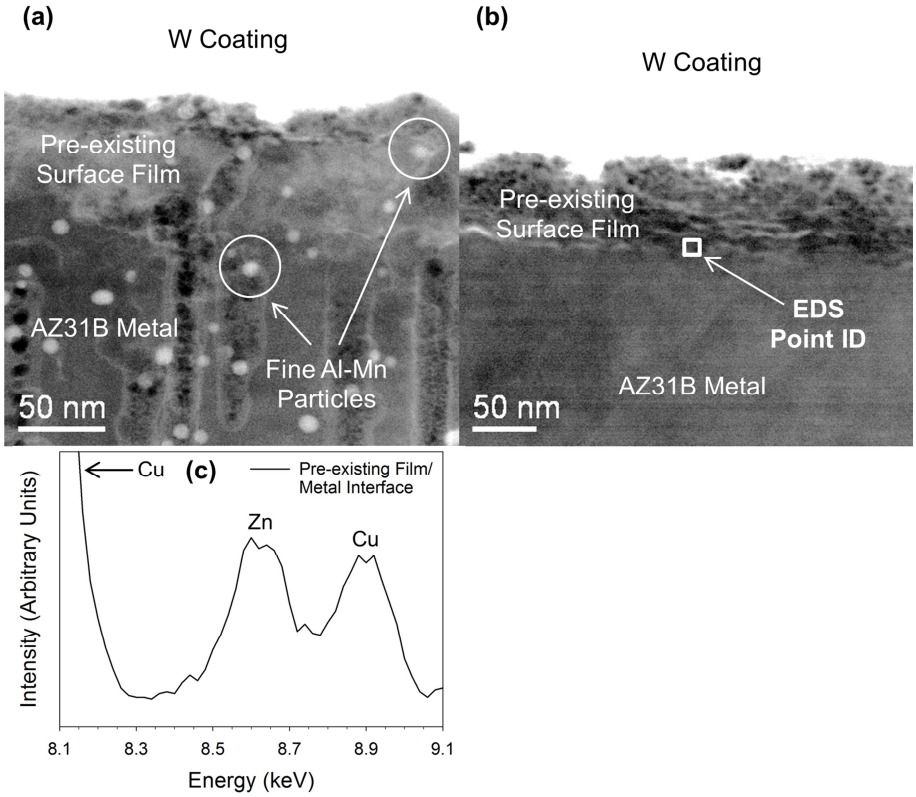

Figure 5.11: (a) HAADF-STEM image of the pre-existing surface film on AZ31B in cross-section revealing the presence of fine Al-Mn particles (note that the dark holes in the film and metal were artifacts caused by the Ga ions used for FIB milling) (b) HAADF-STEM image of the pre-existing surface film in cross-section, (c) EDS point identification spectrum from the location marked in (b), magnified to display the Zn peak.

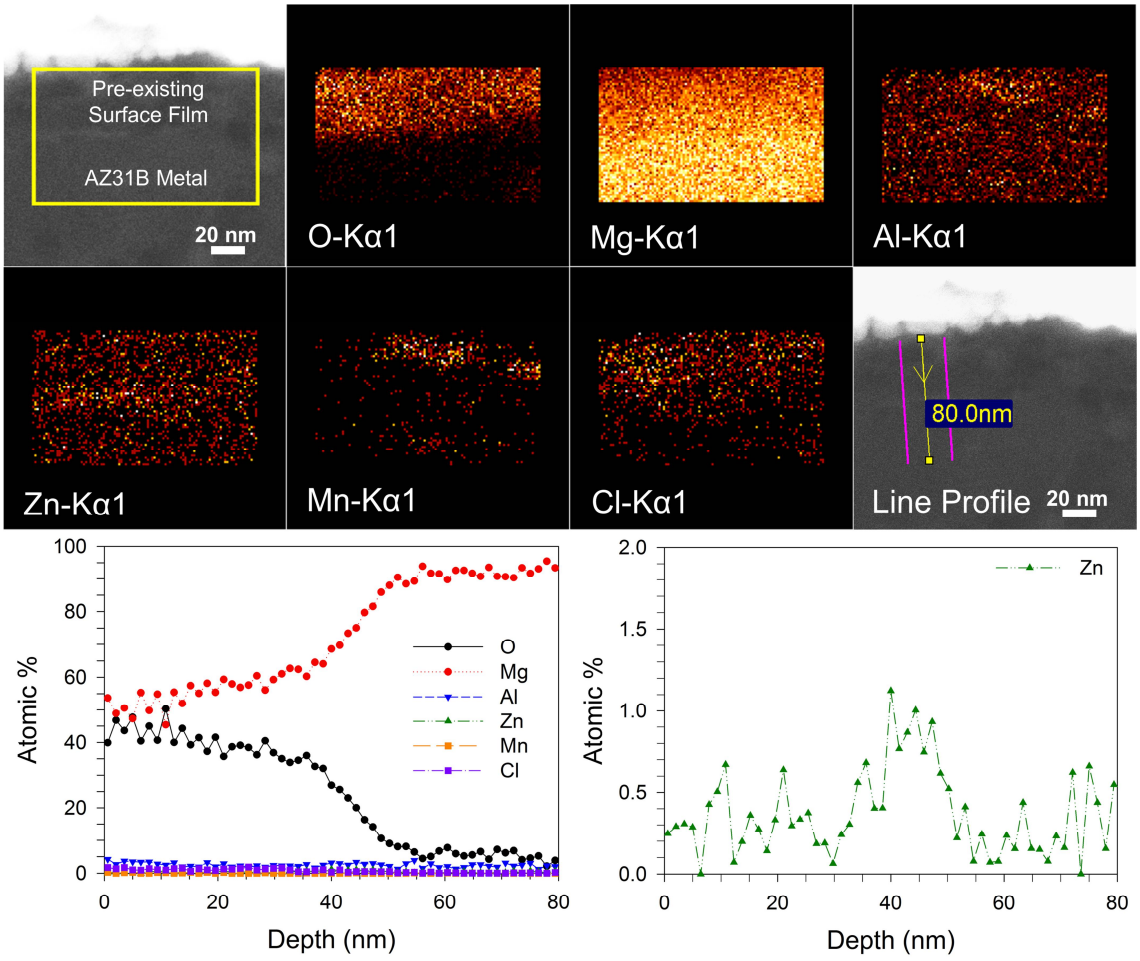

Figure 5.12: EDS maps and line profile displaying O, Mg, Al, Zn, Mn and Cl distribution across the pre-existing film/metal interface on AZ31B. The line profile was summed across ten adjacent lines of pixels located between the marked outer lines.

The AES depth profile through the pre-existing surface film (Figure 5.13) revealed an O:Mg atomic ratio very close to 2:1, which was indicative of a $Mg(OH)_2$ corrosion product and contradicted the SAD result indicating a MgO crystal structure (Figure 5.10[b]). The AES depth profile also provided further evidence that the pre-existing film contained Al and also showed a higher Al concentration at the top surface of the film.

However, the Zn-enrichment detected with EDS at the pre-existing film/metal interface (Figure 5.12) was not revealed by the AES depth profile, perhaps because it was destroyed by the sputtering process.

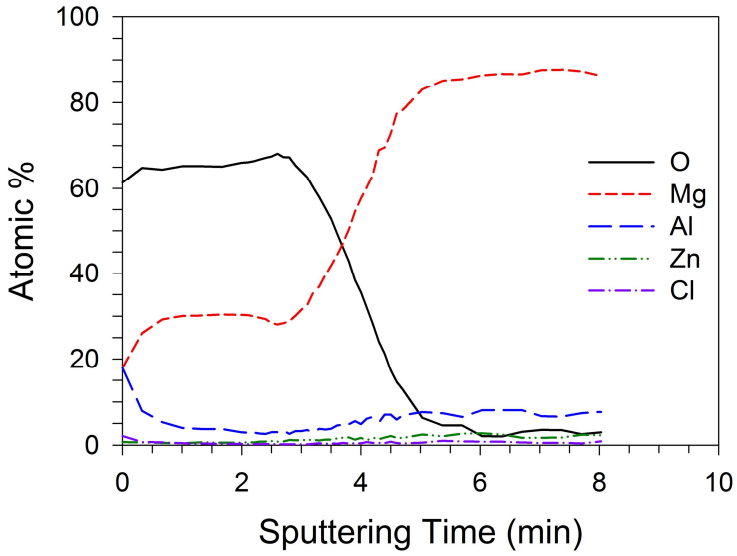

Figure 5.13: AES depth profile through the pre-existing surface film on AZ31B.

5.2.2.3. Freshly Formed Corrosion Filament

A SEM image of a fresh corrosion filament, taken before preparing the thin foil cross-section, is displayed in Figure 5.14. Several cracks were present throughout the corrosion filament. A HAADF-STEM image displaying the entire width of the fresh corrosion filament thin foil cross-section is shown in Figure 5.15(a). The majority of the filament/metal interface was quite diffuse and not easily discernible, and is roughly outlined in the image with a dashed line. The interface location was estimated using a combination of EDS and EELS mapping collected from various sites along the interface. The maximum depth of

the filament was approximately 5 μm. A portion of the filament imaged using BF-TEM is shown in Figure 5.15(b). Several through-thickness cracks in the filament were distinguished by bright areas in this image where electrons could freely pass through the thin foil specimen. However, some portion of the cracks were filled by the protective W coating and as such appeared dark in the BF-TEM image. The broad diffraction rings in the SAD pattern collected from the fresh corrosion filament (Figure 5.15[c]) were matched to cubic MgO (200) and (220), as was the case for the pre-existing surface film, suggesting that the filament also consisted of a nanocrystalline MgO structure.

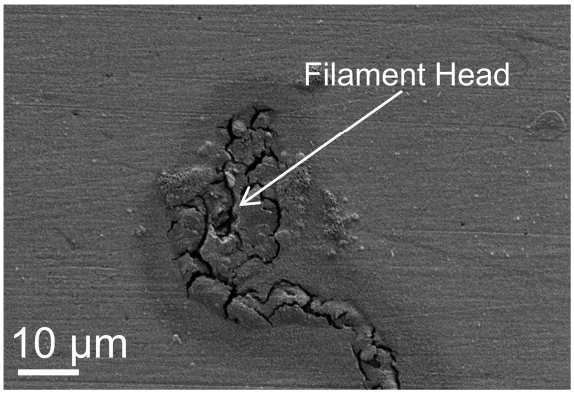

Figure 5.14: Secondary electron SEM image displaying plan view filament morphology on AZ31B immersed in a 0.05 M NaCl solution for 3.5 h.

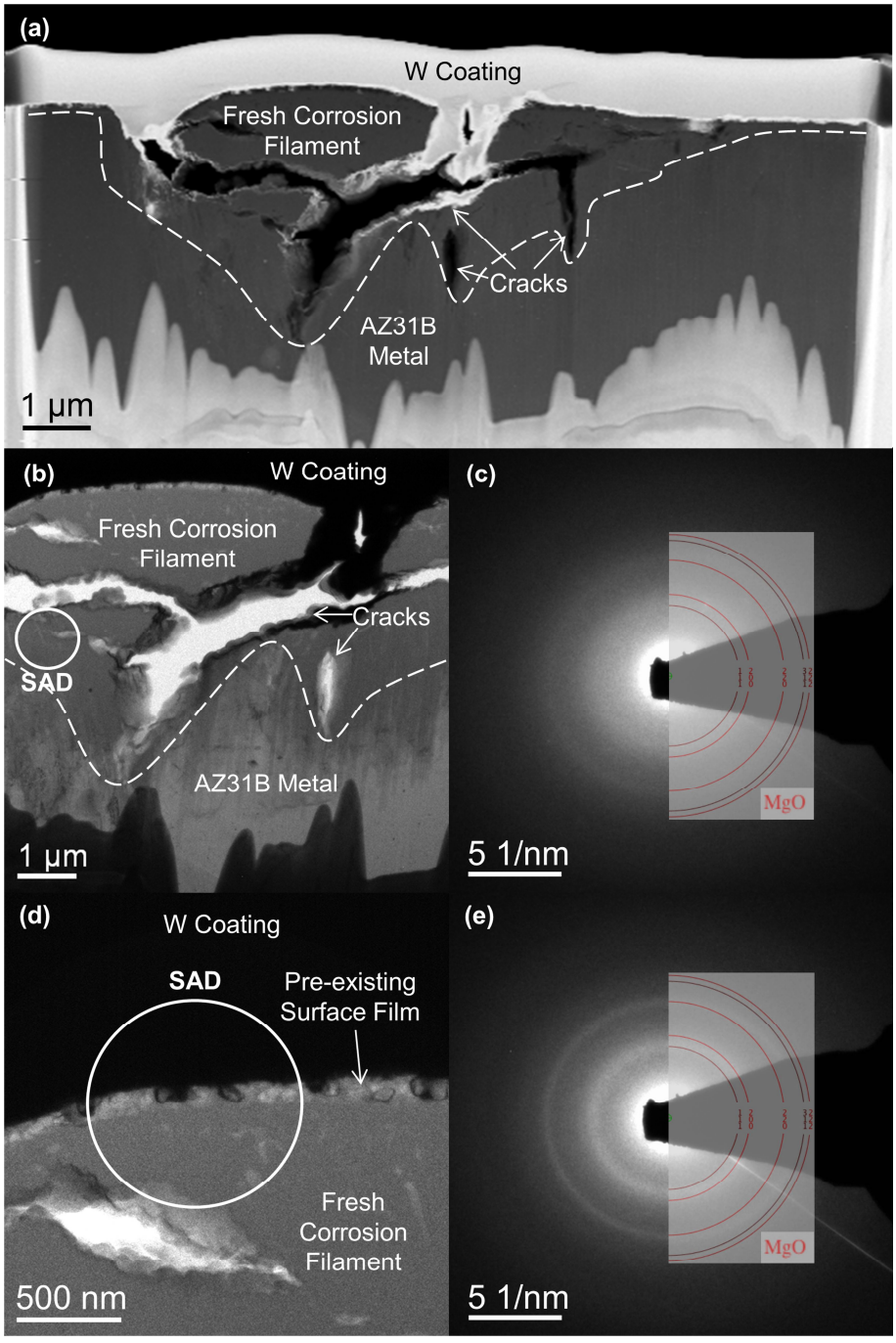

Figure 5.15: (a) HAADF-STEM image of the fresh corrosion filament on AZ31B in cross-section (freshly formed in a 0.05 M NaCl solution); the approximate filament/metal interface is marked with a dashed line, (b) BF-TEM image of the fresh

corrosion filament in cross-section, (c) SAD pattern collected from the marked area in (b); the diffraction rings were indexed to the (200) and (220) planes of cubic MgO, (d) higher magnification BF-TEM image of the fresh corrosion filament and overlying pre-existing surface film, (e) SAD pattern from the area marked in (d); the diffraction rings were indexed to the (111) and (220) planes of cubic MgO.

A separate, thin layer that had the same thickness and appearance as the pre-existing surface film was visible on top of the fresh corrosion filament (Figure 5.15[d]). Due to the small thickness of this layer, the SAD collection area shown in Figure 5.15(d) also contained a significant signal from the underlying filament. However, the resulting SAD pattern (Figure 5.15[e]) contained no diffraction rings or spots corresponding to phases other than cubic MgO, suggesting that this layer had the same MgO crystal structure as the underlying filament and pre-existing surface film. From this, it appears that the corrosion filament undercut and tunneled beneath the pre-existing surface film as it propagated across the metal surface. Figure 5.15(d) also allows for a direct comparison of the morphologies of the pre-existing surface film and fresh corrosion filament. With the exception of the cracks, the darker and relatively uniform contrast of the corrosion filament indicates that it contained denser corrosion products than the relatively porous pre-existing surface film.

A higher magnification HAADF-STEM image revealed the presence of both fine and coarse Al-Mn particles embedded in the fresh corrosion filament (Figure 5.16[a]). EDS spot analyses of both types of particles produced results consistent with those in

Figure 5.9(c). The fine particles were generally more difficult to resolve within the corrosion filament than within the metal and, thus, there may have been additional unresolved particles within the filament. The pre-existing surface film/fresh corrosion filament (Figure 5.16[a]) and fresh corrosion filament/metal (Figure 5.16[b]) interfaces were targeted with EDS point analysis measurements in order to determine if there was any enrichment of Zn at these locations, as was the case for the pre-existing film/metal interface. The spectra revealed no Zn peak at the pre-existing surface film/fresh corrosion filament interface and a Zn peak at the fresh corrosion filament/metal interface (Figure 5.16[c]). Two additional EDS point identification measurements at each of these interfaces yielded the same results. The Zn EDS map across the fresh corrosion filament/metal interface arguably showed a minor enrichment of Zn at the interface, underneath a region apparently depleted in Zn (Figure 5.17). The extracted line profile confirmed that the Zn atomic concentration approximately doubled at the interface relative to the alloy matrix and filament. Similarly to the pre-existing surface film, the EDS maps showed that Al and Cl were present in the fresh corrosion filament.

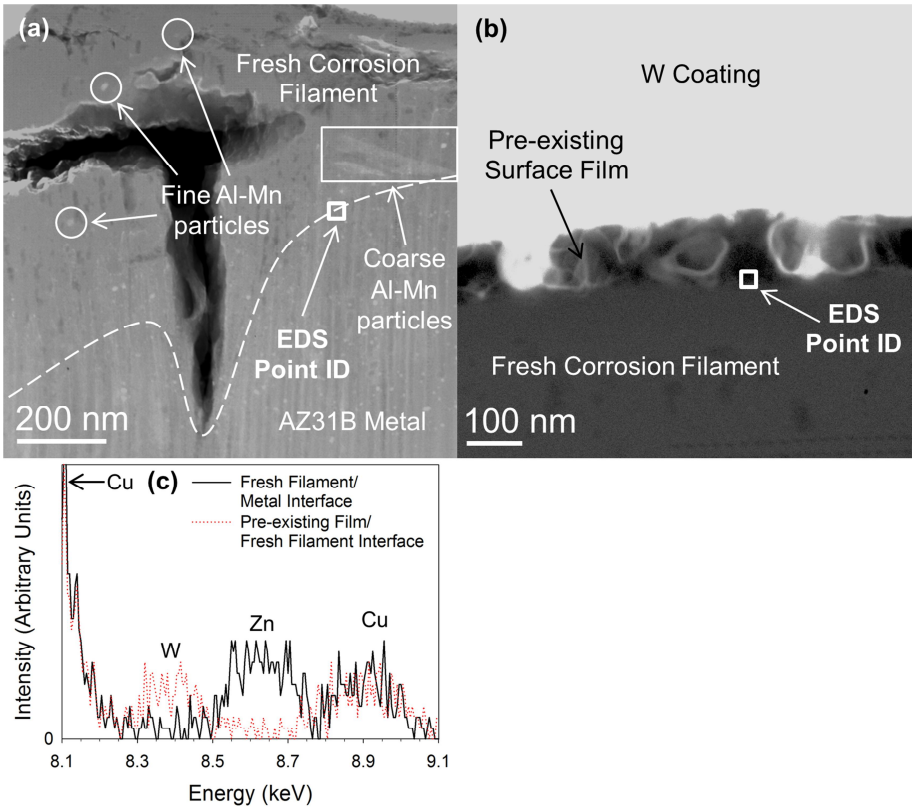

Figure 5.16: (a) Higher magnification HAADF-STEM image of the fresh corrosion filament on AZ31B in cross-section revealing the presence of fine and coarse Al-Mn particles, (b) higher magnification HAADF-STEM image of the fresh corrosion filament and overlying pre-existing surface film, (c) EDS point identification spectra from the locations marked in (a) and (b), magnified to display the Zn peak location.

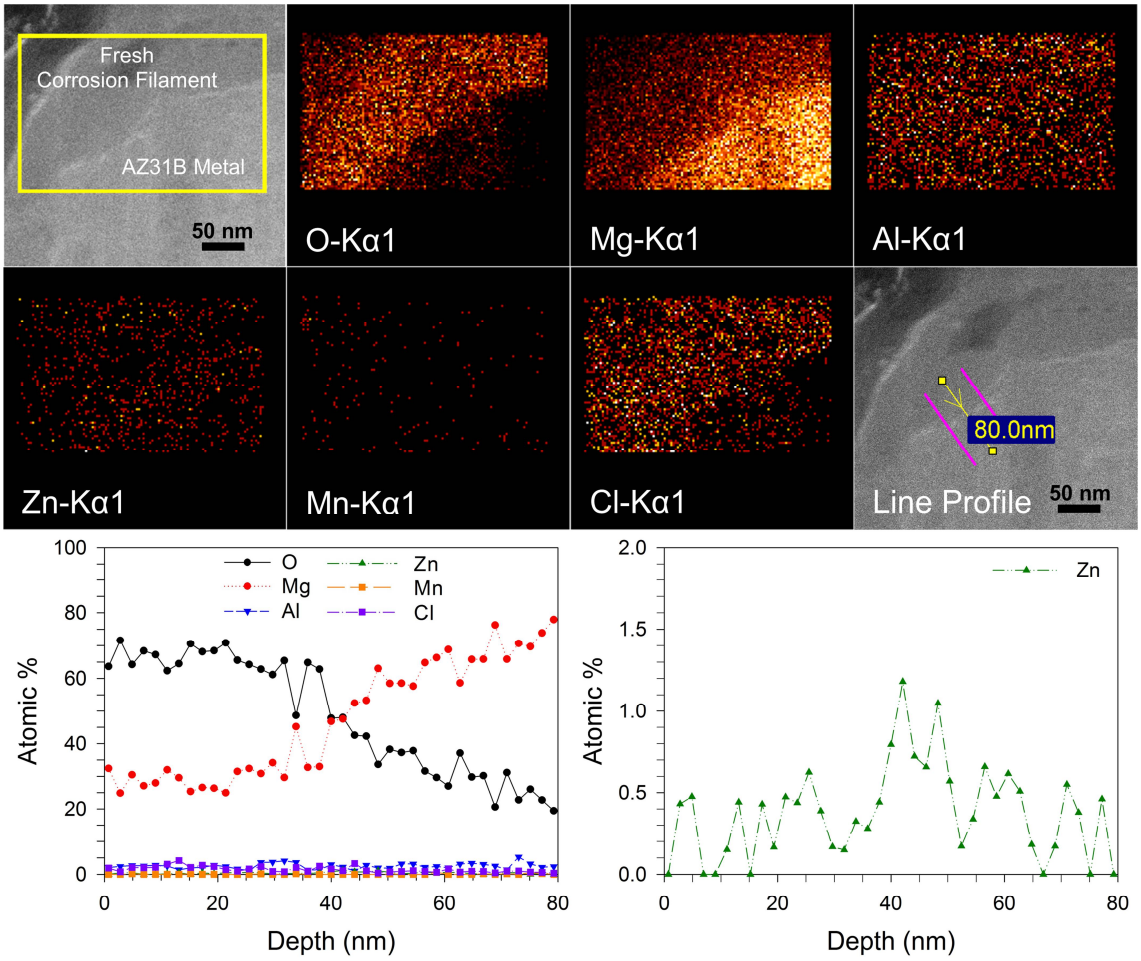

Figure 5.17: EDS maps and line profile displaying O, Mg, Al, Zn, Mn and Cl distribution across the fresh corrosion filament/metal interface on AZ31B. The line profile was summed across ten adjacent lines of pixels located between the marked outer lines.

The AES depth profile through the fresh corrosion filament (Figure 5.18) revealed an O:Mg atomic ratio close to 1:1, indicative of a corrosion product composed primarily of MgO. However, the fact that the atomic concentration of O was slightly higher than Mg suggested that the corrosion products were hydrated to a certain extent. The depth

profile also appeared to show that, opposite to the pre-existing surface film, the top portion of the fresh corrosion filament was depleted in Al. It should be noted here that the thicknesses of all analyzed corrosion filaments prevented complete sputtering through to the underlying metal during depth profiling.

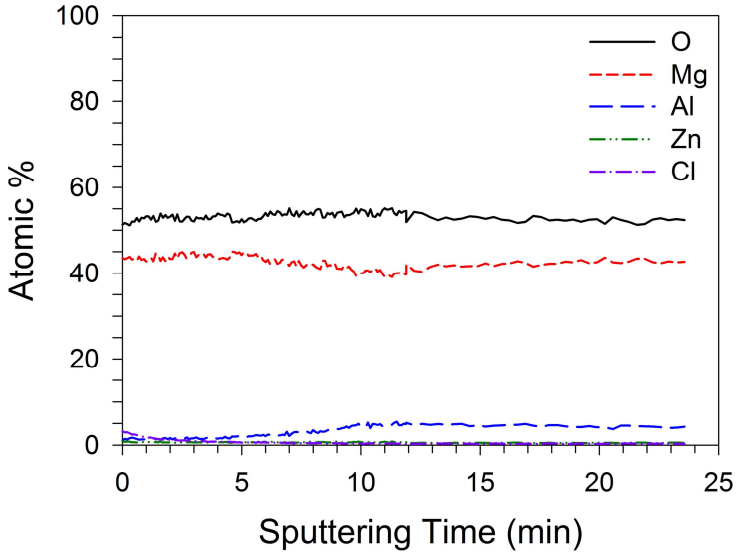

Figure 5.18: AES depth profile through the fresh corrosion filament on AZ31B. Note that the filament thickness (greater than 1 μm) prevented complete sputtering through to the underlying metal.

5.2.2.4. Aged Corrosion Filament

A HAADF-STEM image displaying the entire width of the aged corrosion filament thin foil cross-section is shown in Figure 5.19(a). The aged corrosion filament had a maximum thickness of approximately 3 μm; however, because this filament was not the same one as the fresh corrosion filament, the relative thicknesses of each filament were not regarded

as significant. One through-thickness crack was visible, along with ruptured horizontal bands containing columnar features. A portion of the sample imaged using BF-TEM is shown in Figure 5.19(b). The broad diffraction rings in the SAD pattern collected in Figure 5.19(c) were matched to cubic MgO (111), (200) and (220), suggesting that this aged corrosion filament also consisted of nanocrystalline MgO.

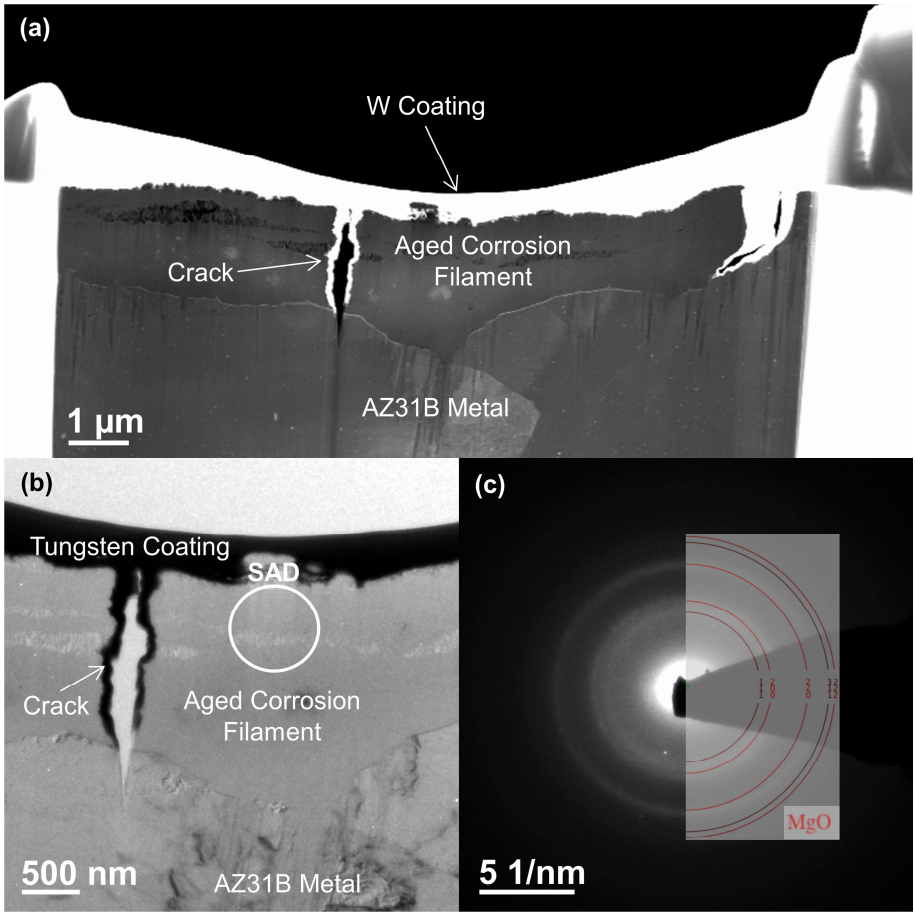

Figure 5.19: (a) HAADF-STEM image of the aged corrosion filament on AZ31B in cross-section (aging time of approximately 11 h in a 0.05 M NaCl solution), (b) BF-TEM image of the aged corrosion filament in cross-section, (c) SAD pattern collected from the marked area in (b); the diffraction rings were indexed to the (111), (200) and (220) planes of cubic MgO.

Higher magnification HAADF-STEM imaging revealed the presence of fine Al-Mn particles within the aged corrosion filament (Figure 5.20[a]): their identities were again confirmed with EDS measurements. At the aged corrosion filament/metal interface

a distinct brighter layer was observed (Figure 5.20[b]). An EDS point identification measurement confirmed that this layer was enriched with Zn (Figure 5.20[c]). The Zn peaks in this spectrum were much stronger relative to the Zn peaks observed in the EDS spectra taken at the pre-existing surface film/metal interface (Figure 5.11[c]) and fresh corrosion filament/metal interface (Figure 5.16[c]) indicating that the concentration of Zn at the filament/metal interface increased as the filament aged. The EDS map and extracted line profile further confirmed the Zn-enrichment at the interface and showed that its atomic concentration increased by a factor of approximately six relative to the alloy matrix and filament (Figure 5.21). Figure 5.21 also displayed, once again, that Al and Cl were present in the aged corrosion filament. In order display the elemental distribution through the majority of the aged filament thickness, an additional line profile is shown in Figure 5.22. Interestingly, a noticeable drop in the Zn concentration could be observed in the filament within approximately 150 μm of the filament/metal interface, suggesting that Zn was rejected from the filament into the metal as the filament aged.

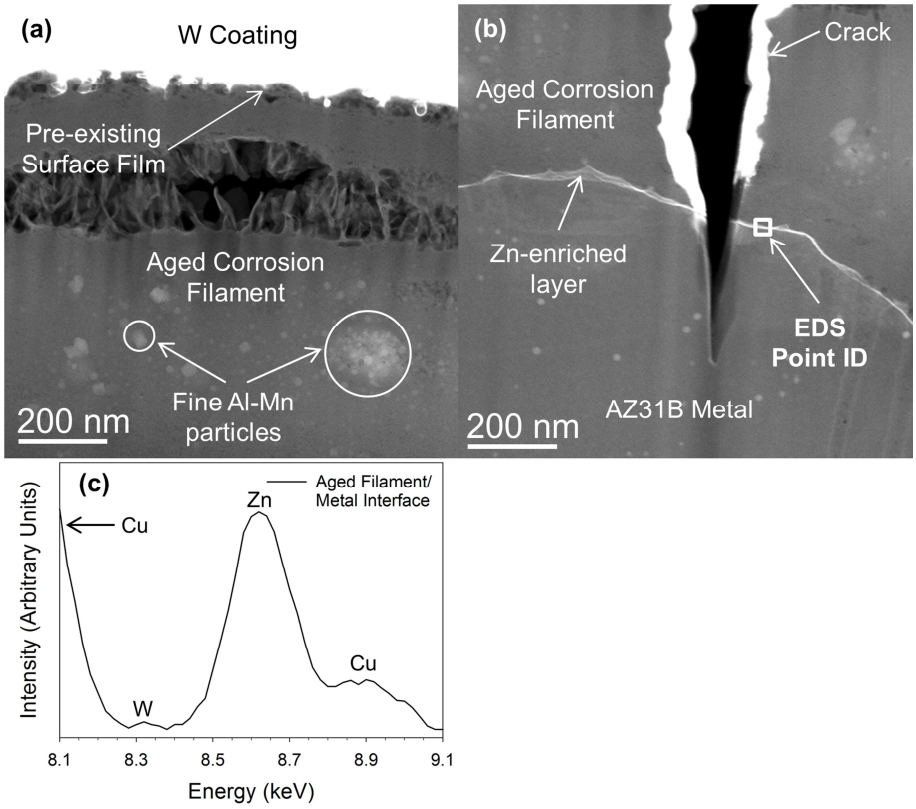

Figure 5.20: (a) Higher magnification HAADF-STEM image of the aged corrosion filament on AZ31B in cross-section revealing the presence of fine Al-Mn particles and the overlying pre-existing surface film, (b) Higher magnification HAADF-STEM image of the aged corrosion filament in cross-section revealing a visible Zn-enriched layer, (c) EDS point identification spectrum from the location marked in (b), magnified to display the Zn peak.

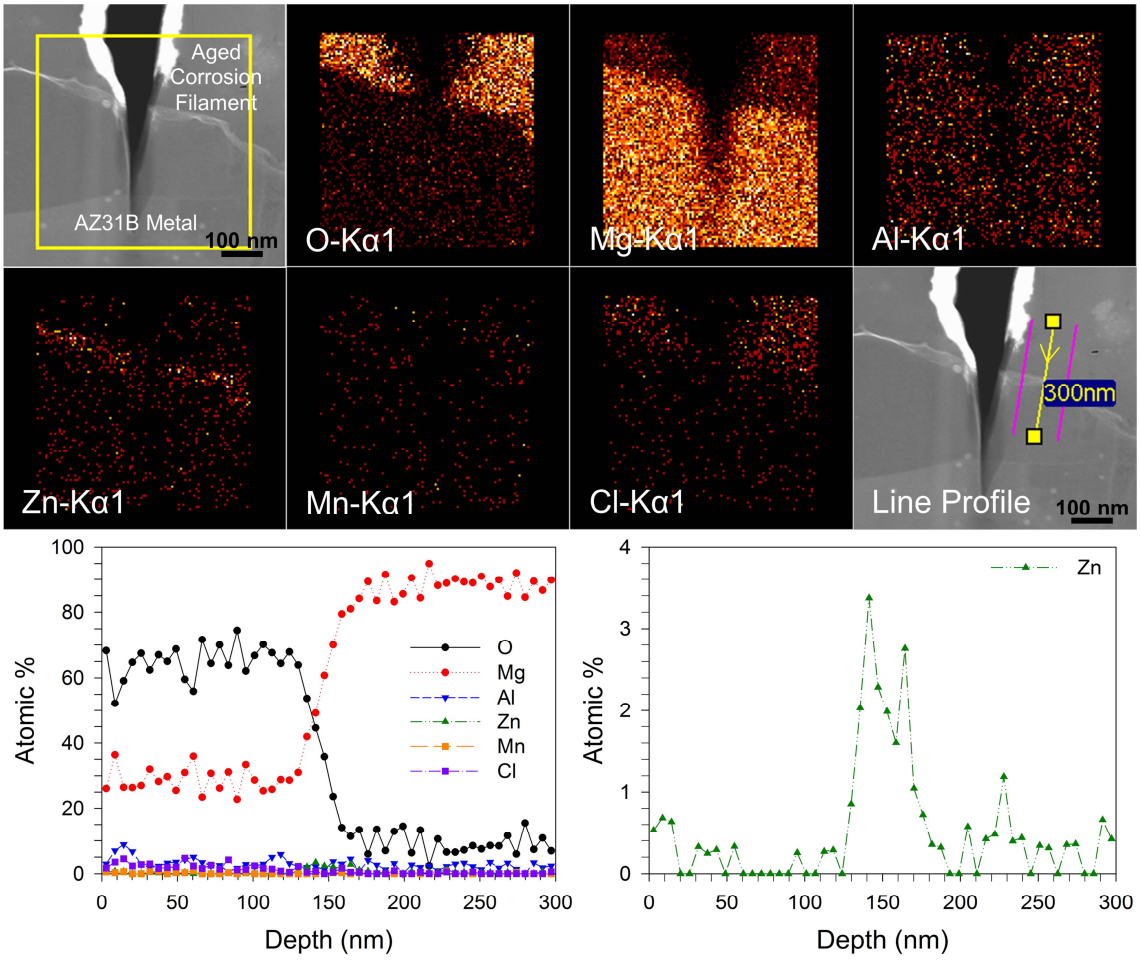

Figure 5.21: EDS maps and line profile displaying O, Mg, Al, Zn, Mn and Cl distribution across the aged corrosion filament/metal interface on AZ31B. The line profile was summed across ten adjacent lines of pixels located between the marked outer lines.

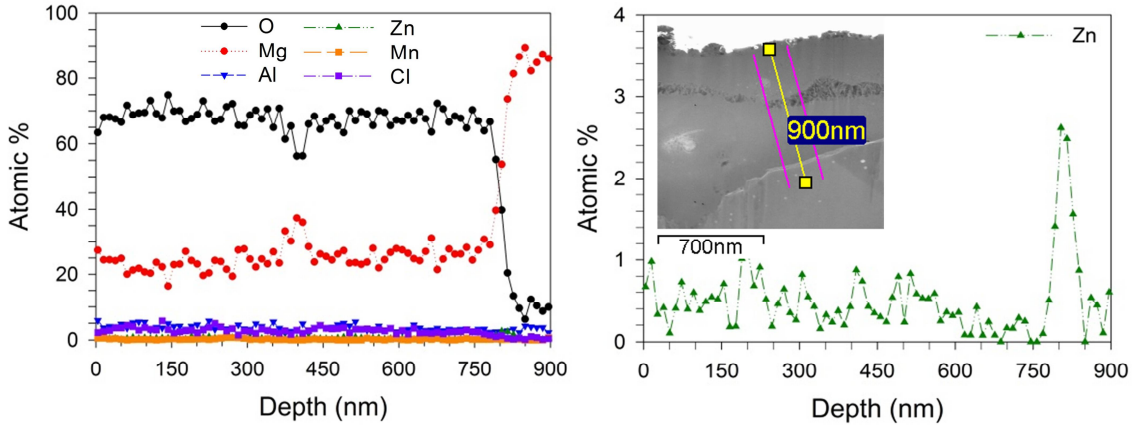

Figure 5.22: Additional line profile displaying O, Mg, Al, Zn, Mn and Cl distribution through the aged corrosion filament and across the filament/metal interface. The line profile was summed across ten adjacent lines of pixels located between the marked outer lines.

In order to better understand the atomic bonding within the observed Zn-enriched layer, a low-loss EELS spectrum image was taken across the aged corrosion filament/metal interface (Figure 5.23 inset). Representative EELS spectra from the Zn-enriched layer (spectrum 1), filament (spectrum 2) and metal (spectrum 3) are shown in Figure 5.23. The spectrum (spectrum 1) taken from the Zn-enriched layer displayed a relatively sharp peak centred at 11.25 eV, confirming that the Zn-enriched layer was metallic. The peak detected from the Zn-enriched layer was slightly shifted and less sharp than that detected from the underlying metal (spectrum 2), the latter of which was centred at 10.60 eV and thus consistent with bulk Mg [78]. The peak expected for bulk Zn is 14 eV and is significantly broader than that of bulk Mg [83], which explains the change in shape and position of the metallic peak from the Zn-enriched layer. However, the position shift

of only 0.65 eV from that of bulk Mg indicated that the Zn-enriched layer was still an Mg-based phase albeit with a significant enrichment of Zn in solid solution.

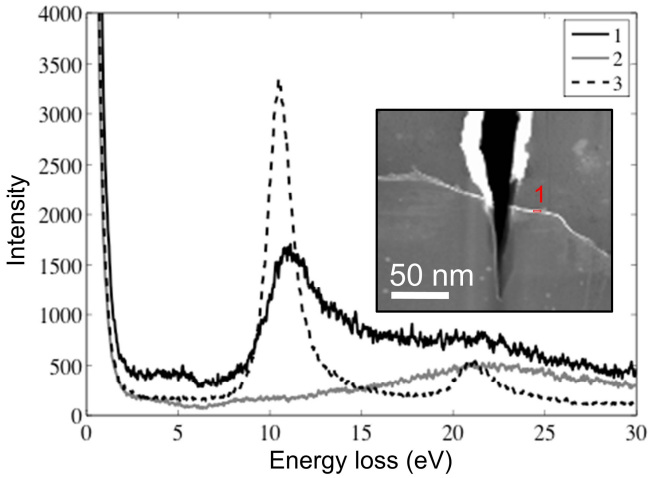

Figure 5.23: Representative low-loss EELS spectra at the aged corrosion filament/metal interface on AZ31B: (1) spectrum corresponding exactly to the Zn-enriched layer (area marked in the inset image, sum of 4 pixels in the spectrum image), (2) spectrum corresponding to one pixel above from the interface (filament), and (3) spectrum corresponding to one pixel below the interface (metal). The peak at location (1) is centered at 11.25 eV with FWHM of 3.75 eV and the Mg plasmon observed in spectrum (3) is centered at 10.60 eV with FWHM of 2.04 eV. Note that the intensity of spectrum 1 was multiplied by a factor of 3 to allow for easier comparison to spectrum 3.

The AES depth profile through the aged corrosion filament (Figure 5.24) revealed an O:Mg atomic ratio appreciably higher than for the fresh corrosion filament, yet still

below a 2:1 ratio. This suggested again that the aged corrosion filament was composed of a mixture of MgO and $Mg(OH)_2$, yet the degree of hydration presumably increased as a result of aging in the solution. Interestingly, the depth profile also appeared to show that the top surface of the fresh corrosion filament was enriched with Al, which was similar to the pre-existing film and opposite to the fresh corrosion filament.

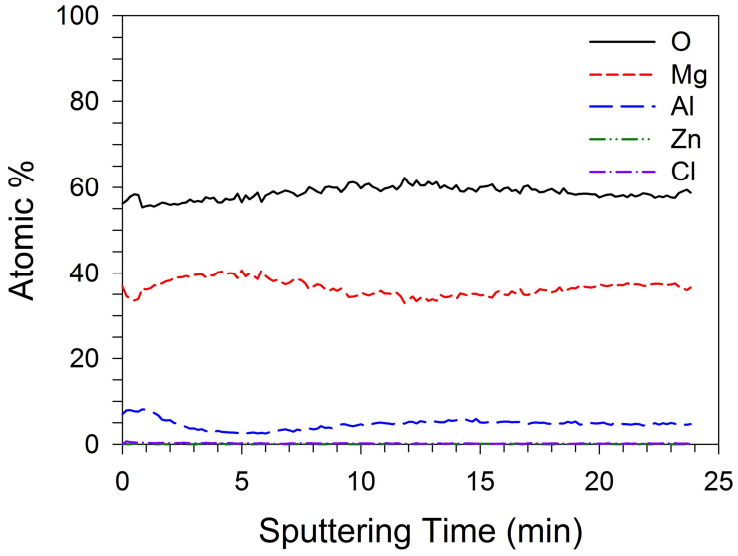

Figure 5.24: AES depth profile through the aged corrosion filament on AZ31B. Note that the filament thickness (greater than 1 µm) prevented complete sputtering through to the underlying metal.

5.3. Localized Corrosion of Mg AM30

5.3.1. Localized Electrochemical Measurements

Selected SVET plots and corresponding scan area images of the AM30 alloy are presented in Figure 5.25 as a function of immersion time. Similarly to the AZ31B alloy, localized corrosion sites evidenced by local anodic peaks and HE were initiated within the first 30 min of immersion (Figure 5.25[a]). Multiple corrosion filaments propagated laterally from these locations towards the bottom-left of the scan area, with anodic peaks and HE observed at the moving fronts of the corrosion filaments and cathodic currents observed in the dark areas left behind (Figure 5.25[b,c]). However, unlike for the AZ31B alloy, cathodic currents were also detected in the lower area of the scan area not yet consumed by the corrosion filaments, albeit with lower magnitudes than the upper areas that were already consumed by the filaments (Figure 5.25[b]). Additionally, the cathodic currents detected above the corrosion filaments appeared to diminish in magnitude with continued immersion time (Figure 5.25[d]). Additional corrosion filaments continued to propagate across the remainder of the alloy surface after 8 h of immersion, but the cathodic currents left behind continued to diminish in magnitude (Figure 5.25[e-h]), which appeared to cause less sustained growth of the filaments when compared to the AZ31B alloy.

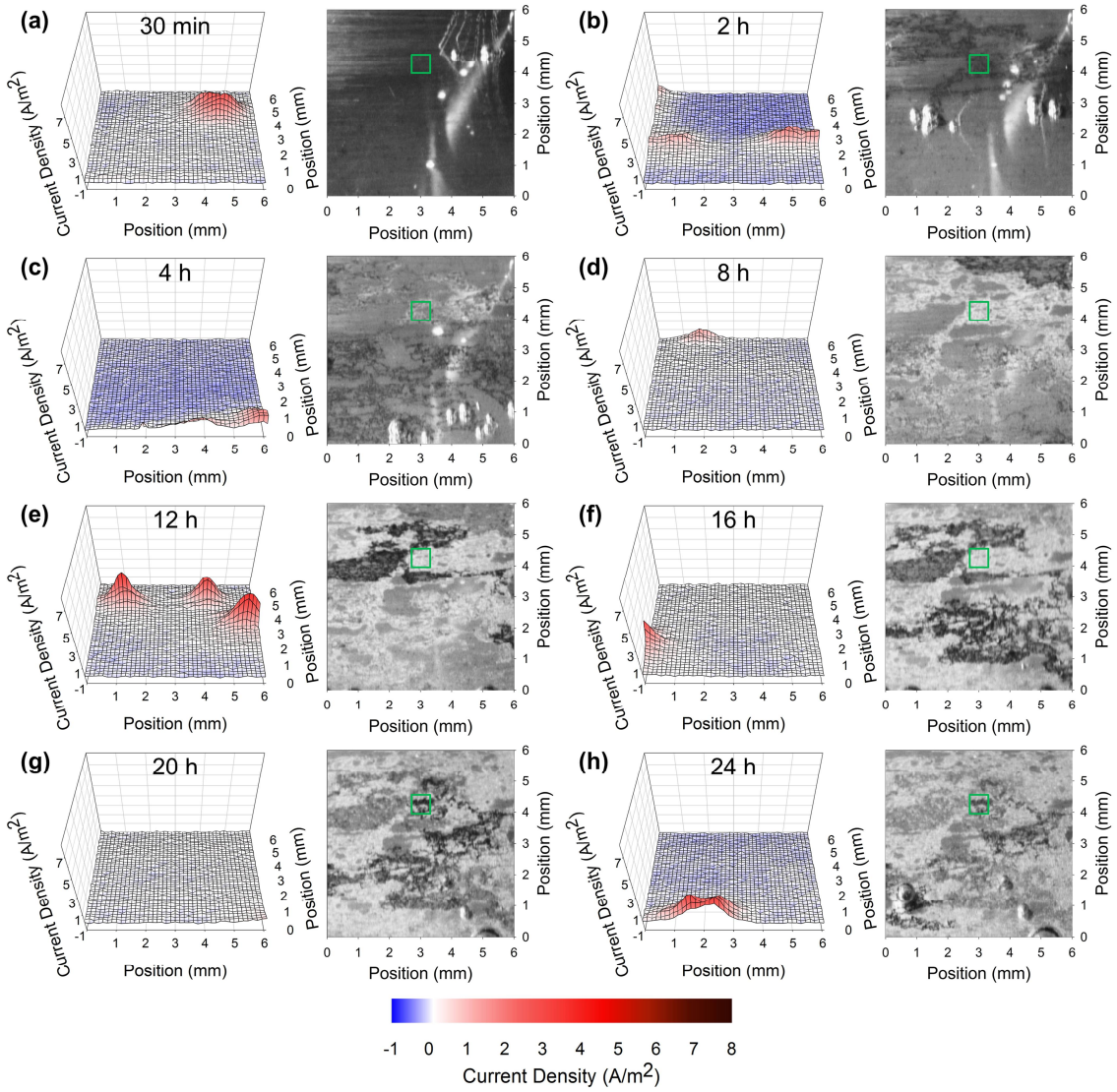

Figure 5.25: Selected SVET plots and scan area images of the AM30 sample at various times after immersion in a 0.05 M NaCl solution. Note that the streak of light sometimes visible on the right half of the scan area images was caused by the reflection of the SVET probe on the alloy surface.

The average magnitudes of the anodic and cathodic current densities within a 0.6 mm × 0.6 mm area outlined by the small squares in Figure 5.25 are shown in Figure 5.26.

The diminishment of cathodic current as a function of immersion time following the passing of a set of corrosion filaments can be clearly observed between the 1 h and 5 h marks in this figure. Additionally, unlike for the AZ31B alloy, repeated passes of corrosion filaments near or within this area did not result in appreciably larger cathodic currents left behind in their wakes.

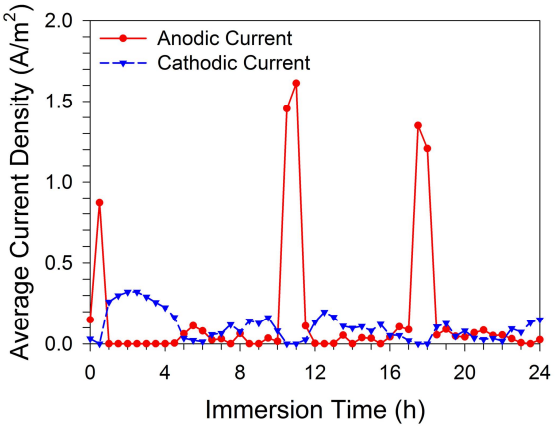

Figure 5.26: Average current density values within the area outlined by the small squares in the scan area images in Figure 5.25.

Plots of integrated current measured across the whole scan area for AM30 versus immersion time are shown in Figure 5.27. For all three of the repeat 24 h immersion tests, it was clear that both the integrated anodic and cathodic currents detected by SVET were relatively stable with respect to immersion time, which was in contrast with the increasing currents observed on the AZ31B alloy (Figure 5.7, Figure 5.8).

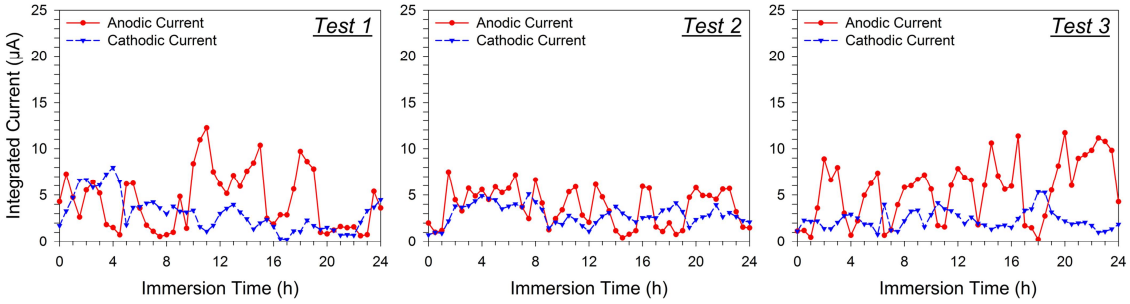

Figure 5.27: Integrated currents across the SVET scan area for AM30 as a function of immersion time in a 0.05 M NaCl solution. Each plot was derived from a separate 24 h immersion test of a freshly polished alloy surface. The first plot was derived from the same test as Figure 5.25 and Figure 5.26.

5.3.2. Microstructure/Corroded Structure Characterization

5.3.2.1. AM30 Microstructure

Unlike the AZ31B alloy, the AM30 microstructure observed from the FIB-prepared thin-foil cross-sections appeared to contain particles having only a single size range, ranging from a few tens to a few hundreds of nanometers (Figure 5.28[a,b]). However, it is noted that coarse particles with sizes on the order of microns were observed from SEM imaging of the AM30 alloy (Figure 4.2[d]). The fine particles in the thin-foil cross-sections had a round shape and some of them were elongated to varying degrees (Figure 5.28[a,b]). The average diameter of the fine particles (assuming perfect spherical shapes) was 27.1 ± 3.0 nm, and their estimated volumetric number density was 800 per μm^3 of metal. EDS spot

analyses of the matrix phase and particles revealed that every analyzed particle was enriched with Al and Mn (Figure 5.28[c]) and a SAD pattern collected from one of the larger particles (Figure 5.28[d]) was indexed to the crystal structure for Al8Mn5. EDS quantification performed on six individual particles after applying the correction adjustment described in Section 5.2.2.1 revealed a mean Al:Mn ratio of 1.33 (Table 5.3), which was within the thermodynamically stable range of Al_8Mn_5 [81]. No evidence was found for the presence of the β-$Mg_{17}Al_{12}$ phase, as was the case for the AZ31B microstructure.

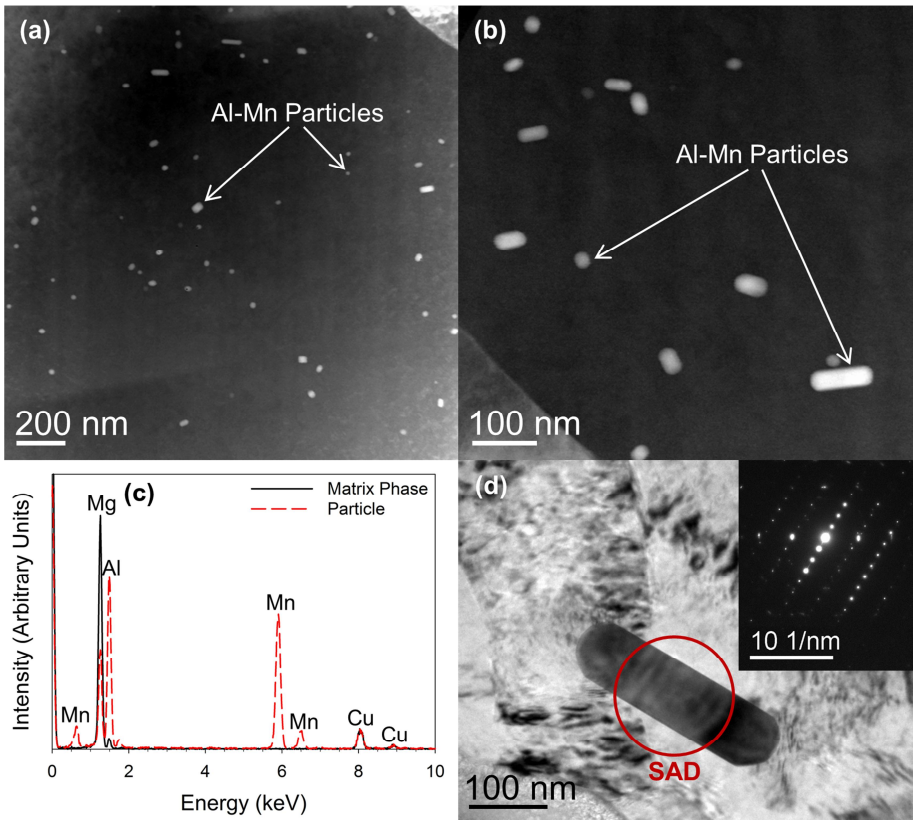

Figure 5.28: (a) (b) HAADF-STEM images of particles found in the AM30 microstructure, (c) typical EDS spectra from the matrix phase and particles, (d) SAD pattern obtained from a relatively large particle.

Table 5.3: Corrected atomic ratios calculated from EDS quantification of Al-Mn particles in the AM30 microstructure.

Particle #	Al:Mn atomic ratio
1	1.25
2	1.31
3	1.48
4	1.46
5	0.79
6	1.69
Mean (95% Confidence)	1.33 (+/- 0.30)

5.3.2.2. Pre-existing Surface Film

A BF-TEM image of the pre-existing surface film formed on the AM30 alloy is shown in Figure 5.29(a). The variations in observed contrast indicated a porous morphology. The thickness of the film varied from approximately 70 to 160 nm, with an average thickness of 106 ± 5 nm. The diffraction rings in the SAD pattern collected from the pre-existing film (Figure 5.29[b]) were indexed to cubic MgO (200) and (220), suggesting that the pre-existing film consisted of nanocrystalline MgO.

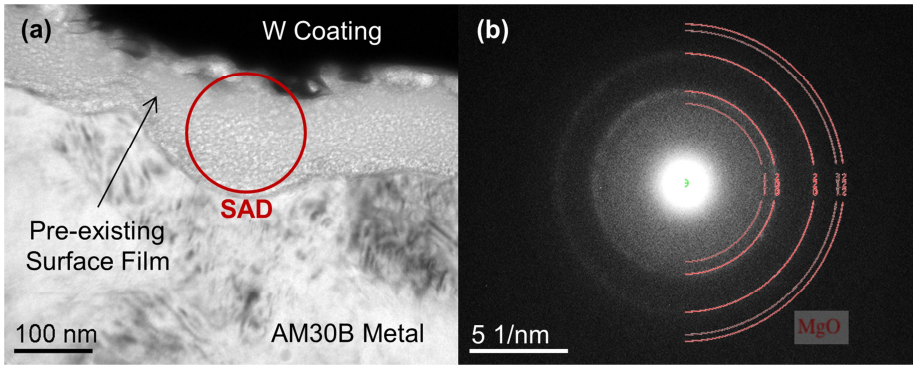

Figure 5.29: (a) BF-TEM image of the pre-existing surface film on AM30 in cross-section after immersion in a 0.05 M NaCl solution for 3.5 h, (b) SAD pattern collected from the area indicated in (a); the diffraction rings were indexed to the (200) and (220) planes of cubic MgO.

The pre-existing surface film imaged with HAADF-STEM revealed the presence of Al-Mn particles embedded within the film (Figure 5.30[a]). EDS point identification revealed a relatively intense Al peak at the pre-existing film/metal interface (Figure 5.30 [b,c]), and EDS mapping demonstrated that the entire analyzed interface was enriched with Al (Figure 5.31). The extracted line profile across the interface indicated that the Al atomic concentration was 2-4 times higher at the interface than in the alloy matrix or film. Therefore, when considering the results of the AZ31B pre-existing film (Figure 5.12), it appears that the absence of Zn in the metal matrix was required to allow for Al to become enriched at the film/metal interface. The presence of Al and Cl in the pre-existing film, as was observed in the pre-existing film on AZ31B, should also be noted.

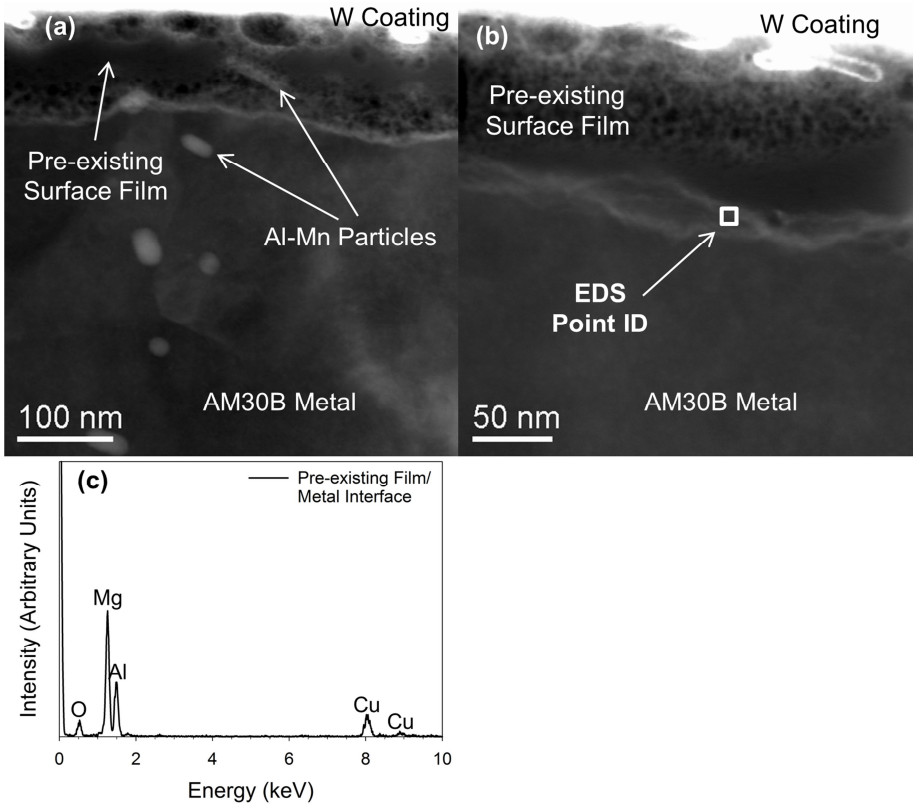

Figure 5.30: (a) HAADF-STEM image of the pre-existing surface film on AM30 in cross-section revealing the presence of fine Al-Mn particles, (b) Higher magnification HAADF-STEM image of the pre-existing surface film, (c) EDS point identification spectrum from the location marked in (b).

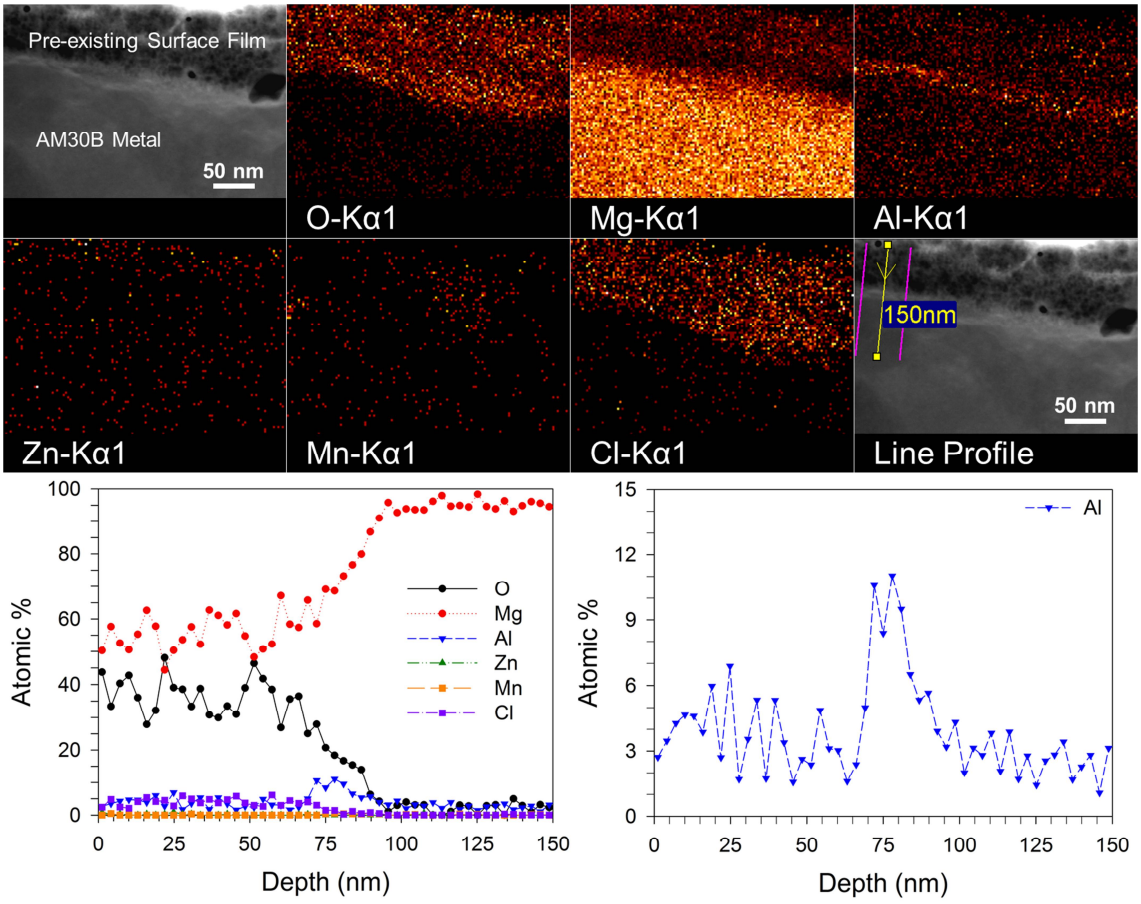

Figure 5.31: EDS maps and line profile displaying O, Mg, Al, Zn, Mn and Cl distribution across the pre-existing film/metal interface on AM30. The line profile was summed across ten adjacent lines of pixels located between the marked outer lines.

The AES depth profile through the pre-existing surface film (Figure 5.32) revealed an O:Mg atomic ratio very close to 2:1. Therefore, similarly to the pre-existing film on the AZ31B alloy, SAD (Figure 5.29[b]) suggested a corrosion product composed of MgO while the AES depth profile instead suggested a $Mg(OH)_2$ corrosion product. The AES depth profile did not definitively reveal the enrichment of Al at the interface that was shown with EDS mapping, which as mentioned for the AZ31B pre-existing film could

perhaps be due to the enriched region being destroyed by the sputtering process. However, the top surface of the film was shown to contain a higher concentration of Al than the rest of the film thickness, as was the case for the pre-existing film on the AZ31B alloy.

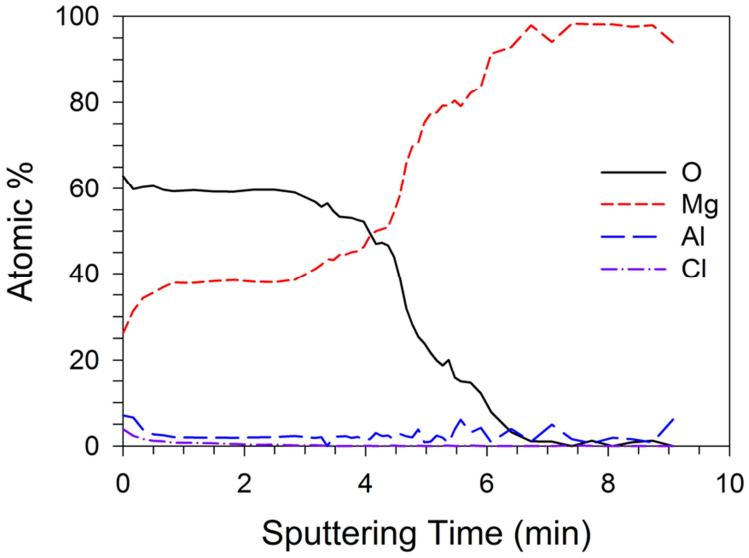

Figure 5.32: AES depth profile through the pre-existing surface film on AM30.

5.3.2.3. Freshly Formed Corrosion Filament

BF-TEM images of the fresh corrosion filament thin foil cross-section are shown in Figure 5.33(a,b). The maximum depth of the filament was approximately 2 µm. The filament contained several cracks and was found to lie underneath the more porous pre-existing surface film, consistent with the filaments formed on AZ31B. Horizontal bands of pores also appeared to be present throughout the filament. The diffraction rings in the SAD pattern collected from the fresh corrosion filament and overlying pre-existing surface film (Figure 5.33[c,d]) were again matched to cubic MgO.

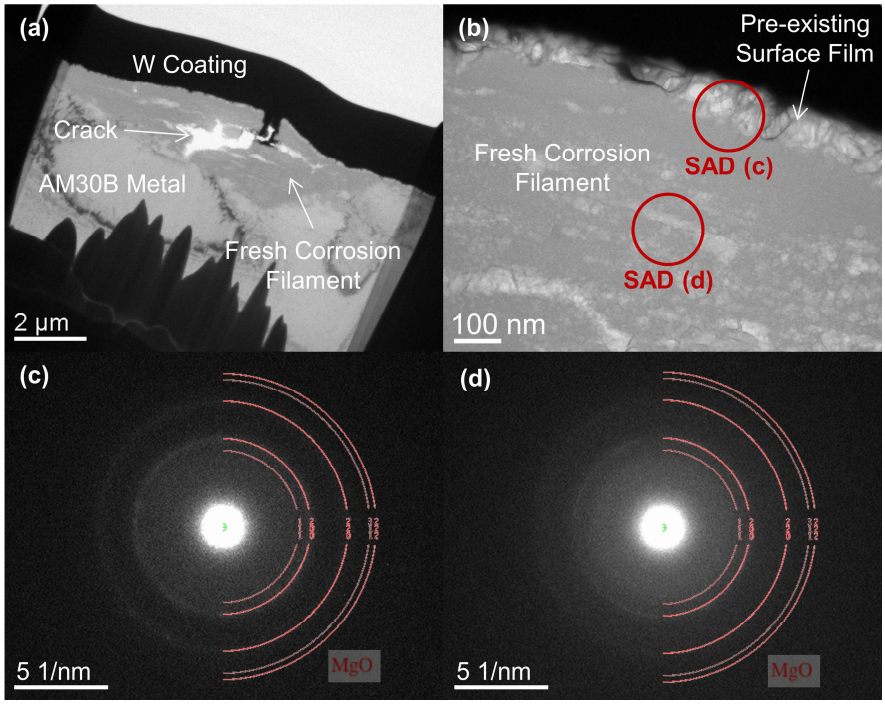

Figure 5.33: (a) BF-TEM image of the fresh corrosion filament on AM30 in cross-section (freshly formed in a 0.05 M NaCl solution), (b) higher magnification BF-TEM image of the fresh corrosion filament and overlying pre-existing surface film, (c) (d) SAD patterns collected from the marked areas in (b); the diffraction rings in (c) and (d) were indexed to the (220)/(200) and (220)/(200)/(111) planes of cubic MgO, respectively.

HAADF-STEM imaging (Figure 5.34[a]) revealed the presence of Al-Mn particles in the fresh corrosion filament, which was again consistent with the filaments on AZ31B. The fresh corrosion filament/metal interface was targeted with EDS point analysis (Figure 5.34[b]) and EDS mapping (Figure 5.35) in an attempt to detect similar Al enrichment as was found at the pre-existing film/metal interface. However, an increased Al signal was

not observed after repeated EDS point and map analyses. The Al EDS map in Figure 5.35 showed the presence of Al and Cl within the fresh corrosion filament, consistent with the filaments analyzed on the AZ31B alloy.

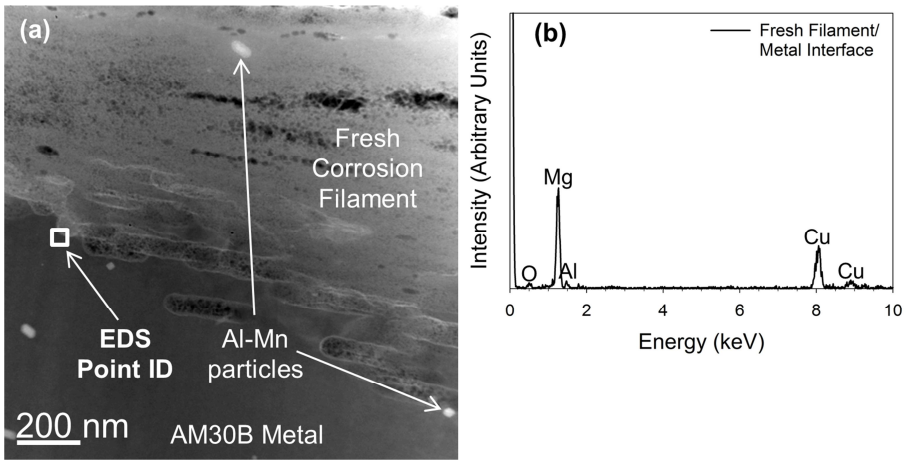

Figure 5.34: (a) Higher magnification HAADF-STEM image of the fresh corrosion filament on AM30 in cross-section revealing the presence of fine Al-Mn particles, (b) EDS point identification spectra from the location marked in (a).

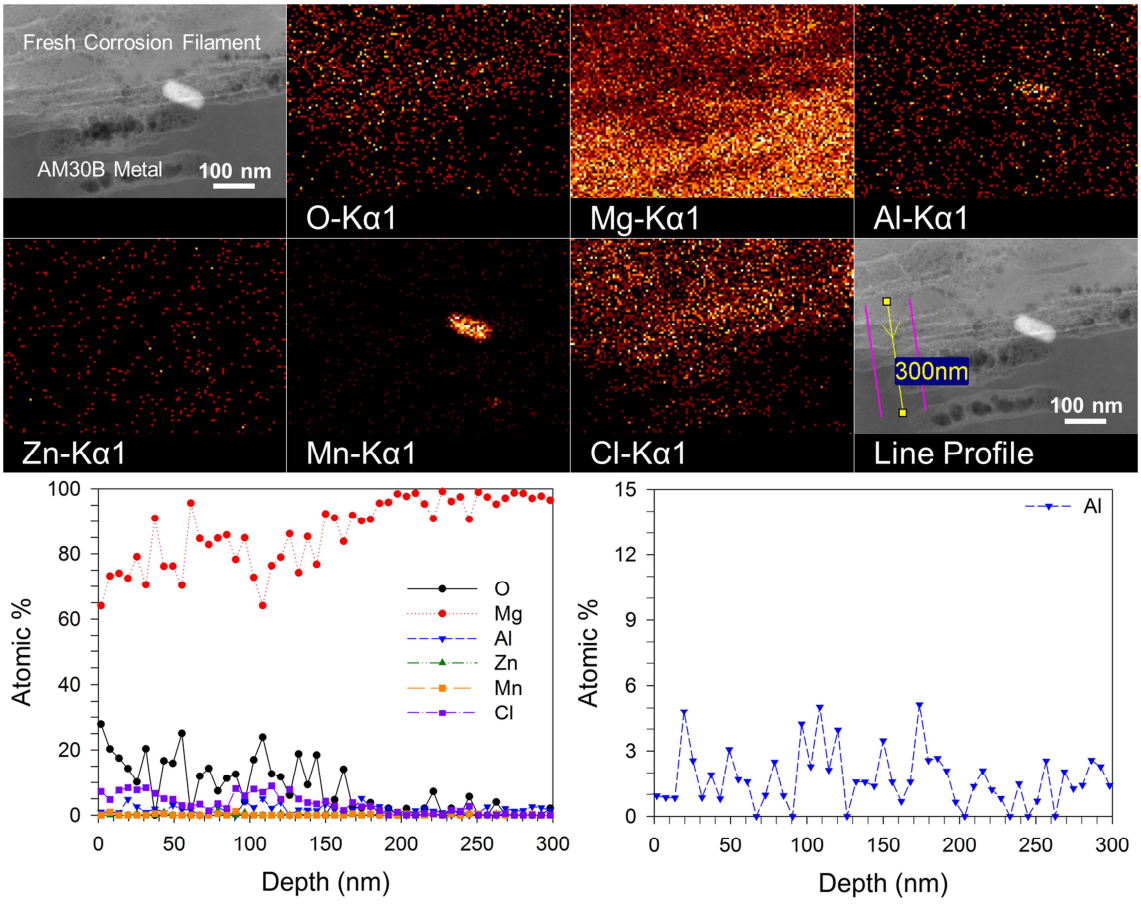

Figure 5.35: EDS maps and line profile displaying O, Mg, Al, Zn, Mn and Cl distribution across the fresh corrosion filament/metal interface on AM30. The line profile was summed across ten adjacent lines of pixels located between the marked outer lines.

The AES depth profile through the fresh corrosion filament (Figure 5.36) was nearly identical to that of the AZ31B fresh corrosion filament (Figure 5.18), where the O:Mg atomic ratio was closer to 1:1 than 2:1 and the top portion of the filament was depleted in Al.

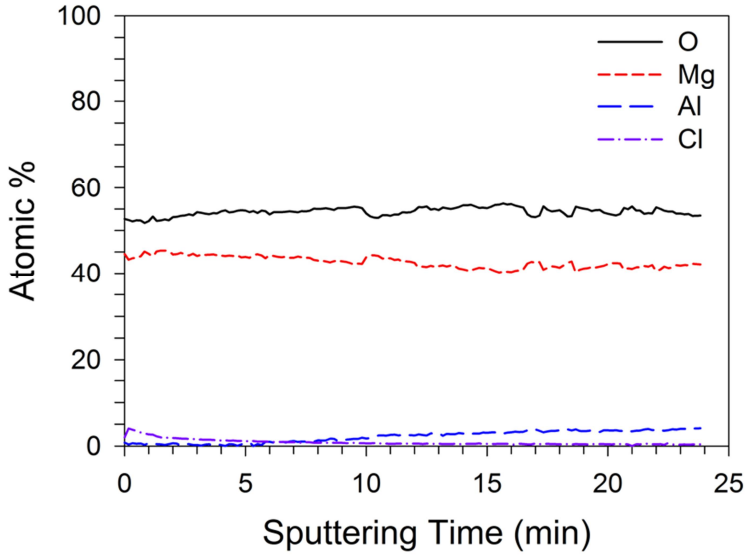

Figure 5.36: AES depth profile through the fresh corrosion filament on AM30. Note that the filament thickness (greater than 1 µm) prevented complete sputtering through to the underlying metal.

5.3.2.4. Aged Corrosion Filament

BF-TEM images of the aged corrosion filament thin foil cross-section are shown in Figure 5.37(a,b). The aged corrosion filament had a maximum thickness of approximately 3 µm, but it should be noted again here that this filament was not the same one as the fresh corrosion filament and thus their relative thicknesses were not regarded as significant. Two through-thickness cracks were visible in the filament along with some ruptured bands containing columnar features; however, the brighter contrast of the overlying pre-existing film indicated that the corrosion filament had a comparatively dense structure, as was the case for each examined filament described previously. The diffraction rings in the SAD patterns collected from the overlying pre-existing surface film (Figure 5.37[c]) and

filament (Figure 5.37[d]) were matched to cubic MgO, suggesting again that they consisted of nanocrystalline MgO. However, diffraction spots characteristic of $Mg(OH)_2$ were also observed in the SAD pattern collected from the ruptured columnar feature located at the overlying pre-existing film.

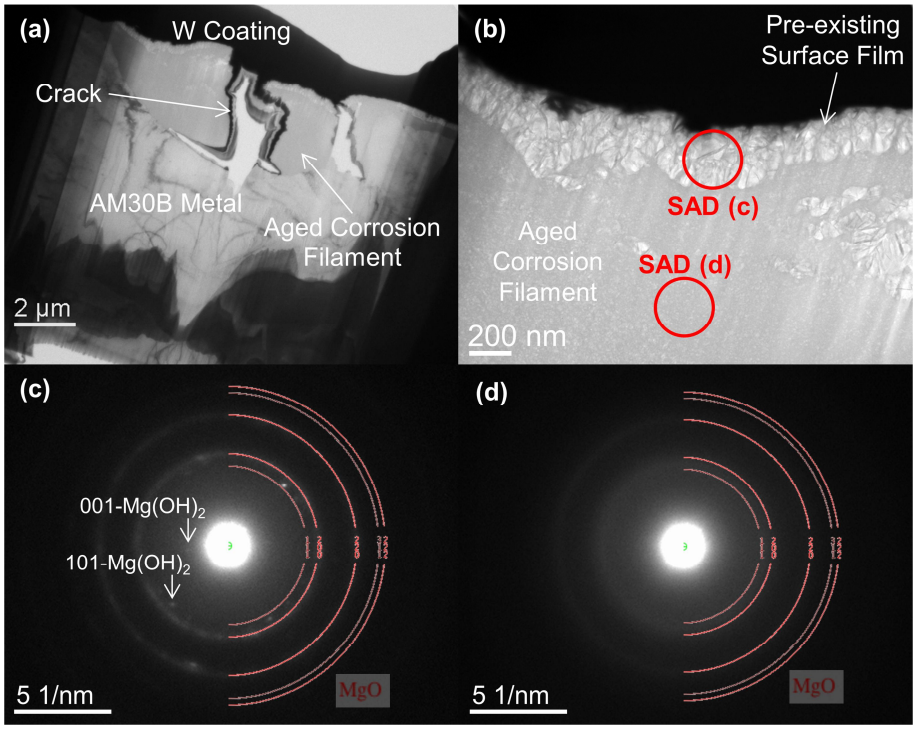

Figure 5.37: (a) BF-TEM image of the aged corrosion filament on AM30 in cross-section (aging time of approximately 11 h in a 0.05 M NaCl solution), (b) higher magnification BF-TEM image of the aged corrosion filament and overlying pre-existing surface film, (c) (d) SAD patterns collected from the marked areas in (b); the diffraction rings in (c) and (d) were indexed to the (220)/(200) and (220)/(200)/(111) planes of cubic MgO, respectively. The diffraction spots in (c) were indexed to the (001) and (101) reflections of $Mg(OH)_2$.

HAADF-STEM imaging revealed the presence of Al-Mn particles within the aged corrosion filament (Figure 5.38[a]). A brighter layer appeared to be present at the aged corrosion filament/metal interface (Figure 5.38[b]) and EDS point identification revealed an Al signal (Figure 5.38[c]) with increased intensity relative to the matrix phase (Figure 5.28). The EDS map and extracted line profile (Figure 5.39) confirmed that Al was enriched to a degree along the interface; however, the quantified concentration here was not as high as what was observed at the pre-existing film/metal interface (Figure 5.31). The concentration of Al at the interface relative to the filament and bulk metal also appeared relatively minor when compared to the Zn enrichment observed at the aged corrosion filament/metal interface on the AZ31B alloy (Figure 5.21). Three additional EDS maps encompassing the aged corrosion filament/metal interface on AM30 demonstrated an equal or lower level of Al enrichment along the interface. Finally, the general presence of Al and Cl in the bulk of the aged corrosion filament displayed by the EDS maps should once again be noted.

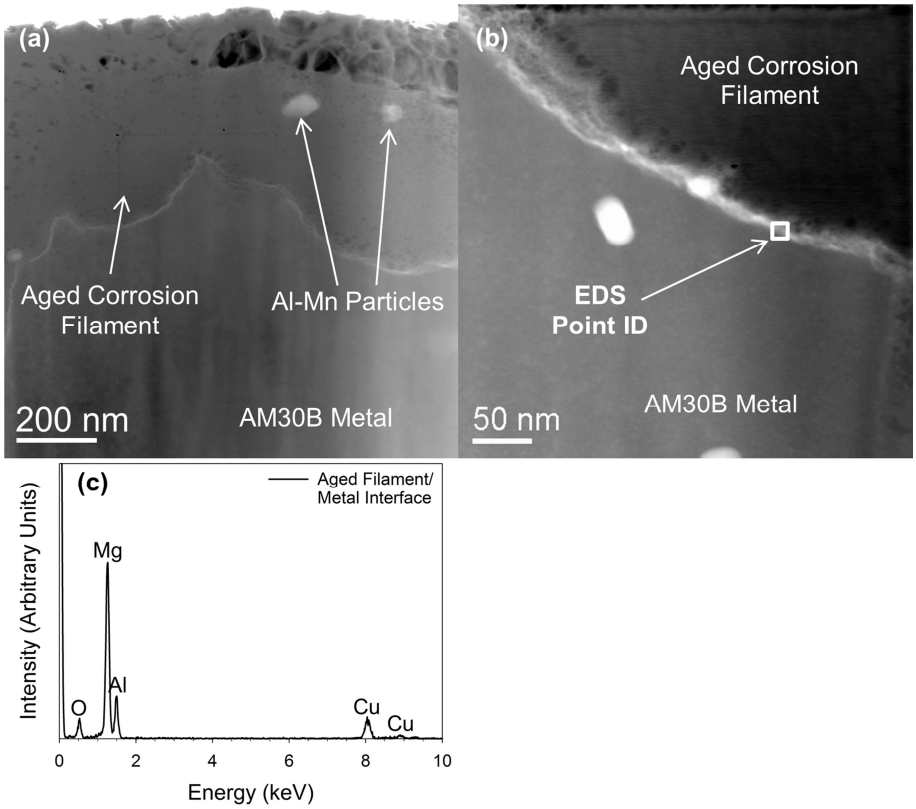

Figure 5.38: (a) HAADF-STEM image of the aged corrosion filament on AM30 in cross-section revealing the presence of Al-Mn particles (b) Higher magnification HAADF-STEM image of the aged corrosion filament revealing a brighter layer at the filament/metal interface, (c) EDS point identification spectrum from the location marked in (b).

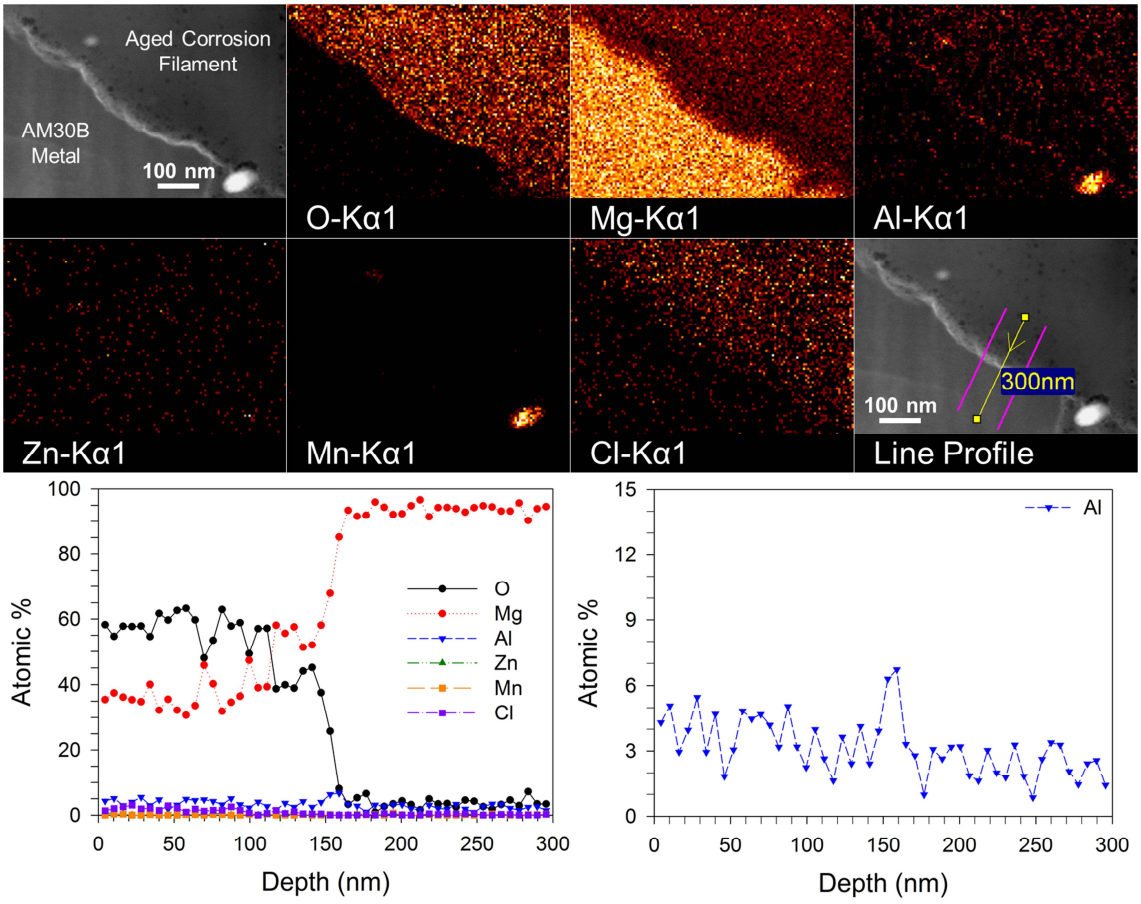

Figure 5.39: EDS maps and line profile displaying O, Mg, Al, Zn, Mn and Cl distribution across the aged corrosion filament/metal interface on AM30. The line profile was summed across ten adjacent lines of pixels located between the marked outer lines.

The AES depth profile through the aged corrosion filament (Figure 5.40) proved again to be similar to that of the AZ31B alloy (Figure 5.24), where the O:Mg atomic ratio was appreciably higher than for the fresh corrosion filament, and therefore suggested a higher degree of hydration. The top surface of the aged corrosion filament appeared to be

enriched with Al, which was also consistent with the aged corrosion filament on the AZ31B alloy.

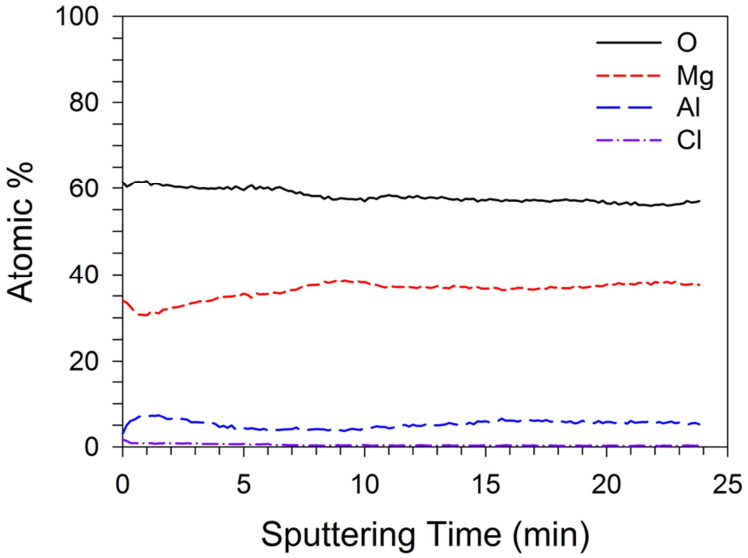

Figure 5.40: AES depth profile through the aged corrosion filament on AM30. Note that the filament thickness (greater than 1 µm) prevented complete sputtering through to the underlying metal.

Chapter 6: Discussion

The first three sections in this chapter will discuss the electrochemical behaviour (Section 6.1), corrosion product formation and aging (Section 6.2) and the preferential dissolution and elemental segregation (Section 6.3) aspects of the results reported in Chapter 5. Each of these sections contains a detailed comparison between the AZ31B and AM30 alloys as it pertains to the respective topic along with further discussion detailing the implications of the findings. The key findings are summarized in Section 6.4 and will be discussed in the context of an overall mechanism of filiform-like corrosion on AZ31B and AM30 alloys in Section 6.5.

6.1. Electrochemical Behaviour

The OCP evolution as a function of immersion time was not significantly different between AZ31B and AM30 (except for the higher OCP of the AM30 alloy) (Figure 5.1). Both alloys displayed a relatively rapid rise in their respective OCP within the first 100 s of immersion followed by a more gradual rise thereafter, which was not unlike the OCP transient behaviour observed by Taheri et al. [31] for pure Mg immersed in pure H_2O (Figure 2.4). However, the OCP of the AZ31B and AM30 alloys suddenly dropped within approximately 2-5 h of immersion time, coinciding with the initiation of localized corrosion filaments on the exposed surfaces (Figure 5.1, Figure 5.2). Presumably, the OCP de-

crease was caused by the high anodic current density associated with localized corrosion and the fluctuations in the OCP following the breakdown event were reflective of the unstable nature of localized corrosion. Breakdown events were similarly detected in the OCP transients recorded by Williams and co-workers [12,16] for pure Mg in 0.86 M NaCl (Figure 2.5) and also for AZ31B in NaCl solutions ranging in concentration from 0.034 M to 0.86 M. A more gradual OCP drop was observed by Taheri et al. [31] for pure Mg in pure H_2O after approximately 5 h (Figure 2.4), and although this was not correlated with the initiation of localized corrosion, it was postulated that the OCP maximum corresponded to a breakdown of the pre-existing MgO-rich surface film and subsequent formation of a thick $Mg(OH)_2$-rich outer layer.

The average OCP, i_{corr} and i_c values of the alloys following immersion at the OCC for 1 h and 24 h are plotted in Figure 6.1 (data from Table 5.1). Prior to breakdown (after 1 h), the OCP of AM30 was significantly higher than that of AZ31B by approximately 20 mV. However, the OCP of AZ31B rose significantly by approximately 30 mV following 24 h at the OCC, whereas the average OCP of AM30 did not significantly change after 24 h. The OCP increase of the AZ31B alloy was caused by an increase of cathodic kinetics, since i_c at -1.6 V_{SCE} was significantly higher following 24 h at the OCC. By contrast, i_c at -1.6 V_{SCE} was not significantly different for AM30 between 1 h and 24 h at the OCC. Similarly, only the i_{corr} of AZ31B increased significantly after 24 h, which was consistent with the observation of higher surface coverage of the corrosion filaments on AZ31B following 24 h at the OCC (Figure 5.2).

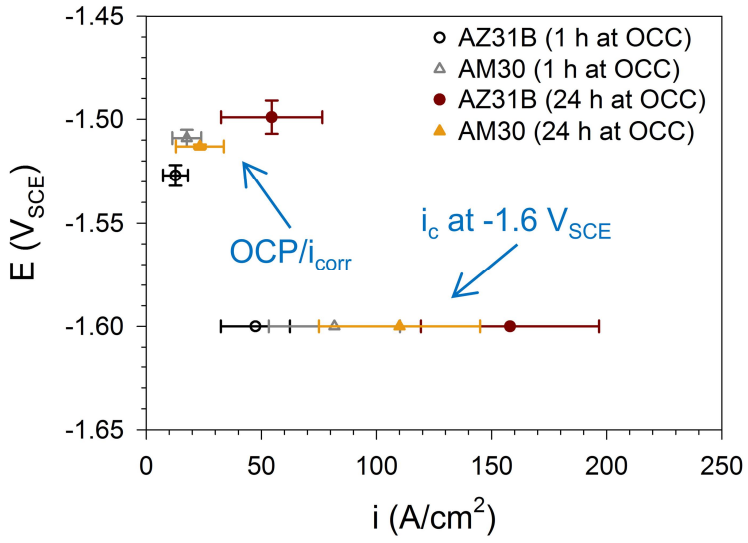

Figure 6.1: Average values and 95% confidence intervals for the OCP, i_{corr} and i_c (at -1.6 V_{SCE}) for AZ31B and AM30 (data from Table 5.1).

The SVET results in this work revealed that the surfaces consumed by corrosion filaments acted as localized cathodes on both AZ31B (Figure 5.5) and AM30 (Figure 5.25), which was in agreement with the previous SVET investigations of Williams and co-workers. [12,15,16]. However, it was also shown in this work that the cathodic current density above a defined region of filaments was relatively stable with respect to immersion time for AZ31B (Figure 5.6), whereas it diminished with immersion time for AM30 (Figure 5.26). The consequences of this observation are summarized in Figure 6.2, which displays the average SVET-determined integrated currents for each alloy as a function of immersion time. It can be seen that the increasing surface coverage of the cathodic corrosion filaments for AZ31B resulted in progressively larger cathodic currents, and thus, progressively larger anodic currents with respect to immersion time. By contrast, although

the surface coverage of the cathodic corrosion filaments on AM30 also progressively increased, the proportionately diminishing cathodic current density from a defined region of filaments (Figure 5.26) resulted in relatively constant integrated cathodic and anodic currents with respect to immersion time. This behaviour correlated well with the OCP, i_{corr} and i_c data for each alloy after 1 h and 24 h at the OCC (Figure 6.1). This is an important observation because it demonstrates that relatively straightforward polarization tests can reveal the electrochemical kinetics of localized corrosion features as long as they cover a significant fraction of the tested surface.

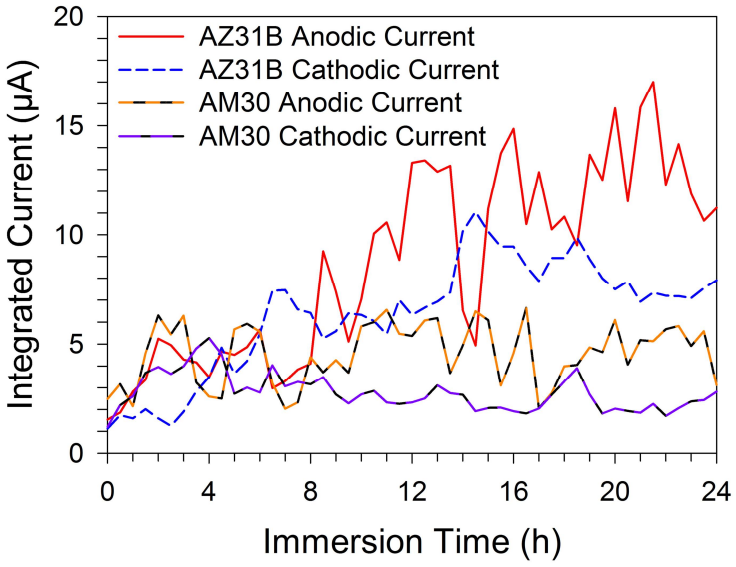

Figure 6.2: Average values of SVET-determined integrated currents from AZ31B (Figure 5.7) and AM30 (Figure 5.27) as a function of immersion time.

Interestingly, the AZ31B SVET investigation by Williams et al. [16] yielded results that were more similar to the AM30 results presented in this work, since they also

noted that the average cathodic current density for a defined region of corrosion filaments diminished with respect to immersion time in a 0.86 M NaCl solution. However, it should be noted that the AZ31B material used by Williams et al. was in the as-cast condition, whereas the AZ31B material used in this work was wrought and subjected to a H24 temper. AZ31B in the as-cast condition often has a dendritic microstructure with significant segregation of Al [84,85] as opposed to the homogeneous microstructure of the AZ31B alloy used in this work (Figure 4.1). The dendritic appearance of the corrosion filaments observed by Williams et al. (Figure 2.11[a]) suggested that the filaments propagated along dendritic pathways of the microstructure. By contrast, the corrosion filaments in this work likely propagated along grain boundaries, twin boundaries and surface damage arising from the sample preparation procedure (e.g. scratch marks), in a similar manner as that reported for pure Mg [51]. It is also worth noting that the electrochemical results in this work appear to contradict those of Zhao et al. [73], who determined from polarization testing and hydrogen collection experiments that the corrosion rate of AM30 was considerably higher than that of AZ31B in a 0.53 M NaCl solution in which localized corrosion was initiated. However, it is not clear how the nanoscale microstructures (which are suspected to significantly affect filiform-like corrosion susceptibility) of the alloys used in each work compared to each other.

The fact that the average grain size of the AZ31B alloy used in this work was approximately ten times larger than the AM30 alloy should also be mentioned as a possible factor in their respective corrosion behaviours. While it has been proposed that reducing the grain size of Mg increases its corrosion resistance by increasing the stability of the

semi-protective surface film [46,54,86], this does not speak to its post-breakdown resistance to filiform or filiform-like corrosion. Song et al. [87] have reported that decreasing the grain size on pure Mg led to a decreased resistance to localized corrosion, while Aung and Zhou [48] reported the opposite trend for AZ31B. With the assumption that filiform and filiform-like corrosion propagates primarily along grain boundaries, it could be argued that a higher density of grain boundaries would provide a higher number of anodic pathways for filiform-like propagation. However, given that disc-like or filiform-like corrosion on Mg and AZ31B is a cathodically-driven process [12,16], a higher density of grain boundaries by itself would not be expected to lead to enhanced anodic dissolution. This hypothesis is supported by the result presented in Figure 5.8, which demonstrated that the SVET-detected integrated anodic and cathodic current magnitudes on a coarse-grained AZ31B sample were insignificantly different from the fine-grained AZ31B sample (Figure 5.7) and appreciably higher than the (similarly coarse-grained) AM30 alloy (Figure 5.27). Kish et al. [88] similarly reported that the grain size of friction stir welded AZ31B joints did not affect the anodic and cathodic kinetics of filiform-like corrosion.

Taking the above points into consideration, it would appear that the greater local cathodic kinetics (and thus localized corrosion susceptibility) on AZ31B in comparison to AM30 cannot be attributed solely to differences in their respective average grain sizes. It is, therefore, more likely that the electrochemical dissimilarities between the alloys can be explained either by differences in their respective alloying contents or by differences in the distribution of cathodic intermetallic Al-Mn particles in each alloy.

6.2. Corrosion Product Formation and Aging

In this work, SAD (via TEM) and quantification of the O:(Mg+Al+Zn) or O:(Mg+Al) ratios (via AES) were both used to determine whether the corrosion products within the pre-existing surface films and corrosion filaments comprised either MgO or $Mg(OH)_2$. Every SAD pattern collected from the corrosion products consisted of diffraction rings indicative of nanocrystalline MgO, while only one of the SAD patterns collected from the top surface of the aged corrosion filament on AM30 contained diffraction spots indicative of $Mg(OH)_2$ in addition to MgO diffraction rings (Figure 5.37). However, the O:(Mg+Al+Zn) or O:(Mg+Al) atomic ratios (plotted for comparison in Figure 6.3) suggested that varying mixtures of MgO and $Mg(OH)_2$ were present in each corrosion product.

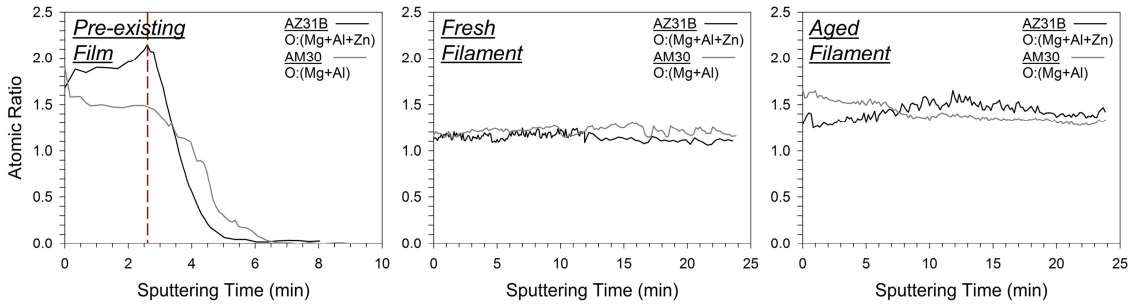

Figure 6.3: O:(Mg+Al+Zn) and O:(Mg+Al) atomic ratio depth profiles through the pre-existing surface film, fresh corrosion filament and aged corrosion filament on AZ31B and AM30. Atomic ratios were calculated from the AES quantification results presented in Figure 5.13, Figure 5.18, Figure 5.24, Figure 5.32, Figure 5.36 and Figure 5.40. The vertical dashed line represents the approximate location of the beginning of the transition from the pre-existing surface film to the metal for both alloys.

The single-layer MgO structure observed from the TEM analysis of the pre-existing surface film on each alloy appears to be consistent with the surface films examined by Unocic et al. [32] on pure Mg and AZ31B following 4 h of immersion in pure H_2O, which were also identified as being primarily composed of MgO using XPS depth profiling and SAD via cross-sectional TEM. However, the AES-determined O:(Mg+Al+Zn) or O:(Mg+Al) atomic ratios for the pre-existing surface films in this work were at least 1.5 (Figure 6.3), which suggested these structures contained a significant proportion of hydrated corrosion products. This apparent discrepancy could perhaps be explained by the presence of scattered hydroxide products throughout the nano-sized pores in the film which would lack the sufficient long-range ordering necessary to pro-

duce a SAD pattern characteristic of $Mg(OH)_2$ (i.e. an amorphous or nearly-amorphous hydroxide).

The O:(Mg+Al+Zn) and O:(Mg+Al) atomic ratios calculated from the fresh corrosion filament for each alloy ranged from 1.1 to 1.3 (Figure 6.3), suggesting that these structures were primarily composed of MgO in accordance with the TEM-determined MgO SAD patterns. This result is consistent with the results of Schmutz et al. [51], who determined that the corrosion filaments formed on pure Mg in 0.01 M NaCl + 10^{-4} M $Na_2Cr_2O_7$ were composed primarily of MgO. Interestingly, this would appear to contradict the conventional reaction process typically used to describe Mg corrosion, which involves the direct reaction of dissolved Mg^{2+} and OH^- produced from the HE reaction to form $Mg(OH)_2$ (Equation 2.3). The physical separation of the anodic and cathodic processes involved in filiform-like corrosion could help to explain the formation of MgO rather than $Mg(OH)_2$. The high local quantity of Mg^{2+} ions dissolved at the filament head (evidenced by the intense SVET-detected anodic current peaks) would likely outnumber the local quantity of OH^- ions, since the production of the latter would be dispersed along the regions already consumed by corrosion filaments. As noted in Chapter 2, the production of MgO rather than $Mg(OH)_2$ is significant in regards to the resulting corrosion filament morphology because the lattice parameter of MgO is smaller than that of metallic Mg. This lattice mismatch causes tensile stresses to develop within the corrosion filaments and can ultimately lead to shrinkage cracks, which were indeed observed in both the work of Schmutz et al. [51] and the present work (Figure 5.14, Figure 5.15, Figure 5.19, Figure 5.33 and Figure 5.37).

The aged corrosion filaments on both alloys were noted to contain a number of ruptured features with a columnar appearance (Figure 5.19 and Figure 5.37). These regions appeared to have a similar morphology to the columnar structures observed by Taheri et al. [31,58] which were identified as crystalline $Mg(OH)_2$ in these works. The SAD pattern collected from one of these regions (Figure 5.37) confirmed the presence of crystalline $Mg(OH)_2$, although diffraction rings indicative of nanocrystalline MgO were also observed. The presence of these characteristic $Mg(OH)_2$ features was consistent with AES-determined O:(Mg+Al+Zn) or O:(Mg+Al) atomic ratios ranging from 1.2 to 1.7 (Figure 6.3), which indicated the degree of hydration of the aged corrosion filaments increased relative to the fresh corrosion filaments. It is, therefore, proposed that aging in the solution caused the transformation of a portion of the corrosion filaments from MgO to $Mg(OH)_2$, with the larger lattice parameter of the latter causing the compressive stresses necessary to create the ruptured appearance of the columnar regions. It is also suspected that the noticeable brightening of the corrosion filaments during aging in the solution (Figure 5.2, Figure 5.5, Figure 5.25) may have corresponded to a gradual transition from MgO to $Mg(OH)_2$.

The significant morphological differences between the pre-existing surface film (nanoporous with continuous surface coverage) and the corrosion filaments (dense with the exception of cracks and ruptures) could help to explain the differences in catalytic activity of each structure. However, no significant differences between the respective corrosion product structures on AZ31B and AM30 were detected in the analysis. Therefore, as mentioned in Section 6.1, the increased cathodic activity observed on the corrosion fila-

ments on AZ31B relative to AM30 can most likely be attributed to differences in the alloying content or microstructures of each alloy.

6.3. Preferential Dissolution and Elemental Segregation

Preferential dissolution and elemental segregation were observed throughout the analysis of the corroded structures for both the AZ31B and AM30 alloys. Preferential dissolution was identified primarily from the TEM imaging of intact Al-Mn particles within the corroded structures, since this required the preferential dissolution of the Mg matrix phase. Elemental segregation was observed at the film/metal and filament/metal interfaces in addition to the film or filament surfaces using TEM-EDS and AES analysis, respectively.

Al-Mn particles were embedded in the pre-existing surface film (Figure 5.11[a], Figure 5.30[a]), fresh corrosion filaments (Figure 5.16[a], Figure 5.34[a]) and aged corrosion filaments (Figure 5.20[a], Figure 5.38[a]) for each alloy. It is important to recall that the Al-Mn particles in each alloy had different stoichiometries; the particles in the AZ31B alloy were identified as $Al_{11}Mn_4$ while the particles in the AM30 alloy were identified as Al_8Mn_5. Although a direct comparison of the electrochemical behaviour of these two phases is not available in the literature, Al-Mn particles with a lower Al:Mn ratio are generally reported to be more noble and thus more detrimental to the corrosion resistance of Mg alloys [19,89]. Therefore, the Al-Mn particles in the corroded structures on the AM30 alloy would collectively be expected to have greater cathodic potency under the assumption that they possessed the same total exposed surface area as in the AZ31B alloy. In or-

der to test this assumption, the collective surface areas of particles in each alloy were estimated by calculating the surface area of an average-sized particle (assuming a spherical shape) and multiplying by the estimated number density of particles in the respective alloy. The AZ31B alloy contained an estimated 3.3 μm^2 of Al-Mn particle surface area per μm^3 of metal, while the AM30 alloy contained an estimated 1.9 μm^2 per μm^3 of metal. Therefore, if it is assumed that the size and number density of particles within the corroded structures mirrored that of the microstructures of the underlying metal, the collective surface area of particles in the AZ31B corroded structures was greater than that of the AM30 alloy. It is not clear which of these two factors (Al-Mn phase cathodic potency or total exposed surface area) was more significant, and therefore it is unknown whether the collective population of Al-Mn particles in AZ31B or AM30 would be expected to provide higher cathodic kinetics to the corroded structures on each alloy.

The Al and Zn EDS line profiles across the film/metal and filament/metal interfaces presented in Chapter 5 are re-plotted for comparison in Figure 6.4. The data is presented as Al/(Mg+Al+Zn), Zn/(Mg+Al+Zn) and Al/(Mg+Al) atomic percentages in order to emphasize the quantity of Al and Zn relative to the respective solid-solution components in each alloy. The first observation from these plots is that the films and filaments were generally enriched with Al relative to the base metals. As discussed in Chapter 2, Al-enrichment is often identified within the surface films formed on Mg-Al alloys, and as such this result is not surprising. The mechanism by which Al enriches in the surface films formed on Mg has been proposed to involve the higher affinity of O_2 for Al than for

Mg [90], since Al_2O_3 (-788 kJ per mole of Al) has a lower Gibbs free energy of formation than MgO (-559 kJ per mole of Mg).

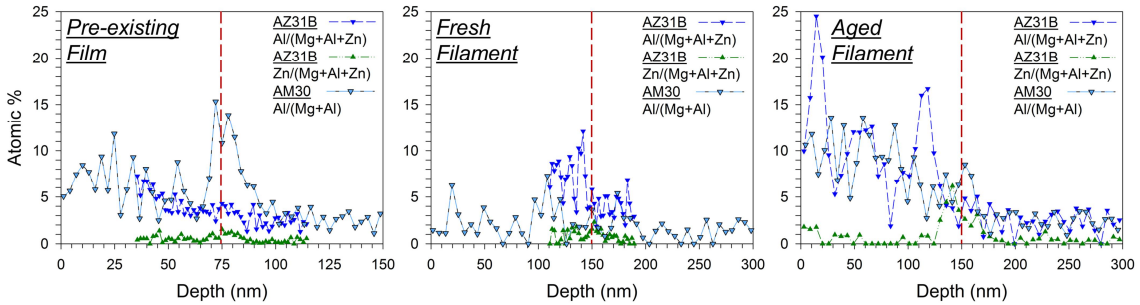

Figure 6.4: Al/(Mg+Al+Zn), Zn/(Mg+Al+Zn) and Al/(Mg+Al) atomic percentage line profiles across the pre-existing surface film, fresh corrosion filament and aged corrosion filament/metal interfaces on AZ31B and AM30. Atomic percentages were calculated from the EDS line profiles presented in Figure 5.12, Figure 5.17, Figure 5.21, Figure 5.31, Figure 5.35 and Figure 5.39. The vertical dashed lines represent the film/metal or filament/metal interfaces.

The enrichment of Al at the pre-existing film/metal interface of the AM30 alloy was somewhat surprising since a similar Al-enriched layer has only been previously observed underneath the corroded structures on higher Al-content Mg alloys containing the β-$Mg_{17}Al_{12}$ phase [65,67,91,92]. As mentioned in Chapter 2, the enrichment of Zn underneath surface films of Zn-containing Mg alloys has been previously reported [32,40,45]. The fact that Al-enrichment was not observed on the AZ31B alloy (for which Zn-enrichment was instead observed) suggests that a competitive process, in which all but the noblest alloying element are preferentially corroded, dictates which element segregates at

the pre-existing film/metal interface. Zn, with a standard electrode potential of -1.0 V_{SCE}, would thus be expected to be left behind in its metallic form as Al (-1.9 V_{SCE}) and Mg (-2.6 V_{SCE}) both preferentially corrode from the AZ31B alloy. The AM30 alloy, which contained no detectable Zn, would instead be expected to have Al left behind in its metallic form as Mg preferentially corrodes. The greater enrichment of Al at the pre-existing film/metal interface on AM30 relative to Zn at the pre-existing film/metal interface on AZ31B (Figure 6.4) presumably reflects the higher alloying content of Al relative to Zn.

The lack of significantly increased elemental enrichment at the fresh corrosion filament/metal interfaces, despite the large volume of metal that corroded during corrosion filament formation, suggests that the intense local anodic currents at the heads of the corrosion filaments (Figure 5.5, Figure 5.25) were strong enough to dissolve all of the alloying elements. The noble element enrichment observed at the aged corrosion filament/metal interfaces likely cannot be attributed to preferential dissolution due to the fact that the filament-consumed areas of the surface were cathodically protected (Figure 5.5, Figure 5.25). The comparable quantities of Al-enrichment at the aged corrosion filament/metal interface of AM30 and Zn-enrichment at the aged corrosion filament/metal interface of AZ31B (Figure 6.4) is somewhat remarkable when considering the lower alloying content of the latter element, and also supports the hypothesis that the elemental enrichment mechanism in this case is not equivalent to the case of the pre-existing films. A potential explanation for the elemental enrichment at the aged corrosion filament/metal interfaces could instead involve the rejection of oxidized noble elements from the corrosion filament onto the metal surface, which the result presented in Figure 5.22 alludes to.

The higher thermodynamic tendency of reducing oxidized Zn relative to Al could then explain the comparable levels of enrichment of the respective elements underneath the aged corrosion filaments on each alloy despite the lower alloying content of Zn. The segregation of metallic Al or Zn to the corrosion filament/metal interfaces could be a significant factor in the cathodic behaviour of corrosion filaments, since the cathodic kinetics on Al [93,94] and Zn [46] are approximately an order of magnitude or larger than the cathodic kinetics on Mg near the typical corrosion potentials of Mg. It should also be noted that the concentration of Al and Zn at the respective interfaces of each alloy could possibly be significantly higher than detected with EDS quantification, due to tilted boundary layers and/or limited TEM imaging resolution.

The Al/(Mg+Al+Zn), Zn/(Mg+Al+Zn) and Al/(Mg+Al) atomic percentages calculated from the quantification of the AES depth profiles are plotted for comparison in Figure 6.5. The depth profiles revealed significant enrichment of Al at the top surfaces of the pre-existing surface films; interestingly, this result appears to be unique from previous studies which employed XPS and TEM-EDS analysis of the surface films formed on Mg-Al alloys [32,34–38,40]. However, this result would appear to be consistent with the mechanism discussed above for the general enrichment of Al within the corroded structures, since the higher affinity of O_2 for Al versus Mg would result in segregation of the former element to the top surface where O_2 is abundantly present either in air or dissolved in solution. Unlike the pre-existing surface films, an Al-depleted surface layer appeared to be present on the fresh corrosion filaments of each alloy. This was rather unexpected because TEM imaging appeared to reveal that the pre-existing surface film was still present

overtop the fresh corrosion filament (Figure 5.15[d], Figure 5.33[b]). The reason for the depletion of Al from this layer is therefore not clear; however, it would appear to indicate that the overlying pre-existing surface film was modified in some way as a result of propagation of the underlying corrosion filament. The aged corrosion filaments on each alloy displayed an Al-depleted region similar to the fresh corrosion filaments while also displaying an overlying Al-enriched region similar to the pre-existing surface films, which could presumably be explained again by the higher affinity of O_2 for Al manifesting itself as the filament aged in the solution.

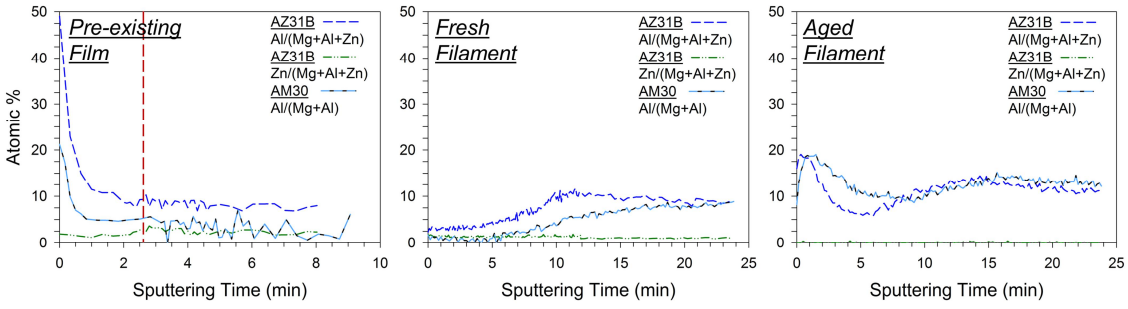

Figure 6.5: Al/(Mg+Al+Zn), Zn/(Mg+Al+Zn) and Al/(Mg+Al) atomic percentage depth profiles through the pre-existing surface film, fresh corrosion filament and aged corrosion filament on AZ31B and AM30. Atomic percentages were calculated from the AES quantification results presented in Figure 5.13, Figure 5.18, Figure 5.24, Figure 5.32, Figure 5.36 and Figure 5.40. The vertical dashed line represents the approximate location of the beginning of the transition from the pre-existing surface film to the metal for both alloys.

6.4. Summary of Corroded Structure Characteristics

A summary of the key characteristics from the three corroded structures characterized on each of the AZ31B and AM30 alloys is provided in Table 6.1. These characteristics are considered to be the most important to the discussion of the filiform-like corrosion mechanism in Section 6.5.

Table 6.1: Summary comparison of the three corroded structures characterized from each alloy (*The SAD-detected $Mg[OH]_2$ structure present in the aged corrosion filament on AM30 likely was present but undetected in the aged corrosion filament on AZ31B, since both corroded structures contained ruptured columnar features characteristic of $Mg[OH]_2$).

Alloy	Corroded Structure	Thickness	Morphology	Crystal Structure (SAD)	Embedded Al-Mn Particles	Elemental Enrichment at Film/Metal or Filament/Metal Interface
AZ31B	**Pre-existing Surface Film**	50-120 nm	Porous, uniform coverage	MgO	$\underline{Al_{11}Mn_4}$ (estimated 3.3 μm^2 total particle surface area per μm^3 of material)	$\underline{Zn}$ Zn/(Mg+Al+Zn) ≈ 2 At. %
	Fresh Corrosion Filament	>1 μm	Dense, through-thickness cracks	MgO		$\underline{Zn}$ Zn/(Mg+Al+Zn) ≈ 2 At. %
	Aged Corrosion Filament	>1 μm	Dense, through-thickness cracks and ruptures	MgO (*)		$\underline{Zn}$ Zn/(Mg+Al+Zn) ≈ 6 At. %
AM30	**Pre-existing Surface Film**	70-160 nm	Porous, uniform coverage	MgO	$\underline{Al_8Mn_5}$ (estimated 1.9 μm^2 total particle surface area per μm^3 of material)	$\underline{Al}$ Al/(Mg+Al) ≈ 15 At. %
	Fresh Corrosion Filament	>1 μm	Dense, through-thickness cracks	MgO		None detected
	Aged Corrosion Filament	>1 μm	Dense, through-thickness cracks and ruptures	MgO/ $Mg(OH)_2$ (*)		$\underline{Al}$ Al/(Mg+Al) ≈ 8 At. %

6.5. Filiform-Like Corrosion Mechanism

Although the localized corrosion investigated in this work resembles filiform corrosion, it is important to remember that the same differential aeration-based mechanism generally accepted to drive filiform corrosion beneath coated Fe and Al-based alloys cannot be applied to Mg alloys. The reasons for this are that the main cathodic reaction in the corrosion of Mg is HE instead of oxygen reduction, and the hydrolysis of Mg^{2+} cations increases the local solution pH instead of decreasing it as is the case for Al^{3+} and Fe^{3+} cations [15]. As discussed in Chapter 2, Scanning Kelvin probe and SVET measurements performed by Williams and coworkers demonstrated that a differential electrocatalytic-based mechanism drives filiform-like corrosion on both uncoated and coated pure Mg [12,15] as well as uncoated AZ31B [16]. The SVET results in this work were in agreement with the above mechanism since it was similarly demonstrated that net cathodic currents above the corrosion filaments were coupled with net anodic currents at the fronts of the propagating filaments on both AZ31B (Figure 5.5) and AM30 (Figure 5.25). However, a more detailed analysis revealed some potentially critical differences between the electrochemical behaviour of the filiform-like corrosion on each alloy (Section 6.1). The variations in the characterized corroded structures on each alloy, which primarily involved preferential dissolution and elemental segregation (Section 6.3), were thus considered as potential factors in their different electrochemical behaviours. These factors are discussed in the following sub-section in an attempt to further the understanding on the

source(s) of cathodic activation of the corrosion filaments on AZ31B and AM30 and by extension other Mg alloys not investigated in this work.

6.5.1. Potential Sources of Cathodic Activation

As mentioned in Chapter 2, the proposed mechanism by Williams et al. [16] for the cathodic activation of the filament-covered regions on AZ31B (and by extension, AM30) states that it is a result of the accumulation of noble Al-Mn particles within the corrosion filaments (Figure 2.12). The strongest evidence to date for this mechanism was provided by Merino et al. [67], who showed with plan view SEM imaging that Al-Mn particles were present in the corroded regions of a AZ31B alloy exposed to 5 wt.% NaCl salt fog. The present work has provided clear evidence that Al-Mn particles are left embedded in the corrosion filaments during filiform-like corrosion. However, it was also shown in this work that Al-Mn particles were present in the pre-existing surface films of each alloy which covered regions not yet consumed by corrosion filaments. If the cathodic activation of AZ31B and AM30 is caused by the accumulation of Al-Mn particles, this raises a question as to why cathodic currents would be confined primarily to the corrosion filament when Al-Mn particles are available on the intact surface by being present within the pre-existing surface film. The answer could lie in the fact that, for equal surface areas, a larger number of Al-Mn particles could reasonably be assumed to be present in the corrosion filament than in the pre-existing surface film due to the greater thickness of the corrosion filament. This explanation would require the assumption that electrons from the metal can

freely travel to all regions of the corrosion filament and pre-existing surface film. As discussed in Section 6.3, the AZ31B and AM30 alloys both contained Al-Mn particles, but with different stoichiometries and collective surface areas. Therefore, it cannot be definitively stated which alloy would be expected to encompass a larger cathodic contribution from the Al-Mn particles, and the possibility of Al-Mn particles causing cathodic activation cannot be definitively evaluated by interpreting the comparative electrochemical results discussed in Section 6.1. However, it is noted that the magnitudes of cathodic currents detected at relatively short times after filiform corrosion initiation were similar between each alloy (Figure 6.2). If the embedded Al-Mn particles indeed caused the corrosion filaments to become cathodically active, this would suggest that they induced relatively similar cathodic effects on each alloy and that another mechanism could be responsible for the divergence of the detected cathodic currents after prolonged immersion times (Figure 6.2).

The key findings from this work are summarized in an updated schematic representation of the filiform-like corrosion mechanism on AZ31B and AM30 alloys, presented in Figure 6.6. The particles and elemental enrichment were generically referred to as "noble" because it is suspected that this schematic representation can be applied to the filiform-like corrosion process on many other Mg alloys containing a wide range of alloying elements. It is proposed that the through-thickness cracks observed in the corrosion filaments play a key role in the cathodic activation mechanism, by providing pathways for ionic passage to cathodic sites either within the filament or at the corrosion filament/metal interface. For example, considering again the cathodic contribution of Al-Mn particles,

the presence of the through-thickness cracks could explain why cathodic currents were confined to the corrosion filaments when both the pre-existing surface films and corrosion filaments contained embedded Al-Mn particles. A crack is thus shown as a local cathode in the presented schematic representation. Three possible cathodic sites within the crack are labelled, the first of which is the previously-mentioned Al-Mn particles (Figure 6.6, cathodic site #1).

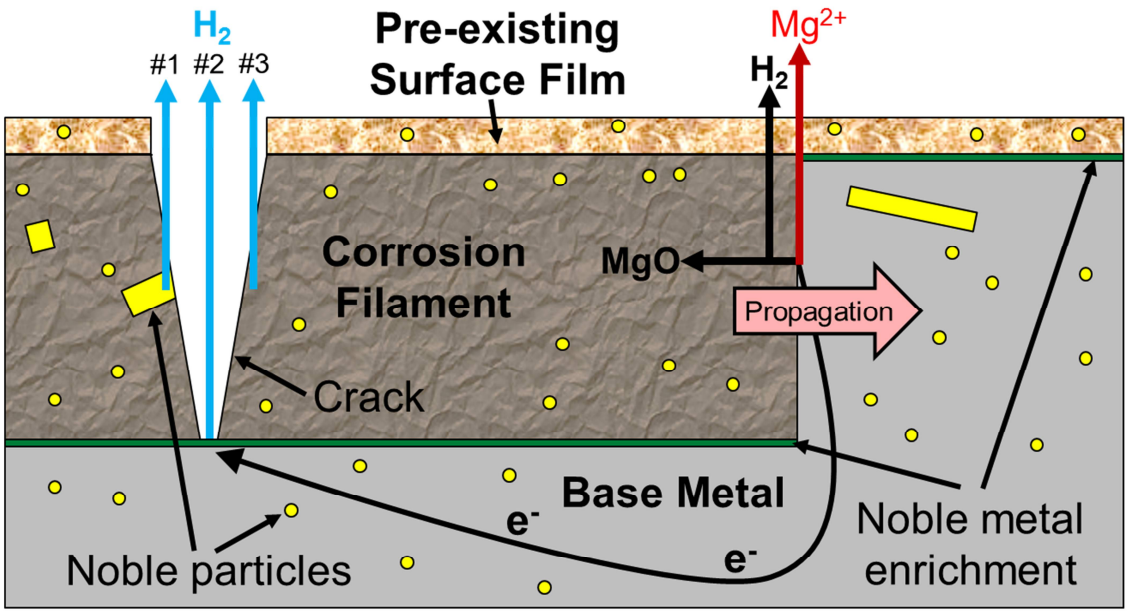

Figure 6.6: Schematic representation of the filiform-like corrosion mechanism, including three proposed cathodic sites responsible for cathodic activation of the corrosion filaments formed on AZ31B and AM30. The proposed cathodic sites include noble intermetallic particles (#1), noble metal enrichment (#2) and the corrosion filament itself (#3).

The interfacial enrichment of Zn and Al observed at the corroded structures on AZ31B and AM30, respectively, has the potential to increase the rate of cathodic kinetics at potentials near the corrosion potential of Mg (Section 6.3). This noble metal enrichment is thus proposed as a second possible site causing cathodic activation (Figure 6.6, cathodic site #2). A possible detraction from this proposal is the fact that the corrosion filament-covered areas on AZ31B and AM30 were cathodically activated immediately after their formation (Figure 5.6, Figure 5.26), while significant noble metal enrichment was not observed at the corrosion filament/metal interfaces until they were analyzed in the aged condition. However, it is possible that the noble metal-enriched layers acted as "secondary" cathodic catalysts in addition to primary cathodic catalysts (such as embedded Al-Mn particles). In this context, the differing quantities of noble metal enrichment at the corroded structures of AZ31B and AM30 could explain the divergence of detected cathodic currents on each alloy after prolonged immersion times (Figure 6.2). It can be seen in Table 6.1 that the detected quantity of Zn in the AZ31B corroded structures was higher at the aged corrosion filament/metal interface than at the pre-existing film/metal interface, which would suggest that the corrosion filament-covered regions became increasingly more cathodic with respect to the intact pre-existing film-covered regions as a function of immersion time. By contrast, the detected quantity of Al in the AM30 corroded structures was higher at the pre-existing surface film/metal interface than at the aged corrosion filament/metal interface, suggesting that the secondary cathodic catalyst in this case (i.e. Al-enrichment) was higher at the intact pre-existing film-covered regions. Both of these observations are consistent with the respective electrochemical behaviour of each alloy,

since the total cathodic current on AZ31B definitively increased with immersion time whereas the total cathodic current on AM30 did not increase significantly after the initiation of corrosion filaments (Figure 6.2).

A third potential cathodic site that deserves consideration is the MgO corrosion filament itself (Figure 6.6, cathodic site #3). It has been previously speculated [95] that corrosion films can act as cathodes, and in this case, the dense corrosion filament might allow higher electronic conductivity than the pre-existing surface film and, therefore, more efficient cathodic kinetics. In addition, the roughened surface that was previously observed on the corrosion filaments formed on pure Mg by Schmutz et al. [51] (Figure 2.10) could conceivably provide a higher effective surface area necessary to catalyze the HE reaction. However, investigations of cathodic disbondment of organic coatings have shown that the relatively good resistance of $MgZn_2$ electrodes to coating failure can be attributed to the poor cathode properties of the MgO surface film [96,97]. Schmutz et al. [51] also surmised from the excessive charging observed during Ar ion sputtering that the corrosion filaments on pure Mg were relatively electronically insulating, which would tend to negate them effectively transporting electronic current in the filiform-like corrosion process. For these reasons, the possibility of the corrosion filament itself acting as a significant cathode is considered to be the least likely of the three identified potential cathodic sites. Even if the corrosion filament does contribute to the cathodic activation mechanism, it is clear from the observed electrochemical differences between AZ31B and AM30 filiform-like corrosion (Figure 6.1, Figure 6.2) that other factors must affect the magnitude of cathodic activation.

6.5.2. Cathodic Activation and the Negative Difference Effect

As noted in Chapter 2, the cathodic activation of corroded Mg has been proposed as the reason behind the NDE (i.e. increased HE rate during anodic polarization) [12,13,23,26]. Although this study has focused on cathodic activation of AZ31B and AM30 during open-circuit corrosion, it is evident from SVET measurements at the OCC that intense local net anodes are formed at the fronts of propagating corrosion filaments (Figure 5.5, Figure 5.25). Thus, a discussion on the relationship between cathodic activation and the NDE in the context of localized corrosion is warranted. Numerical area integration of previous SVET-measured current densities on both pure Mg [12] and AZ31B [16] in addition to the present work (Figure 5.7, Figure 5.27) has demonstrated a well-correlated charge balance between the anodic currents at propagating corrosion fronts and the uniform cathodic currents observed across the previously corroded regions. It is surprising, then, that HE at the propagating corrosion front is readily observed to occur much faster than on the previously corroded regions (Figure 5.5, Figure 5.25). This "extra" HE was independently verified by Lebouil et al. [98] via simultaneous time-resolved measurement of dissolved Mg and evolved H_2 during potentiostatic anodic dissolution of pure Mg. Firstly, they demonstrated that the number of moles of dissolved Mg was greater than that expected based on the number of electrons collected by the potentiostat, which indicated the availability of extra electrons for consumption by the HE reaction. They also demonstrated that the number of moles of H_2 evolved was greater than the number which could be created by consumption of the expected extra electrons by the HE reaction. This could only

be explained by a greater amount of oxidized Mg than measured, and this discrepancy was attributed to the formation of insoluble MgO or $Mg(OH)_2$ films [98]. Rossucker et al. [99] have since performed similar time-resolved measurements of galvanostatically polarized pure Mg, which demonstrated that the currents associated with HE and film formation are indeed closely correlated with one another. In the present work, the corrosion filaments were shown to be formed primarily as MgO. For these reasons, it is expected that the extra HE at the fronts of the propagating corrosion filaments during open-circuit corrosion of AZ31B and AM30 was a product of the following overall direct reaction:

$$Mg + H_2O \rightarrow MgO + H_2 \tag{6.1}$$

The rest of the oxidized Mg at the corrosion front is detectable by SVET as Mg^{2+} and, as mentioned above, is entirely charge-balanced by the detected cathodic ionic currents at the cathodically-activated corrosion filaments. Thus, the electrons drawn from the propagation front to the cathodically-activated corrosion filaments are analogous to the electrons drawn by a potentiostat during external anodic polarization of Mg. This leads to the conclusion that the extra HE (i.e. the NDE) which occurs at the localized sites of anodic activity is not a direct result of cathodic activation. It is instead attributed to the formation of an insoluble MgO corrosion product. The extra HE at the propagating corrosion front as a result of Equation (6.1) is shown schematically in Figure 6.6.

Chapter 7: Conclusions and Recommendations

In this investigation, the filiform-like corrosion behaviour of Mg alloys AZ31B and AM30 was investigated in a dilute NaCl solution using electrochemical and microanalytical techniques. The key findings of the investigation are summarized below:

(1) Scanning vibrating electrode technique (SVET) testing demonstrated that the corrosion filaments on both alloys were cathodically activated, which was consistent with previous investigations on pure Mg [12,15] and AZ31B [16].

(2) Polarization and SVET testing revealed the corrosion filaments on AZ31B to be more cathodically active than on AM30 after prolonged immersion periods. As a result, the AZ31B alloy suffered more severe filiform-like corrosion after prolonged immersion periods.

(3) Transmission electron microscopy (TEM) and Auger electron spectroscopy (AES) analysis revealed the freshly formed corrosion filaments on both alloys to comprise primarily MgO. Following a discussion of the work of Lebouil et al. [98] and Rossrucker et al. [99], it was deduced that the rapid hydrogen evolution (HE) observed at the fronts of the propagating corrosion filaments was a product of the direct reaction of Mg and H_2O to form MgO and H_2. TEM and AES analysis suggested that the corrosion filaments became partially hydrated to $Mg(OH)_2$ as a result of aging in the salt solution.

(4) Through-thickness cracks were observed in the corrosion filaments, which were postulated to play a major role in the cathodic activation mechanism. It was proposed that the cracks facilitated ionic flow to specific cathodic sites within the corrosion filament or at the corrosion filament/metal interface of each alloy.

(5) Al-Mn particles were embedded in the corrosion filaments of both alloys. This provided some confirmatory evidence for the proposed mechanism of Williams et al. [16] whereby the filaments were cathodically activated due to an enrichment of noble Al-Mn particles. Assuming that the Al-Mn particles were responsible for the "primary" cathodic currents detected after initial filament formation, the similar cathodic current magnitudes detected on each alloy within short immersion times suggested that the cathodic contribution of the Al-Mn particles in each alloy were relatively similar.

(6) Zn-enrichment was observed at the aged corrosion filament/metal interface of the AZ31B alloy, while Al-enrichment was observed at the aged corrosion filament/metal interface of the AM30 alloy. The noble metal-enriched layers were proposed to act as "secondary" cathodic enablers, with the differences in the respective concentrations of the layers after aging presumably causing the divergence of the cathodic current magnitudes detected on each alloy after prolonged immersion periods.

Conclusions (2) and (6) listed above suggested that alloying with Zn has a detrimental effect on the filiform corrosion susceptibility of Mg-Al-Zn alloys. However, the

differences in the average grain size, particle size, particle distribution and particle stoichiometry within each alloy meant that the effect of alloyed Zn could not be determined with absolute certainty. Nevertheless, the significant differences in the severity of filiform-like corrosion observed on the AZ31B and AM30 alloys made it clear that the alloy content and/or microstructure likely has a significant effect on the filiform corrosion process on Mg alloys.

The experimental methods employed in this investigation can serve as a framework for studying the cathodic activation susceptibility (and, thus, filiform corrosion susceptibility) of other Mg alloys. It is recommended that future work in this area focusses on binary or ternary alloys that are directly comparable to one another in terms of average grain size and particle size, distribution and stoichiometry. Doing so would enable more certain conclusions on the effects of various alloying elements on the cathodic activation susceptibility of Mg alloys under open circuit immersion conditions. It should also be noted that the direct correlation of the potentiodynamic polarization and SVET results in this investigation could mean that it is not necessary to employ the relatively specialized equipment needed for SVET testing. Simple polarization testing can be used to probe the cathodic potency of corrosion filaments on an Mg alloy surface, provided that the corrosion filaments have consumed a significant portion of the surface.

References

[1] L.C. Lau, K.T. Lee, A.R. Mohamed, Global warming mitigation and renewable energy policy development from the Kyoto Protocol to the Copenhagen Accord—A comment, Renew. Sustain. Energy Rev. 16 (2012) 5280–5284. doi:10.1016/j.rser.2012.04.006.

[2] Improving Energy Performance in Canada, Natural Resources Canada, 2012. http://oee.nrcan.gc.ca/publications/statistics/parliament10-11/pdf/parliament10-11.pdf (accessed December 28, 2014).

[3] S.C. Davis, S.W. Diegel, R.G. Boundy, Transportation Energy Data Book, 33rd ed., Oak Ridge National Lab., TN (US), 2014. http://www.osti.gov/scitech/biblio/788356 (accessed December 29, 2014).

[4] J. Norman, H.L. Maclean, C.A. Kennedy, Comparing High and Low Residential Density: Life-Cycle Analysis of Energy Use and Greenhouse Gas Emissions, J. Urban Plan. Dev. (2006) 10–21. doi:10.1061/(ASCE)0733-9488(2006)132:1(10).

[5] E.W. Martin, S. a. Shaheen, Greenhouse Gas Emission Impacts of Carsharing in North America, IEEE Trans. Intell. Transp. Syst. 12 (2011) 1074–1086. doi:10.1109/TITS.2011.2158539.

[6] United States - Canada Clean Energy Dialogue, (2014). http://www.climatechange.gc.ca/dialogue/default.asp?lang=Enn=E47AAD1C-1 (accessed December 31, 2014).

[7] K. Sadayappan, D. Cariou, Three-Country R&D Collaboration Designs a Lighter Automotive Front End, (2013). http://www.nrcan.gc.ca/mining-materials/materials-technology/highlights/8270 (accessed December 31, 2014).

[8] E. Nyberg, A. Luo, Magnesium for future autos, Adv. Mater. Process. 166 (2008) 35–37. http://www.osti.gov/scitech/biblio/946646

[9] A. Dubreuil, L. Bushi, S. Das, A. Tharumarajah, X. Gong, A Comparative Life Cycle Assessment of Magnesium Front End Autoparts, 2010. http://papers.sae.org/2012-01-2325/.

[10] H. Friedrich, S. Schumann, Research for a “new age of magnesium” in the automotive industry, J. Mater. Process. Technol. 117 (2001) 276–281. doi:10.1016/S0924-0136(01)00780-4.

[11] M.K. Kulekci, Magnesium and its alloys applications in automotive industry, Int. J. Adv. Manuf. Technol. 39 (2007) 851–865. doi:10.1007/s00170-007-1279-2.

[12] G. Williams, H. Neil McMurray, Localized Corrosion of Magnesium in Chloride-Containing Electrolyte Studied by a Scanning Vibrating Electrode Technique, J. Electrochem. Soc. 155 (2008) C340. doi:10.1149/1.2918900.

[13] G.S. Frankel, A. Samaniego, N. Birbilis, Evolution of hydrogen at dissolving magnesium surfaces, Corros. Sci. 70 (2013) 104–111. doi:10.1016/j.corsci.2013.01.017.

[14] R.C. McCune, V. Upadhyay, Y.-M. Wang, D. Battocchi, The Use of AC-DC-AC Methods in Assessing Corrosion Resistance Performance of Coating Systems for Magnesium Alloys, in: N. Hort, S.N. Mathaudhu, N.R. Neelameggham, M. Alderman (Eds.), Magnes. Technol. 2013, John Wiley & Sons, Inc., Hoboken, NJ, USA, 2013: pp. 163–168. http://dx.doi.org/10.1002/9781118663004.ch27.

[15] G. Williams, R. Grace, Chloride-induced filiform corrosion of organic-coated magnesium, Electrochimica Acta. 56 (2011) 1894–1903. doi:10.1016/j.electacta.2010.09.005.

[16] G. Williams, H. ap Llwyd Dafydd, R. Grace, The localised corrosion of Mg alloy AZ31 in chloride containing electrolyte studied by a scanning vibrating electrode technique, Electrochimica Acta. 109 (2013) 489–501. doi:10.1016/j.electacta.2013.07.134.

[17] T. Cain, L.G. Bland, N. Birbilis, J.R. Scully, A Compilation of Corrosion Potentials for Magnesium Alloys, Corrosion. 70 (2014) 1043–1051. doi:10.5006/1257.

[18] G. Makar, J. Kruger, Corrosion of magnesium, Int. Mater. Rev. 38 (1993) 138–153. doi:10.1179/imr.1993.38.3.138.

[19] G. Song, A. Atrens, Understanding Magnesium Corrosion—A Framework for Improved Alloy Performance, Adv. Eng. Mater. 5 (2003) 837–858. doi:10.1002/adem.200310405.

[20] E. Ghali, W. Dietzel, K.-U. Kainer, General and Localized Corrosion of Magnesium Alloys: A Critical Review, J. Mater. Eng. Perform. 13 (2004) 7–23. doi:10.1361/10599490417533.

[21] R. Zeng, J. Zhang, W. Huang, W. Dietzel, K.U. Kainer, C. Blawert, et al., Review of studies on corrosion of magnesium alloys, Trans. Nonferrous Met. Soc. China. 16 (2006) s763–s771. doi:10.1016/S1003-6326(06)60297-5.

[22] G. Song, A. Atrens, D. John, X. Wu, J. Nairn, The anodic dissolution of magnesium in chloride and sulphate solutions, Corros. Sci. 39 (1997) 1981–2004. doi:10.1016/S0010-938X(97)00090-5.

[23] N. Birbilis, A.D. King, S. Thomas, G.S. Frankel, J.R. Scully, Evidence for enhanced catalytic activity of magnesium arising from anodic dissolution, Electrochimica Acta. 132 (2014) 277–283. doi:10.1016/j.electacta.2014.03.133.

[24] S. Bender, J. Goellner, A new theory for the negative difference effect in magnesium corrosion, Mater. Corros. 63 (2012) 707–712. doi:10.1002/maco.201106225.

[25] G. Williams, N. Birbilis, H.N. Mcmurray, The source of hydrogen evolved from a magnesium anode, Electrochem. Commun. 36 (2013) 1–5. doi:10.1016/j.elecom.2013.08.023.

[26] M. Curioni, The behaviour of magnesium during free corrosion and potentiodynamic polarization investigated by real-time hydrogen measurement and optical imaging, Electrochimica Acta. 120 (2014) 284–292. doi:10.1016/j.electacta.2013.12.109.

[27] J. Nordlien, S. Ono, N. Masuko, K. Nisancioglu, A TEM investigation of naturally formed oxide films on pure magnesium, Corros. Sci. 39 (1997) 1397–1414. doi:10.1016/S0010-938X(97)00037-1.

[28] H.B. Yao, Y. Li, A.T.S. Wee, An XPS investigation of the oxidation/corrosion of melt-spun Mg, Appl. Surf. Sci. 158 (2000) 112–119. doi:10.1016/S0169-4332(99)00593-0.

[29] M. Santamaria, F. Di Quarto, S. Zanna, P. Marcus, Initial surface film on magnesium metal: A characterization by X-ray photoelectron spectroscopy (XPS) and photocurrent spectroscopy (PCS), Electrochimica Acta. 53 (2007) 1314–1324. doi:10.1016/j.electacta.2007.03.019.

[30] M. Liu, S. Zanna, H. Ardelean, I. Frateur, P. Schmutz, G. Song, et al., A first quantitative XPS study of the surface films formed, by exposure to water, on Mg and on the Mg–Al intermetallics: Al3Mg2 and Mg17Al12, Corros. Sci. 51 (2009) 1115–1127. doi:10.1016/j.corsci.2009.02.017.

[31] M. Taheri, R.C. Phillips, J.R. Kish, G. a. Botton, Analysis of the surface film formed on Mg by exposure to water using a FIB cross-section and STEM–EDS, Corros. Sci. 59 (2012) 222–228. doi:10.1016/j.corsci.2012.03.001.

[32] K. a. Unocic, H.H. Elsentriecy, M.P. Brady, H.M. Meyer, G.L. Song, M. Fayek, et al., Transmission Electron Microscopy Study of Aqueous Film Formation and Evolution on Magnesium Alloys, J. Electrochem. Soc. 161 (2014) C302–C311. doi:10.1149/2.024406jes.

[33] F. Hermann, F. Sommer, H. Jones, R.G.J. Edyvean, Corrosion inhibition in magnesium-aluminium-based alloys induced by rapid solidification processing, J. Mater. Sci. 24 (1989) 2369–2379. doi:10.1007/BF01174498.

[34] C.B. Baliga, P. Tsakiropoulos, Development of corrosion resistant magnesium alloys Part 1 Characterisation of splat quenched Mg-10AI and Mg-16AI alloys, Mater. Sci. Technol. 9 (1993) 507–511. doi:10.1179/mst.1993.9.6.507.

[35] C.B. Baliga, P. Tsakiropoulos, Development of corrosion resistant magnesium alloys Part 2 Structure of corrosion products on rapidly solidified Mg-16AI alloys, Mater. Sci. Technol. 9 (1993) 513–519. doi:10.1179/mst.1993.9.6.513.

[36] J.H. Nordlien, K. Nisancioglu, S. Ono, N. Masuko, Morphology and Structure of Oxide Films Formed on MgAl Alloys by Exposure to Air and Water, J. Electrochem. Soc. 143 (1996) 2564–2572. doi:10.1149/1.1837048.

[37] J.H. Nordlien, K. Nisancioglu, S. Ono, N. Masuko, Morphology and Structure of Water-Formed Oxides on Ternary MgAl Alloys, J. Electrochem. Soc. 144 (1997) 461–466. doi:10.1149/1.1837432.

[38] S. Mathieu, C. Rapin, J. Steinmetz, P. Steinmetz, A corrosion study of the main constituent phases of AZ91 magnesium alloys, Corros. Sci. 45 (2003) 2741–2755. doi:10.1016/S0010-938X(03)00109-4.

[39] N.T. Kirkland, J. Lespagnol, N. Birbilis, M.P. Staiger, A survey of bio-corrosion rates of magnesium alloys, Corros. Sci. 52 (2010) 287–291. doi:10.1016/j.corsci.2009.09.033.

[40] R.C. Phillips, J.R. Kish, Nature of Surface Film on Matrix Phase of Mg Alloy AZ80 Formed in Water, Corrosion. 69 (2013) 813–820. doi:10.5006/0938.

[41] B.P. Zhang, Y. Wang, L. Geng, Research on an Mg-Zn alloy as a degradable biomaterial., Acta Biomater. 6 (2010) 626–40. doi:10.1016/j.actbio.2009.06.028.

[42] S. Cai, T. Lei, N. Li, F. Feng, Effects of Zn on microstructure, mechanical properties and corrosion behavior of Mg–Zn alloys, Mater. Sci. Eng. C. 32 (2012) 2570–2577. doi:10.1016/j.msec.2012.07.042.

[43] Y. Song, E.-H. Han, D. Shan, C.D. Yim, B.S. You, The effect of Zn concentration on the corrosion behavior of Mg–xZn alloys, Corros. Sci. 65 (2012) 322–330. doi:10.1016/j.corsci.2012.08.037.
[44] X. Xia, C.H.J. Davies, J.. Nie, N. Birbilis, Influence of Composition and Processing on the Corrosion of Magnesium Alloys Containing Binary and Ternary Additions of Zinc and Strontium, Corrosion. 71 (2015) 38–49. doi:10.5006/1417.
[45] M.J. Cristóbal, D. Gesto, P. Miniño, G. Pena, P. Rey, D. Verdera, An XPS analysis of the oxide surface layers formed on a friction stir processed magnesium alloy, Surf. Interface Anal. 44 (2012) 1030–1034. doi:10.1002/sia.4859.
[46] D. Orlov, K.D. Ralston, N. Birbilis, Y. Estrin, Enhanced corrosion resistance of Mg alloy ZK60 after processing by integrated extrusion and equal channel angular pressing, Acta Mater. 59 (2011) 6176–6186. doi:10.1016/j.actamat.2011.06.033.
[47] H. Okamoto, Mg-Mn (Magnesium-Manganese), J. Phase Equilibria Diffus. 29 (2008) 208–209. doi:10.1007/s11669-008-9272-5.
[48] N.N. Aung, W. Zhou, Effect of grain size and twins on corrosion behaviour of AZ31B magnesium alloy, Corros. Sci. 52 (2010) 589–594. doi:10.1016/j.corsci.2009.10.018.
[49] I.J. Polmear, Light Alloys, 3rd ed., Arnold, London, U.K., 1995. http://books.google.ca/books?id=KNZGAAAAYAAJ.
[50] D. Gandel, M. Easton, M. Gibson, N. Birbilis, Influence of Mn and Zr on the Corrosion of Al-Free Mg Alloys: Part 1-Electrochemical Behavior of Mn and Zr, Corrosion. 69 (2013) 666–671. doi:10.5006/0827.
[51] P. Schmutz, V. Guillaumin, R.S. Lillard, J. a. Lillard, G.S. Frankel, Influence of Dichromate Ions on Corrosion Processes on Pure Magnesium, J. Electrochem. Soc. 150 (2003) B99. doi:10.1149/1.1554721.
[52] R. Tunold, H. Holtan, M.-B.H. Berge, A. Lasson, R. Steen-Hansen, The Corrosion of Magnesium in Aqueous Solution Containing Chloride Ions, Corros. Sci. 17 (1977) 353–365. doi:10.1016/0010-938X(77)90059-2.
[53] N. Hara, Y. Kobayashi, D. Kagaya, N. Akao, Formation and breakdown of surface films on magnesium and its alloys in aqueous solutions, Corros. Sci. 49 (2007) 166–175. doi:10.1016/j.corsci.2006.05.033.
[54] K. Ralston, G. Williams, N. Birbilis, Effect of pH on the Grain Size Dependence of Magnesium Corrosion, Corrosion. 68 (2012) 507–517. doi:10.5006/i0010-9312-68-6-507.
[55] L. Wang, T. Shinohara, B.-P. Zhang, Corrosion behavior of Mg, AZ31, and AZ91 alloys in dilute NaCl solutions, J. Solid State Electrochem. 14 (2010) 1897–1907. doi:10.1007/s10008-010-1020-1.
[56] A. Samaniego, I. Llorente, S. Feliu, Combined effect of composition and surface condition on corrosion behaviour of magnesium alloys AZ31 and AZ61, Corros. Sci. 68 (2013) 66–71. doi:10.1016/j.corsci.2012.10.034.
[57] W. Song, H.J. Martin, A. Hicks, D. Seely, C.A. Walton, W.B. Lawrimore, et al., Corrosion behaviour of extruded AM30 magnesium alloy under salt-spray and immersion environments, Corros. Sci. 78 (2014) 353–368. doi:10.1016/j.corsci.2013.10.020.

[58] M. Taheri, J.R. Kish, N. Birbilis, M. Danaie, E. a. McNally, J.R. McDermid, Towards a Physical Description for the Origin of Enhanced Catalytic Activity of Corroding Magnesium Surfaces, Electrochimica Acta. 116 (2014) 396–403. doi:10.1016/j.electacta.2013.11.086.

[59] S. Rossi, M. Fedel, F. Deflorian, M. del Carmen Vadillo, Localized electrochemical techniques: Theory and practical examples in corrosion studies, Comptes Rendus Chim. 11 (2008) 984–994. doi:10.1016/j.crci.2008.06.011.

[60] S. Thomas, J. Izquierdo, N. Birbilis, R.M. Souto, Possibilities and Limitations of Scanning Electrochemical Microscopy of Mg and Mg alloys, Corrosion. 71 (2015) 171–183. doi:10.5006/1483.

[61] N. Birbilis, G. Williams, K. Gusieva, A. Samaniego, M. a. Gibson, H.N. McMurray, Poisoning the corrosion of magnesium, Electrochem. Commun. 34 (2013) 295–298. doi:10.1016/j.elecom.2013.07.021.

[62] A. Samaniego, N. Birbilis, X. Xia, G.S. Frankel, Hydrogen Evolution During Anodic Polarization of Mg Alloyed with Li, Ca, or Fe, Corrosion. 71 (2015) 224–233. doi:10.5006/1367.

[63] C.R. McCall, M. a. Hill, R.S. Lillard, Crystallographic pitting in magnesium single crystals, Corros. Eng. Sci. Technol. 40 (2005) 337–343. doi:10.1179/174327805X66326.

[64] ASTM B951-11, Standard Practice for Codification of Unalloyed Magnesium and Magnesium-Alloys, Cast and Wrought, ASTM International, West Conshohocken, PA, 2011. http://dx.doi.org/10.1520/b0951-11.

[65] a. Pardo, M.C. Merino, A.E. Coy, F. Viejo, R. Arrabal, S. Feliú, Influence of microstructure and composition on the corrosion behaviour of Mg/Al alloys in chloride media, Electrochimica Acta. 53 (2008) 7890–7902. doi:10.1016/j.electacta.2008.06.001.

[66] G.B. Hamu, D. Eliezer, L. Wagner, The relation between severe plastic deformation microstructure and corrosion behavior of AZ31 magnesium alloy, J. Alloys Compd. 468 (2009) 222–229. doi:10.1016/j.jallcom.2008.01.084.

[67] M.C. Merino, A. Pardo, R. Arrabal, S. Merino, P. Casajús, M. Mohedano, Influence of chloride ion concentration and temperature on the corrosion of Mg–Al alloys in salt fog, Corros. Sci. 52 (2010) 1696–1704. doi:10.1016/j.corsci.2010.01.020.

[68] L. Shang, I.H. Jung, S. Yue, R. Verma, E. Essadiqi, An investigation of formation of second phases in microalloyed, AZ31 Mg alloys with Ca, Sr and Ce, J. Alloys Compd. 492 (2010) 173–183. doi:10.1016/j.jallcom.2009.11.159.

[69] L. Xiao, L. Liu, Y. Zhou, S. Esmaeili, Resistance-Spot-Welded AZ31 Magnesium Alloys: Part I. Dependence of Fusion Zone Microstructures on Second-Phase Particles, Metall. Mater. Trans. A. 41 (2010) 1511–1522. doi:10.1007/s11661-010-0197-3.

[70] N. Birbilis, R.G. Buchheit, Electrochemical Characteristics of Intermetallic Phases in Aluminum Alloys, J. Electrochem. Soc. 152 (2005) B140. doi:10.1149/1.1869984.

[71] A. a. Luo, A.K. Sachdev, Development of a New Wrought Magnesium-Aluminum-Manganese Alloy AM30, Metall. Mater. Trans. A. 38 (2007) 1184–1192. doi:10.1007/s11661-007-9129-2.

[72] J.M. Kim, J.M. Lee, J.H. Jun, K.T. Kim, W.J. Jung, Effects of Zn and Sn Additions on the Mechanical Properties of Mg-3%Al Alloy, Mater. Sci. Forum. 539-543 (2007) 1775–1779. doi:10.4028/www.scientific.net/MSF.539-543.1775.

[73] M.-C. Zhao, P. Schmutz, S. Brunner, M. Liu, G. Song, A. Atrens, An exploratory study of the corrosion of Mg alloys during interrupted salt spray testing, Corros. Sci. 51 (2009) 1277–1292. doi:10.1016/j.corsci.2009.03.014.

[74] Y. Hu, J.R. Kish, J.R. McDermid, W. Zheng, Effect of Some Microstructural Parameters on the Corrosion Resistance of Magnesium Alloys, in: S.N. Mathaudhu, W.H. Sillekens, N.R. Neelameggham, N. Hort (Eds.), Magnes. Technol. 2012, John Wiley & Sons, Inc., Hoboken, NJ, USA, 2012: pp. 271–276. http://dx.doi.org/10.1002/9781118359228.ch50.

[75] B.E. Carlson, R. Verma, W. Yuan, R.T. Szymanski, Friction Stir Welding of a Magnesium AZ31 Sub-Assembly, in: Sheet Met. Weld. Conf. XV, 2012.

[76] ASTM E112-10, Standard Test Methods for Determining Average Grain Size, ASTM International, West Conshohocken, PA, 2010. http://dx.doi.org/10.1520/b0951-11.

[77] EDS in the TEM Explained, Oxford Instruments, 2013. www.oxford-instruments.com/OxfordInstruments/media/nanoanalysis/brochures%20and%20thumbs/TEM-Explained.pdf (accessed January 5, 2015).

[78] R.F. Egerton, Electron Energy-Loss Spectroscopy in the Electron Microscope, 3rd ed., Springer, New York, NY, 2011. http://www.springer.com/gp/book/9781441995827.

[79] M. Danaie, S.X. Tao, P. Kalisvaart, D. Mitlin, Analysis of deformation twins and the partially dehydrogenated microstructure in nanocrystalline magnesium hydride (MgH2) powder, Acta Mater. 58 (2010) 3162–3172. doi:10.1016/j.actamat.2010.01.055.

[80] K. Miyamoto, Particle Number and Sizes Estimated from Sections —A History of Stereology, in: R. Takaki (Ed.), Res. Pattern Form., KTK Scientific Publishers, Tokyo, Japan, 1994: pp. 507–516. http://www.scipress.org/e-library/rpf/pdf/chap8/0507.PDF (accessed December 24, 2014).

[81] A. Shukla, A.D. Pelton, Thermodynamic Assessment of the Al-Mn and Mg-Al-Mn Systems, J. Phase Equilibria Diffus. 30 (2008) 28–39. doi:10.1007/s11669-008-9426-5.

[82] S. Chapman, Precautions When Making Light Element EDS Investigations, Protrain, n.d. http://www.emcourses.com/light_el.htm (accessed January 9, 2015).

[83] C.C. Ahn, Transmission Electron Energy Loss Spectrometry in Materials Science and The EELS Atlas, Second Edition, John Wiley & Sons, 2006. http://onlinelibrary.wiley.com/book/10.1002/3527605495.

[84] D. JU, Effect of casting parameters and deformation on microstructure evolution of twin-roll casting magnesium alloy AZ31, Trans. Nonferrous Met. Soc. China. 16 (2006) s874–s877. doi:10.1016/S1003-6326(06)60319-1.

[85] T. Laser, M.R. Nürnberg, A. Janz, C. Hartig, D. Letzig, R. Schmid-Fetzer, et al., The influence of manganese on the microstructure and mechanical properties of AZ31 gravity die cast alloys, Acta Mater. 54 (2006) 3033–3041. doi:10.1016/j.actamat.2006.02.039.

[86] K.D. Ralston, N. Birbilis, C.H.J. Davies, Revealing the relationship between grain size and corrosion rate of metals, Scr. Mater. 63 (2010) 1201–1204. doi:10.1016/j.scriptamat.2010.08.035.

[87] D. Song, A. Ma, J. Jiang, P. Lin, D. Yang, J. Fan, Corrosion behavior of equal-channel-angular-pressed pure magnesium in NaCl aqueous solution, Corros. Sci. 52 (2010) 481–490. doi:10.1016/j.corsci.2009.10.004.

[88] J.R. Kish, G. Williams, J.R. McDermid, J.M. Thuss, C.F. Glover, Effect of Grain Size on the Corrosion Resistance of Friction Stir Welded Mg Alloy AZ31B Joints, J. Electrochem. Soc. 161 (2014) C405–C411. doi:10.1149/2.0901409jes.

[89] O. Lunder, K. Nisancioglu, R.S. Hansen, Corrosion of die cast magnesium-aluminum alloys, SAE Tech. Pap. (1993). doi:10.4271/930755.

[90] G.L. Song, Corrosion Prevention of Magnesium Alloys, Elsevier Science, 2013. https://books.google.ca/books?id=OgxaAgAAQBAJ.

[91] a. Pardo, M.C. Merino, A.E. Coy, R. Arrabal, F. Viejo, E. Matykina, Corrosion behaviour of magnesium/aluminium alloys in 3.5wt.% NaCl, Corros. Sci. 50 (2008) 823–834. doi:10.1016/j.corsci.2007.11.005.

[92] M. Danaie, R.M. Asmussen, P. Jakupi, D.W. Shoesmith, G. a. Botton, The role of aluminum distribution on the local corrosion resistance of the microstructure in a sand-cast AM50 alloy, Corros. Sci. 77 (2013) 151–163. doi:10.1016/j.corsci.2013.07.038.

[93] F.H. Haynie, S.J. Ketcham, Electrochemical Behavior of Aluminum Alloys Susceptible to Intergranular Corrosion. II. Electrode Kinetics of Oxide-Covered Aluminum, Corrosion. 19 (1963) 403t–407t. doi:10.5006/0010-9312-19.12.403.

[94] K. Nisancioglu, Cathodic Polarization of Commercially Pure Aluminum, Corros. Sci. 19 (1979) 537–552. doi:10.1016/S0010-938X(79)80058-X.

[95] R. McNulty, J. Hanawalt, Some corrosion characteristics of high purity magnesium alloys, Trans. Electrochem. Soc. 81 (1942) 423–433. doi:10.1149/1.3071389.

[96] R. Hausbrand, M. Stratmann, M. Rohwerder, The Physical Meaning of Electrode Potentials at Metal Surfaces and Polymer/Metal Interfaces: Consequences for Delamination, J. Electrochem. Soc. 155 (2008) C369. doi:10.1149/1.2926589.

[97] R. Hausbrand, M. Stratmann, M. Rohwerder, Corrosion of zinc–magnesium coatings: Mechanism of paint delamination, Corros. Sci. 51 (2009) 2107–2114. doi:10.1016/j.corsci.2009.05.042.

[98] S. Lebouil, A. Duboin, F. Monti, P. Tabeling, P. Volovitch, K. Ogle, A novel approach to on-line measurement of gas evolution kinetics: Application to the negative difference effect of Mg in chloride solution, Electrochimica Acta. 124 (2014) 176–182. doi:10.1016/j.electacta.2013.07.131.

[99] L. Rossrucker, K.J.J. Mayrhofer, G.S. Frankel, N. Birbilis, Investigating the Real Time Dissolution of Mg Using Online Analysis by ICP-MS, J. Electrochem. Soc. 161 (2014) C115–C119. doi:10.1149/2.064403jes.